Optomechanics and nonlinear mechanics of suspended photonic crystal membranes

Optomechanics and nonlinear mechanics of suspended photonic crystal membranes

A dissertation presented

by

Pui Chuen Hui

to

The School of Engineering and Applied Sciences

in partial fulfillment of the requirements

for the degree of

Doctor of Philosophy

in the subject of

Engineering Sciences

Harvard University

Cambridge, Massachusetts

July 2014

Thesis advisor

Marko Lončar

Author

Pui Chuen Hui

Optomechanics and nonlinear mechanics of suspended photonic crystal membranes

Abstract

The recent demonstration of strong interactions between optical force and mechanical motion of an optomechanical structure has led to the triumphant result of mechanical ground-state cooling, where the quantum nature of a macroscopic object is revealed. Another intriguing demonstration of quantum physics on a macroscopic level is the measurement of the Casimir force which is a manifestation of the zero-point energy. An interesting aspect of the Casimir effect is that the anharmonicity of the Casimir potential becomes significant when the separation of microscale objects is in the sub-100nm regime. This regime is readily accessible by many of the realized gradient-force-based optomechanical structures. Hence, a new avenue of probing the Casimir effect on-chip all-optically has become available. We propose an integrated optomechanical platform, consisting of a suspended photonic crystal membrane evanescently coupled with a silicon-on-insulator substrate, for (i) measuring the Casimir force gradient and (ii) counteracting the attractive force by exerting a resonantly enhanced repulsive optical gradient force. This thesis first presents the full characterization of the optomechanical properties of the system *in vacuo*. The interplay of the optical gradient force (optomechanical coupling strength $g_{om}/2\pi$=-66GHz/nm) and the photothermal force manifested in the optical spring effect and dy-

namic backaction is elucidated. Static displacement by the repulsive force of 1nm/mW is also demonstrated.

In the second part of the thesis, the nonlinear mechanical signatures upon a strong coherent drive are reported. By resonantly driving the photonic crystal membrane with a piezo-actuator and an optical gradient force, we observed mechanical frequency mixing, mechanical bistability and non-trivial interactions of the Brownian peak with the driving signal. Finally we present our recent progress in establishing electrostatic control of individual photonic crystal membranes to reduce and calibrate the electrostatic artifact which plagues Casimir measurements.

The results discussed in this thesis point towards an auspicious future of a complete realization of a Casimir optomechanical structure and novel applications with nonlinearity afforded by the Casimir force and the optical gradient force.

Contents

List of Figures

List of Tables

Acknowledgments

I am honored and blessed to work in a nurturing, supportive and resourceful environment that helped me thrive as a scientist. Surrounded by colleagues who share intellectual thoughts, words of wisdom and encouragement, work and life experiences, jokes and rants, I have had an enjoyable time in the past six years of graduate study. First and foremost, I thank Prof. Marko Loncar for being a wonderful mentor. His availability for scientific discussion, his patience, encouragement and challenges, his generosity with his research resources, etc. help shape me to be a better researcher. I am indebted to him for his supervision and the opportunities he provides me with.

I thank Ian Frank, Irfan Bulu, Mughees Khan, Qimin Quan, Parag Deotare, Anna Shneidman, Young-Ik Sohn, Vivek Venkataraman, Peter Stark, Pawel Latawiec, Murray McCutcheon, Jennifer Choy, Raji Shankar, Yinan Zhang, Ian Burgess, Stefan Kalchmair, Birgit Hausmann, I-Chun Huang, Mike Burek, Haig Atkian, Cheng Wang, Shota Kita, Srujan Meesala, Khadijeh Bayat, Tom Babinec, Daniel Ramos, Dan Floyd, Zin Lin, and Wooyoung Hong for their friendship, services and inspiration brought to the lab. In particular, I acknowledge Ray's initial development of lift-off processing, Young-Ik's help with the wirebonding and Peter Stark's masterful help with repairing the vacuum system and instruction about PDMS.

Among those with whom I have worked closely, I thank Igor Lovchinsky for his collaboration, incredible insights and eye-opening musical discussion in the initial phase of the work. I thank my lab buddy David Woolf for four fruitful years of partnership, and teaching me much about physical thinking and presentation techniques. I thank Alejandro Rodriguez-Wong not only for inculcating me academically, but also for being a constant source of encouragement and fun. I thank Eiji Iwase for being a

great teacher of fabrication and other research techniques.

I thank Sagar Bhandari, Yat-sen Au, Katie Pooley, Alex Woolf and Shanying Cui for generously granting me occasional access to their lab equipment. I thank Terry Szeto, Yuyu Chen, Mike Smith, Jim MacArthur and Ellery Buntel for their assistance in various apsects of the dissertation work. I thank Tarek Anous, Mikhail Kats, Romain Blanchard and Jeff Parker for their friendship and intellectual help.

I thank Kathy Masse for her assistance in equipment purchases and other administrative matters. I thank the staff of Harvard's Center for Nanoscale Systems, in particular Jiang Dong Deng, John Tsakirgis and Yuan Lu, for their prompt response and friendliness.

I thank Prof. Marko Loncar, Federico Capasso, and Evelyn Hu for serving on the dissertation committee and providing me with valuable feedback and guidance. I also thank Prof. Steven G. Johnson, Robert Westervelt and Donhee Ham for their insights in photonics, semiconductor surface states and self-oscillators.

I thank my friends at BCEC for their fellowship and prayerful support.

I am grateful to my parents and my sisters for their loving support and unconditional sacrifices which allow me to comfortably pursue a research career. In particular I thank them for their understanding and patience for all the calls I miss. I am also grateful to my parents-in-law, for their academic advice, loving care and prayers. My formal start at the Loncar Lab coincided with the courtship with my dear wife Wendy five years ago. This unplanned arrangement turns out to have immensely blessed my life and scientific career. From her, I learnt about disciplines, persistence in the pursuit of excellence, importance of rest and exercise, and many inspiring qualities. She

loves me with her caring presence at all times, by keeping me accountable, praying with me and bringing home cookies and free food. Wendy, thank you for being the constant in my life.

Finally and most importantly, I give great thanks to God for defining my identity and purpose of life, teaching me about humility and discipline, helping me symmetrize equations when I was hopelessly stuck in a derivation, and showing me His unfailing love in all parts of my life. *Psalm 36:9 For with you is the fountain of life; in your light we see light.*

Dedicated to Wendy my wife

Chapter 1

Introduction and summary

1.1 Introduction of optomechanics mediated by the optical gradient force

In the late 19th century, James Maxwell formulated the wave theory for electromagnetism, where one of the implications is that light as electromagnetic wave carries energy and momentum [1]. The fascinating history of demonstrating the mechanical effects of light started from the experiments performed by Lebedew [2] and Nichols and Hull [3] by 1903. Albeit the small momentum p carried by light, e.g. h/λ=4.28$\times 10^{-28}$kg m/s per telecom photon, the invention of lasers to provide light with high intensities facilitated one of the first applications of the mechanical effect of light on macroscopic objects. In the early 80's, Ashkin demonstrated the trapping of micron-sized particles by a tightly focused laser light in both normal and tangential directions which requires the balance of the optical scattering and gradient forces

on the particles [4]. Shortly laser cooling and trapping of ions and neutral atoms [5, 6, 7, 8] was demonstrated, leading to breakthroughs in various aspects of atomic physics, including the realization of Bose-Einstein condensates [9], quantum simulation of arrays of atoms trapped in optical lattices, and a new field of atom optics [10]. The physics of optomechanics has strong resemblance with Doppler cooling in atomic/optical physics [11, 12, 13] whose groundbreaking development preceded optomechanics by two decades, but here the predicted quantum nature is manifested in macroscopic objects. Instead of the atomic energy levels being dressed due to strong atom-light interactions, in optomechanics, the photonic resonant states are dressed due to strong optomechanical interactions [11].

Similar to conventional optical trapping, optical forces could be categorized into scattering force/ radiation pressure and gradient force. For the scattering-force-based approach, the small momentum imparted by one photon on a compliant object can be drastically enhanced by introducing an optical cavity where the photon, while not being absorbed and assuming elastic collision, keeps exchanging momentum with the movable element within the cavity lifetime τ. The corresponding optical force exerted on the movable element is given by $N\hbar k/\tau$. Often, the canonical example of the optomechanical effect is a Fabry-Perot cavity which consists of a movable mirror [13]: the optical force is maximal when the wavelength of light is resonant with the cavity. Hence the movable mirror is displaced which in turn detunes the cavity and hence the radiation pressure on the mirror. The mirror then moves towards its initial equilibrium as a result of the restoring mechanical spring force. The radiation-pressure-based optomechanics are manifested in a variety of familiar photonic devices

spanning over a large range of length scale and frequency. In Fig. 1.1 we highlight some of the demonstrations in the past decade.

For the gradient-force based approach, both attractive and repulsive forces can be exerted in coupled optomechanical devices [14, 15, 16, 17, 18, 20, 30, 31, 32]. In the same spirit of obtaining large radiation pressure by constructing a high-finesse optical cavity with highly reflective mirrors/ total internal reflection, the forces can be enhanced with optical resonances. The working principle is described in the next section. Some representative structures are displayed in Fig. 1.1(a-h).

Finally, light can lead to mechanical deformation through photothermal interactions, in which the movable structure absorbs part of the incident light which is converted to heat. As a result of thermal expansion and difference in thermal expansion coefficients between the device layer and the bottom supporting substrate, thermal stress arises. It causes bending of the movable structure. Similar optomechanical properties can occur in such system as one introduces a Fabry-Perot cavity to enhance and modulate the light absorption. Examples include the excitation of a gold-coated cantilever excited by a gold-coated optical fiber placed in close proximity (Fig. 1.1(m)) [29], and a silicon cantilever excited with a laser whose frequency corresponds to photon energy beyond silicons bandgap (Fig. 1.1(n)) [28]. While the photothermal effect also allows for optical spring tuning and dynamic back-action (mediated by delay due to its finite thermal time constant), the photothermal effect presents itself as a competing effect in the demonstration of several optomechanical devices [33, 29, 34].

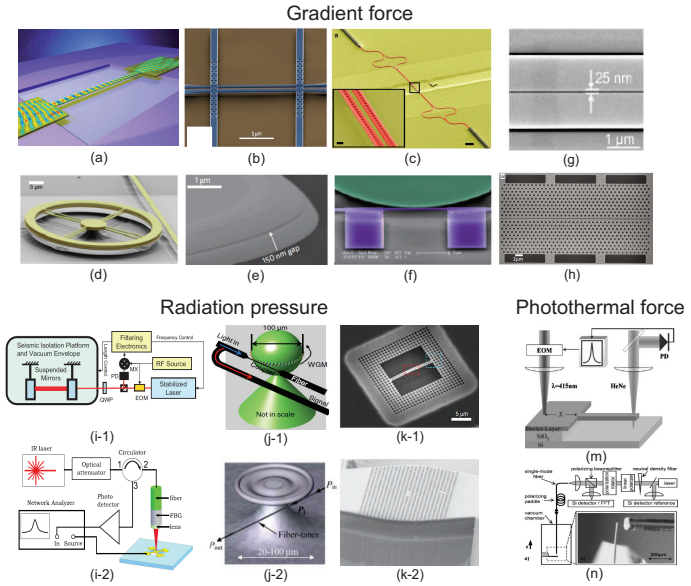

Figure 1.1: Optomechanical structures actuated by radiation pressure, optical gradient and photothermal force. Gradient-force based: (a) Si waveguide (WG) acting as a doubly-clamped beam couples light with the underlying buried oxide layer, demonstrating attractive optical force and Duffing nonlinearity[14]; (b) Coupled Si WGs where attractive and repulsive optical forces are exerted by controlling the relative phase of incoming electric field[15]; (c) Coupled Si PhC cavity WGs where atmospheric operation of attractive optical force with an incoherent light source is demonstrated[16]; (d) Coupled SiN ring resonators where attractive and repulsive forces are related to corresponding mode (anti-)symmetry[17]; (e) Coupled silica microdisks[18]; (f) Dispersive and dissipative optomechanical coupling with Si WGs coupled to a Si microdisk[19]; (g) Au-coated SiN plasmonic WG[20]; (h) Si slot WGs where electric field is tightly confined in the air gap [21]. The effective refractive index increases as the slot size decreases. Radiation-pressure based: (i-1) Fabry-Perot (FP)interferometer in Laser Interferometer Gravitation Wave Observatory[22] (i-2) FP cavity formed by a gold-palladium mirror[23]; (j-1) Silica microtoroid demonstrating quantum coherent coupling[24]; (j-2) Silica microsphere supporting both optical and acoustical whispering gallery modes; excitation of mechanical modes mediated by stimulated Brillouin scattering[25]; (k-1) Si optomechanical crystal with phononic shield optomechanically cooled to the quantum ground state[26]; (k-2) InP PhC cavity with strongly co-localized optical and mechanical modes[27]. Photothermal-force based: (m) A Si cantilever actuated by thermal stress as Si absorbs HeNe light[28]. The effect is modulated by the FP cavity formed by the cantilever and the bottom substrate. (n) Combination of radiation pressure and photothermal effect in a FP cavity formed by a Au-coated cantilever and optical fiber[29].

1.1.1 Optical gradient force in coupled systems

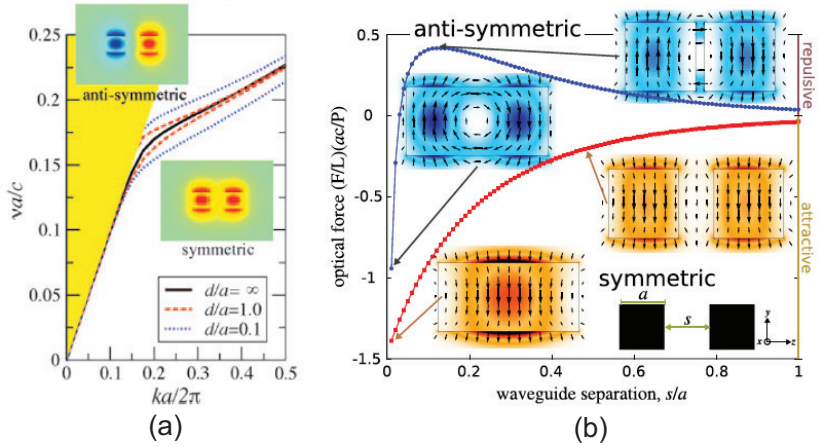

Figure 1.2: (Adapted from [31], [35])(a) Dispersion diagram for coupled waveguides with separations of $d/a = \infty$ (black solid), 1 (red dashed) and 0.1 (blue dashed), where a is the width of the individual waveguide. Insets are the mode profiles of the major field component which can be characterized as bonding/ symmetric (below the black solid line) and anti-bonding/ anti-symmetric (above the black solid line) [31]. As the coupling distance decreases, the bonding mode red-shifts where the anti-bonding mode blue-shifts. (b) Normalized gradient force per unit length per excitation power over different waveguide separations s for a particular wavevector [35]. Positive optical force denotes repulsive force where negative force denotes attractive force. The corresponding mode profiles of the bonding and the anti-bonding modes are shown. Note that the bonding mode has increasingly large attractive force as the waveguide separation decreases, where the anti-bonding mode has increasingly large repulsive force only up to $s/a = 0.03$ and the force switches sign with even small separations.

To illustrate the origin of the optical gradient force, we start by considering two identical waveguides placed in close proximity [31]. Here the waveguides become coupled via the evanescent fields extending outside of them. As a result of the evanescent perturbation, the degeneracy of the propagating modes supported by the waveguides is lifted causing level repulsion, where the initial eigenmode is split into a pair of modes with frequency detuning from the initial eigen-frequency dependent on the coupling strength and degree of field perturbation [32]. The idea is illustrated in

the dispersion diagram in Fig. 1.2(a) as two waveguides approach each other from infinity. Quantitatively with perturbation theory, the frequency shift $\Delta\omega$) is given by [36]

$$\frac{\Delta\omega}{\omega} = -\frac{1}{2}\frac{\langle \mathbf{E}_{\parallel}|\mathbf{\Delta s}(\epsilon_{\mathbf{1}} - \epsilon_{\mathbf{2}})|\mathbf{E}_{\parallel}\rangle - \langle \mathbf{D}_{\perp}|\mathbf{\Delta s}(\epsilon_{\mathbf{1}}^{-\mathbf{1}} - \epsilon_{\mathbf{2}}^{-\mathbf{1}}|\mathbf{D}_{\perp}\rangle}{\langle \mathbf{E}|\epsilon|\mathbf{E}\rangle} \tag{1.1}$$

when a boundary is moved Δs from a dielectric ϵ_1 to ϵ_2. When mechanical degrees of freedom are introduced to such coupled structures, i.e. the waveguides are partially released from the bottom substrate, attractive or repulsive optical forces lead to the reconfiguration of the waveguides in an effort of lowering the mode's optical energy and red-shifting the mode. The work done by the optical force causes a change in the optical energy. The polarity of the optical force is predominantly determined by the relative phases of the electric field in the respective waveguides. In particular, when the electric field in the coupled waveguide mode is in phase, it corresponds to a bonding/ symmetric mode which gives an attractive optical force. This can be understood by the fact that the optical mode's energy is reduced when more of the electric field resides in the high-index dielectric. Hence, pushing the waveguides together encourages more electromagnetic field to be concentrated in the waveguides, and thus lowers the systems' overall optical energy. In Fig. 1.2(b), the attractive optical force (red-line) is shown to rapidly increase as the waveguide becomes more coupled. On the contrary, when the field in the coupled waveguide mode is out of phase, we obtain an anti-bonding/ anti-symmetric mode which corresponds to a repulsive optical force. As seen in the corresponding mode profile in Fig. 1.2b, a nodal plane bisecting the mode exists and the electric field is found closer to the far side of the waveguides [35]. Yet there is a caveat about the repulsive force which we

will detail in a later section.

The energy principle of understanding and calculating the attractive and repulsive optical forces is helpful in gaining physical insights about the origin and design strategies (to be discussed shortly) of the forces. However, this method only works for closed systems which include most of the optomechanical structures in the literature. For open systems where leaky modes and dissipative effects play a significant role in the optical force, Maxwell stress tensors are employed for the force calculations, by first attaining the electromagnetic field distribution everywhere in all directions upon certain excitations [1]. It can be shown that for closed systems the Maxwell stress tensor approach is equivalent to the energy principle aforementioned.

1.1.2 Frequency-dependent polarity of gradient force

Since the first demonstration of attractive and repulsive optical gradient forces by the Tang group with a silicon waveguide coupled to a silica substrate [14] in the same spirit of the coupled waveguide system described above, a deluge of optomechanical structures actuated by resonantly enhanced optical gradient forces rapidly emerged. Geometries and materials explored to attain optomechanical transduction and actuation in coupled systems range from silica and GaAs microdisks [18, 37, 38], silicon nitride microrings [17], silicon and InGaAsP photonic crystal (PhC) membranes and cavities [34, 39, 16, 40], etc. Each coupled system has its own competitive edge suited for particular sets of application, but share the general feature of frequency-dependent polarity of gradient forces. In the same way as level repulsion in guided modes of coupled waveguides, resonances with finite lifetime, be they whispering gallery modes,

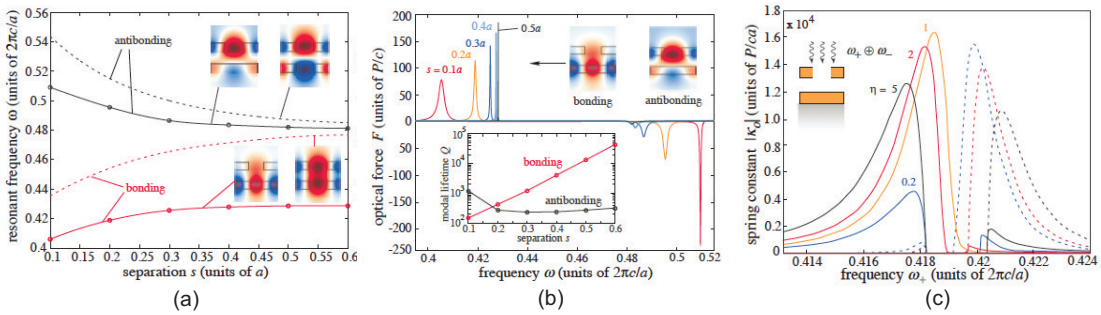

Figure 1.3: (a) Resonant frequency (normalized to periodicity a of the bonding (red) and anti-bonding (black) modes in i. asymmetric coupled PhC-slab system (solid line) and ii. symmetric coupled PhC-PhC system as a function of membrane separation s [32]. The corresponding mode profiles delineating the relative phase in a unit cell of both systems are illustrated. Note that in the asymmetric system, the electric field is concentrated in the bottom slab layer for the bonding mode whereas the field is concentrated in the top PhC layer for the anti-bonding mode. (b) Spectra of the optical gradient force for various PhC-slab separations from $s = 0.1a$ to $s = 0.5a$, which are calculated by a delta-pulse excitation in time to obtain a broadband response. Inset shows the corresponding change of quality factor Q of both the bonding and anti-bonding resonances as a function of PhC-slab separation s: Change of Q for the bonding modeis is drastic compared to the anti-bonding mode as a result of the interactions of the leaky guided resonance in the PhC and lossless guided mode in the slab. (c) Absolute value of pptical spring —κ_o— as a function of pump frequency $\omega+$ due to a two-mode excitation of an attractive and a repulsive force pumped at ω_+ and fixed ω_- respectively, plotted for different power ratios $\eta = P_{\omega_-}/P_{\omega_+}$. Solid lines represent stable solutions where dashes lines represent unstable solutions.

guided resonances in 1-D and 2-D photonic crystal or localized modes in photonic crystal cavity, split into attractive and repulsive force pairs upon evanescent coupling [32, 30]. In other words, one can simply actuate an optomechanical device with an attractive and a repulsive force by choosing the corresponding excitation frequencies. Each of these force pairs could have different responsivity with response to mechanical deformation (dω/ds or optomechanical coupling g_{om}), which is intimately related to the electromagnetic field distribution of the resonance concerned. We reported that attractive and repulsive force pairs also arise in highly asymmetric systems [32].

The system we consider, shown in Fig. 1.3a, is a photonic crystal membrane coupled to layered substrate where guided resonances (with radiative loss) can couple with lossless guided modes (possibly of frequency different from the guided resonances) supported by an asymmetric slab waveguide (a silicon-on-insulator substrate with a thin device layer in this case). Similar to the symmetric case of two coupled photonic crystal membranes, we observe in our asymmetric system that a pair of bonding and antibonding resonances which move apart from each other in frequency as the PhC membrane approaches the substrate. The force enhancement by introducing a guided resonance is more than a hundred fold. Two interesting features stemming from the asymmetry are highlighted here: 1). From the mode profile illustrated in Figure 1.3b, the bonding mode bears more resemblance to the slab waveguide mode while the antibonding mode bears more resemblance to the leaky PhC guided resonance. Thus, the bonding mode has a strong response in the quality factor (from 10^4 to 10^2 in the inset of Fig. 1.3b) with respect to the slab separation upon increasing perturbation by the leaky mode. 2). As a result of the strong coupling-dependent variation in Q of the bonding mode, while the repulsive force (antibonding mode) increases in strength as the membrane separation decreases, the attractive force (bonding mode) amplitude decreases, as shown in Fig. 1.3b. Such non-trivial interactions between a lossless waveguide mode and a leaky guided resonance shed light for new strategies of engineering resonantly enhanced gradient forces. Furthermore, for photonic structures which support many resonances, e.g. microdisks [37, 18], photonic crystal slabs [34, 39], microspheres [30, 41], the coupling-induced frequency-splitting quickly complicates the force spectrum, especially in the higher frequency range where the

density of states increases. With this gallery of bipolar force pairs of varying g_{om} across a wide frequency range, it is possible to perform multi-modal excitations to engineer the net optical force exerted on the optomechanical structure and tune the mechanical spring constant dramatically without perturbing the initial mechanical equilibrium [32, 42]. This opens up a new avenue of optomechanical trapping and exposing the systems mechanical nonlinearity as the linear response is suppressed.

1.1.3 Novel approaches of gradient force enhancement

A commonality of the current demonstrations of coupled optomechanical devices is the strategy of enhancing the optomechanical interactions. Specifically, since the strength of the optical force is related to the change of the optical energy with respect to the mechanical deformation in optomechanical devices, techniques of resonantly enhancing the system's optical energy to achieve strong coupling in photonic-chip-based light-atom interactions [44, 45] were immediately translated to boost the optomechanical coupling and force amplitude. For the camp of radiation-pressured-based optomechanics, much emphasis is placed on obtaining a high-finesse cavity and designing phoxonic structures where ultrahigh-Q optical and mechanical modes are co-localized [27, 46, 47]. The combination of high optical quality factor (in the range of tens of thousands or above) and excitation of high-frequency (MHz-GHz) mechanical mode with low damping loss enabled the exciting demonstration of optical spring effect, optomechanically induced self-oscillations, cooling of macroscopic objects, etc [13]. For optomechanics with gradient force, force enhancement can be pursued by novel approaches. To motivate this, we consider the bipolar gradient forces in a coupled

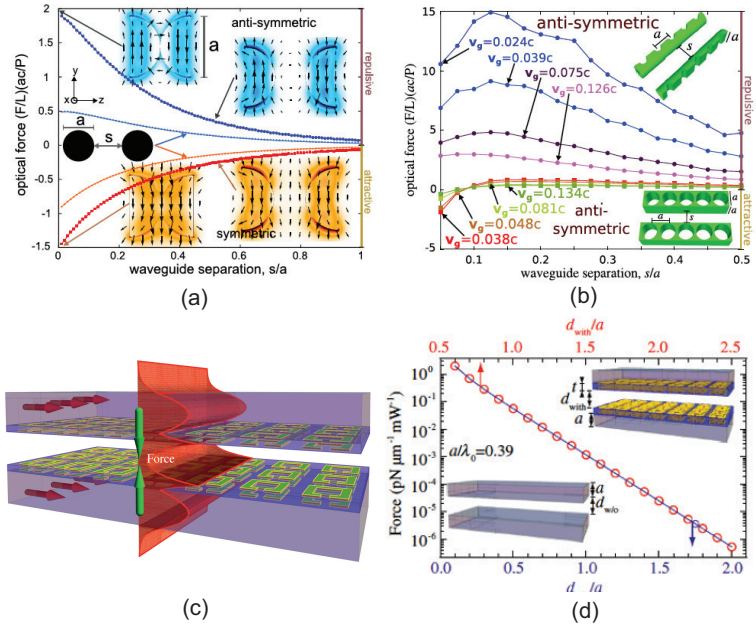

Figure 1.4: (a) Comparison of the normalized optical force as a function of waveguide separations s (measured from the closest points of the waveguides) for two geometries: circle-circle (thin lines) and hemicircle-hemicircle (thick lines)[35]. The mode profiles of both the bonding and the anti-bonding modes of both touching and separated waveguides are illustrated. It shows the expected trend of increasing attractive force when waveguides are placed closer, but the repulsive force also increases monotonically as opposed to the case of coupled square waveguides in Fig. 1.2(b). The convex inner surface of the waveguides pushes more electric field of the anti-bonding mode into air which increases the mode's frequency. (b) Comparison of the normalized optical force due to the anti-bonding mode as a function of waveguide separation s for coupled photonic crystal waveguides, one with a square cross section, and the other with a hemicircular cross section[35]. The slow-light mode as a result of the hole periodicity are excited for enhancing the mode energy, but the force enhancement is more prominent for the PhC waveguides with a hemicircular cross section (a factor of 30 with a slow-light mode with group velocity v_g of $0.024c$ which highlights the combined effect of altering waveguide morphology and the slow-light mode excitation. (c) Illustration of slab waveguides cladded with a layer of metamaterials made of split-ring resonators which reduces the optical distance perceived by the evanescent field [43]. The field in the metamaterial layer is amplified before decaying in the air region. (d) Demonstration of the equivalence of the optical gradient force achieved in a non-transformed geometry (with separation d) and in a metamaterial-mediated transformed geometry (with separation d_{with}) [43]. Note the reduction in the optical space is $0.5a$ where a is the thickness of the slab waveguide.

waveguide system again. While the attractive force of a bonding mode monotonically increases in strength as the waveguides approach each other, it is shown, however, that an antibonding mode does not guarantee to generate a repulsive force [31, 35]: when the waveguides are in very close proximity (e.g. tens of nanometers for telecom excitation), the evanescent field in the air slot between the waveguides has significant contribution to establishing a net attractive force instead. Nonetheless, Oskooi and Favuzzi et al. demonstrate that by tailoring the waveguides' interacting surfaces the evanescent field enhancement of the slot mode can be suppressed while maintaining the strength of the repulsive force [35, 48]. In fact other new directions of enhancing the transverse attractive and repulsive optical gradient forces, apart from the typical approach of employing ultrahigh-Q optical modes (e.g. whispering gallery mode), emerged in recent years. These strategies include 1). adopting slow-light Bloch modes to enhance the intra-cavity optical energy [31]; 2). designing more complex morphologies which engineer the boundary conditions and hence the electric field distribution [35, 48], 3). incorporating metamaterials to the waveguide boundary surfaces which locally engineer the dielectric profile experienced by the evanescent field [49], and 4). adopting transformation optics to effectively reduce the coupling distance perceived by the resonant electric field, which lessens the challenge of fabricating free-standing devices with a small sacrificial layer [43].

Another notable approach of force enhancement can be found in exploiting symmetry in periodic structures. Liu et al. [50] and Sun et al. [51] numerically demonstrated that by perturbing the alignment of the periodic holes between two photonic crystals (e.g. gratings and nano-beams) longitudinal optical force can be excited. Liu

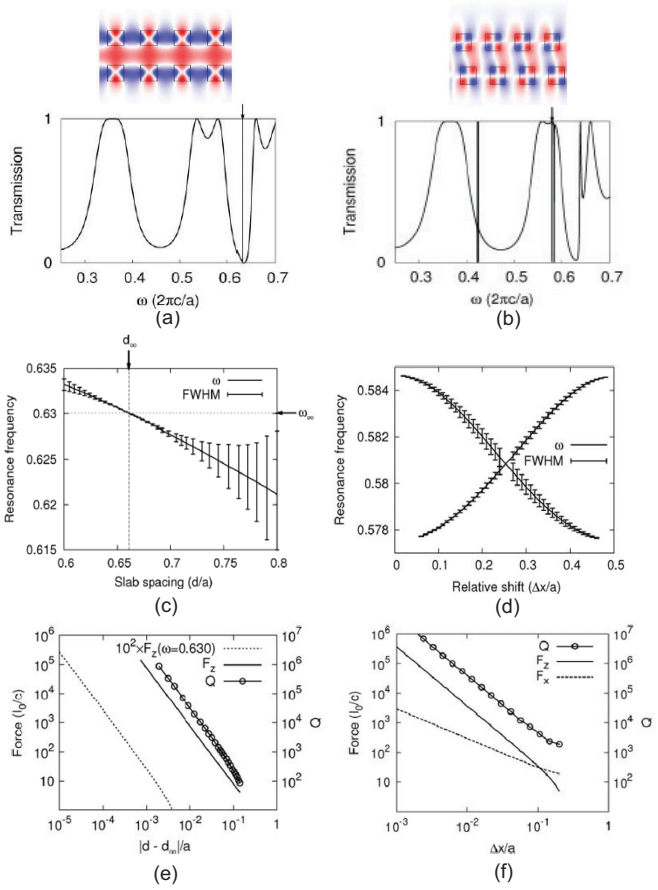

Figure 1.5: Access to large normal and lateral optical gradient forces via dark states [50]: (a) Transmission spectrum of coupled PhC slabs separated by $d = 0.65a$ (where a is the hole periodicity) and the corresponding mode profile at normalized frequency of $\omega = 0.58$; (b) Transmission spectrum of coupled PhC slabs separated by $d = 0.5a$ and the corresponding mode profile at normalized frequency of $\omega = 0.58$; (c) Resonance frequency and linewidth of the "dark mode as a function of the slab separation. The rapid change of the mode quality factor with slab separation is due to the Fabry-Perot interference of the bright modes of the individual PhC. d_∞ is the slab separation where the resonance does not couple to external radiation. (d) Resonance frequency and linewidth of the pair of dark modes at each lateral shift $\Delta x/a$. The in-plane symmetry of the resonance is reflected in the plot. (e) Variation of the normal optical force and the quality factor pumped at $\omega = 0.58$ (solid line) as the slab separation varies about d_∞. Optical force pumped at a slightly detuned frequency (dotted line) is shown to illustrate force enhancement mediated by the high Q. (f) Variation of the normal and lateral gradient forces and quality factor as a function of the relative lateral shift of the PhC $\Delta x/a$.

et al. considered two coupled photonic crystal slabs supporting guided resonances [50]. Depending on the in-plane modal symmetry relative to the symmetry of an incident plane wave, some (bright) guided resonances couple to external radiation by band-folding where some do not and they are known as dark modes. When the two photonic crystal slabs are vertically aligned and evanescently coupled, two interesting phenomena related to dark states occur. First, both coupled bright guided resonances and coupled dark guided resonances could create a dark state at a specific slab separation d_∞ as a result of Fabry-Perot resonances with unity slab reflectivity. For slab separations near d_∞, one may take advantage of the high-Q "near-dark" modes for force enhancement in the normal directions. Second, the dark guided resonances remain uncoupled to external excitation until the in-plane rotational symmetry is broken by laterally offsetting the slab alignment. The emergence of such "near-dark" modes lead to a longitudinal force on the slab which follows the periodicity of the perforation. We envision that the system having the versatility of actuation and sensitivity of transverse and lateral optical forces allows for an all-optical 3-dimensional accelerometer. Certainly the realization of optomechanical structures with greater design complexities demands more sophisticated fabrication techniques. We anticipate the ongoing development of experimental demonstrations of metamaterials in the micron-scale [52], multi-layer thin-film assembly assisted by soft lithography [53], and other micro-fabrication advancement pave a promising path for demonstrating pronounced force enhancement with optimized optical designs.

As a summary of the discussion of various approaches of gradient force enhancement, Table 1.1 highlights a few of the recently studied and representative gradient-

Team	Structure - coupling distance	Mechanical frequency f_m (MHz)	Mechanical quality factor Q_m	Optical quality factor Q_{opt}	$g_{om}/2\pi$ (GHz/nm)	Optical force F_{opt} (nN/mW)	Static displacement/ driven amplitude (nm/mW)
Eichenfield et al. 2007	SiN disk resonator with tapered fiber – 702nm	$0.193X10^{-6}$	-	$1.1x10^6$		-0.02	-324 (static)
Li et al 2008	Si waveguide with SiO2 substrate – 360nm	8.87	1850	-	-	0.005	2 (driven)
Li et al 2009	Laterally coupled Si waveguides – 100nm	17.05	5300	-	-	-2.2 1.1	~9.6 (driven)
Rosenberg/ Liang et al 2009	Vertically coupled SiO2 ring resonator – 138nm	8.3	3.95 (in air)	$1.8x10^6$	33	-244	
Wiederhecker er al 2009	Vertically coupled SiN ring resonator – 640nm	0.6	2 (in air)	$6.8x10^4$ $2.1x10^4$	1.4 -2		-20 (static) 1
Eichenfield et al 2009	Laterally coupled SiN zipper nanobeam cavity – 120nm	8	11600 (in vacuo) 50/150 (in air)	$3x10^5$	123	-	-
Roh et al 2010	Bilayer InP PhC membranes – 200nm	1.8	2 (in air)	1600 700	44 -	-0.83 -	-0.26 (static)
Deotare et al 2012	Laterally coupled Si nanobeam PhC cavity – 70nm	8	17 (in air)	15000	96	-	-
Woolf/ Hui et al 2013	Si PhC membrane vertically coupled with SOI substrate – 160nm	0.16	2000	3400	-66		1 (static)

Table 1.1: Table highlighting several gradient-force-based optomechanical devices in the literature. Information about the photonic structure employed and the separation of coupled elements, mechanical frequency and quality factor, optical quality factor, optomechanical coupling strength (positive for bonding mode), amplitude of attractive (negative)/ repulsive (positive) gradient force achieved and static/ dynamic motion amplitude demonstrated is recorded. [16, 34, 17, 54, 40, 14, 15, 18, 37]

force-actuated optomechanical devices, comparing their fundamental mechanical frequencies and quality factors, optical lifetimes, optomechanical coupling strength, and maximum force/mechanical amplitudes. One observation is that various material systems are chosen for considerations such as thermo-optic effect, free carrier excitation and stress management. Another feature is the successful demonstration of atmospheric operations of these optomechanical devices which circumvent the need for hermetic vacuum packaging for sensing applications.

1.1.4 Technological impact

The conspicuous expression of the optical force in nanophotonic devices facilitates new strategies of achieving reconfigurable and programmable optical devices, along

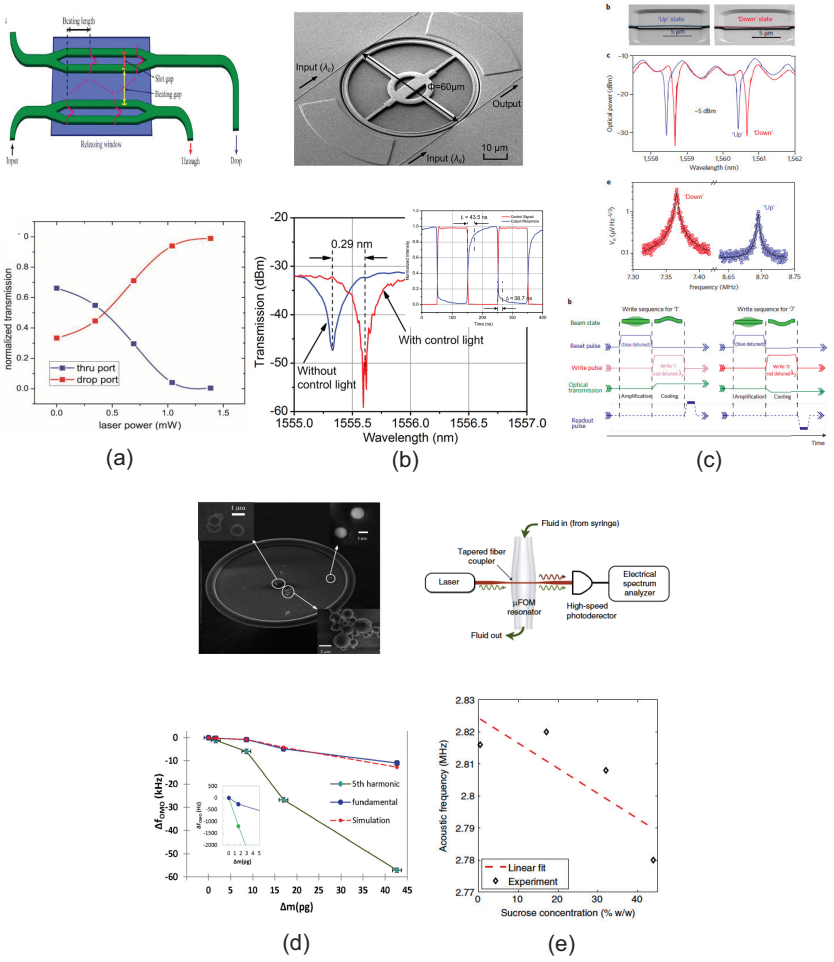

Figure 1.6: (a) Optical waveguide coupler where on-chip tuning is achieved by strong optomechanical coupling in silicon slot waveguides [55]; (b) Optomechanical switching with switching time of tens of nanoseconds, where resonance tuning is achieved by controlling the coupling between the silicon resonator and the underlying buried oxide layer with the gradient force [56]; (c) Optomechanical memory where mechanical bistable transitions are chosen by optomechanical amplification and cooling [57]; (d) Picogram mass detection with toroidal resonators in air where higher harmonics from optomechanical self-oscillations are employed for enhanced detection resolution [58]; (e) Optomechanics with stimulated Brillouin scattering realized in microfluidic environment for detecting solutions with varying concentrations [59, 60].

with the advancing field of nano-optoelectromechanical systems (NOEMS). Reconfigurable passive optical elements demonstrated include couplers with a pair of coupled optomechanical slot waveguides [55], bandband all-optical filters that can be con-

trolled by incoherent light [16], and on-chip resonance tuning of neighboring devices. Thus far, albeit the relatively large degree of actuation achieved by optical forces along on nanophotonic devices, electrostatic actuation still outperforms optomechanics in the extent of actuation. However in applications where operating environments are adverse to systems with metallization, an all-optical platform could still be desirable.

A subtle effect the community of optomechanics learnt in the past years is buckling of the optomechanical devices caused by compressive stress in the device layer, e.g. in typical silicon-on-insulator substrate, indium phosphide, etc. The compressive stress causes deviation of the fabricated structures from the desired geometry. Solutions to this problem may be resorting to material systems with *tensile* stress instead (e.g. silicon nitride), depositing a thin layer of materials to compensate the stress, or developing stress-relief techniques. However some proposals in fact take advantage of the presence of buckling to create two mechanical bistable states for switching and sensing that basically eliminates the consumption of holding power. Examples are mechanical memory demonstrated by Bagheri et al. [57], optical shock sensor [61], and Intaraprasonk et al. [62].

On the other hand, the strong optomechanical strength offers high readout sensitivity of mechanical motions, even in atmospheric conditions where mechanical signals could still be detected above the noise floor in the presence of strong viscous damping. Accelerometry with broad bandwidth in optomechanical slot waveguides [63], particle detection with self-oscillating toroidal resonators in air [58], and shock-sensing by mechanical buckling transitions are some of the recent demonstrations that exploit the readout sensitivity that is hard to reach by conventional electromechanical

schemes. Some other examples include optomechanical AFM [64, 65], microfluidic optomechanical sensing in a liquid environment [59, 60].

There is also strong drive to seek applications of optomechanics in the classical and quantum regimes, particularly in the radio-frequency window. However, scaling of optomechanical devices to from MHz to GHz range while ensuring large optomechanical transduction efficiency is not trivial. There are significant endeavors to design optomechanical structures which feature strong colocalization of photonic and phononic modes to maximize the dispersive coupling. From there, wavelength conversation (telecom to telecom and telecom to microwave) via quantum state transfer mediated by GHz mechanical modes in the sideband-resolved regime were proposed and demonstrated [66, 67, 68, 69, 70, 46, 71, 72]. Self-oscillating optomechanical oscillators for timing applications in the radio-frequency window are also explored with phase-noise suppression schemes incorporated to rival existing technology of crystal oscillators [73, 74, 75, 76, 77, 78, 79, 80, 81].

1.2 Introduction of the Casimir force detection

According to quantum mechanics, the universe is filled with the zero-point energy, even when all quantum mechanical systems are settled in their ground states [82]. This zero-point energy, intimately related to the Heisenberg's Uncertainty Principle, is composed of a continuum of fluctuating electromagnetic (EM) fields propagating in free space. The vast time scale of the fluctuation allows one to decompose the fields over a very broadband of frequencies in the frequency domain. The discussion of fluctuation-induced electromagnetic forces is often motivated by considering two

neutral particles with no permanent dipole moments placed in close proximity d with each other [83, 84]. Instantaneous dipole moments due to the quantum-mechanically agitated electrons causes spontaneous radiation of electromagnetic fields. The electromagnetic fields in turn transiently polarize the neighboring particle. The instantaneous dipoles rotate to align themselves to the lowest energy configuration. As a result, an electromagnetic force that scales as $1/d^6$ arises. This is the basis of the van der Waals force, where the electromagnetic fields instantaneously arrive at neighboring particle in the quasi-static limit. However, the retardation effect (i.e. the finite propagating time of EM waves) has to be accounted for when the particles are farther apart. This is the so-called Casimir-Polder limit where the EM force scales as $1/d^7$.

In 1948, Hendrik Casimir considered a situation in which two perfectly conducting metallic plates were placed closely to each other with a separation of d [85]. Due to the boundary conditions set by the metallic plates, the system naturally filters out many of the free-space modes, only allowing an infinite countable number of bounded modes within the metallic plates. By considering the energy densities outside of the plates (sum of EM energy density over a continuum) and inside (sum of EM energy density over a countable set of modes), the energy difference leads to the famously known Casimir effect, where the metallic plates are pushed towards each other. The effect does not involve any actuation of real photons. In this case, the Casimir force is given by

$$F_{Cas} = -\frac{\pi^2 \hbar c}{240 d^4} A, \tag{1.2}$$

where c is the speed of light in vacuum and A is the interaction area. As a simple illustration of the Casimir effect in MEMS, for two perfectly conducting metallic

plates with the interaction dimensions of 30μm$\times 30\mu$m and a separation of 100nm, the attractive force magnitude is $\approx$11.7nN, which is readily detectable with current force detection techniques of ever higher force sensitivity.

As for the Casimir force on realistic dielectric test bodies, Lifshitz extended Casimir's result by including the dielectric response which has resonances over a wide frequency range [86]. The computation of the Casimir force with the Lifshitz formulation requires one to account for the EM energies of all supported surface modes of both polarizations and wave vectors as well. In this formulation, repulsive Casimir force is also possible by filling the gap between two test bodies with a fluid whose dielectric response strength is in between that of the test bodies concerned over a broadband of frequencies. The Lifshitz formulation has been verified by numerous experimental demonstrations in the past two decades, thanks to the vast advancement in microfabrication and high-precision, nanoscale motion control. A large variety of material systems have been explored including real metals like gold, nickel and copper, and semiconductors like highly doped (poly-)silicon, germanium, and indium tin oxide [87, 88, 89, 90, 91, 92, 93, 94, 95, 96]. Recently the geometrical effects on the Casimir force are actively pursued as well, for instance, by considering the interactions of trenches with various depths [97, 98, 99]. While almost all Casimir demonstrations are performed by introducing an external object to a test body, there has been recent efforts in developing on-chip platforms for probing and taking advantage of the Casimir force [89, 100, 101].

Apart from the shear theoretical interest in probing such quantum electrodynamical phenomenon manifested on macroscopic objects, the Casimir effect has relevance

in the prospect of scaling down nano-devices which are subjected to this attractive, highly nonlinear force [102, 103]. With novel computation tools developed to consider the Casimir effect with non-trivial geometry and boundary conditions [84], one may be interested in designing structures that minimize the Casimir effect and in exploring the large mechanical nonlinearity of the Casimir force.

1.3 Theme and structure of the thesis

This thesis is motivated by the ambition of developing a platform for probing and counteracting the Casimir force in an on-chip setting. We propose the application of an enhanced repulsive optical force to counteract the attractive interactions in MEMS and NEMS due to electrostatics and the Casimir force. Our goal is to monitor the position of a mechanical device via the superb optomechanical readout sensitivity and exert a counteracting repulsive force in real-time as the mechanical part is subjected to an overwhelming large attractive potential.

In the study of Casimir interactions and counteraction, we carried out extensive study with asymmetric coupled silicon photonic crystal membranes. Most Casimir experiments were conducted with a sphere-plate geometry eliminating the need for correcting parallelism of interacting surfaces when compared to theoretical calculations. Here with the goal of enhanced readout sensitivity and exerting a sufficiently large, counteracting optical force to prevent stiction, we devise an on-chip integrated platform to perform Casimir measurements of a plate-plate geometry with a novel optomechanical degree of freedom. It features a tethered silicon photonic crystal membrane (30um×30um) suspended above a typical silicon-on-insulator (SOI) sub-

strate. The large interaction area allows for strong expression of the Casimir effect that relaxes the signal-to-noise requirement in our detection. It also has a convenient optical coupling scheme: The square lattice of perforation serves as a polarization-insensitive second-order grating for coupling normally incident light, in contrast to the typical tapered fiber-coupled optomechanical structures.

This thesis elucidates the optomechanics of this proposed system, the effort of detecting the Casimir force via various approaches, and the nonlinear mechanics associated with it. The structure of the thesis is as follows: Chapter 2 describes the details of the experimental setup employed for interrogating the coupled PhC membranes. Chapter 3 shows the full characterization of the optomechanics of the PhC membranes, including the static and dynamic behaviors, which demonstrates the potential of optically controlling a Casimir optomechanical oscillator. Chapter 4 describes our effort in probing the Casimir effect by measuring a large ensemble of devices with different membrane-substrate separations. It also displays various mechanically nonlinear behavior when resonantly driven by a piezoactuator and an optical gradient force. Chapter 5 reports the progress in establishing the capability of electrically addressing individual PhC membranes to minimize the artifacts in Casimir measurements. Finally, we conclude this thesis in Chapter 6 with a discussion of the future outlook.

Chapter 2

Experimental setup

This chapter describes the experimental techniques and setups employed for investigating the optomechanics and nonlinear dynamics of suspended photonic crystal membranes. In particular, the details of fiber interferometry and the vacuum setup are discussed.

2.1 Fiber interferometry

2.1.1 Working principles

A technique pioneered by Rugar in the late 80s [104], fiber interferometry has become a popular technique that finds applications ranging from commercial atomic force microscopy to high-sensitivity motion detection and fiber-based low-temperature confocal microscopy for studying excitonic dynamics in quantum dots [105, 106]. As illustrated in Figure 2.1, the working principle is based on establishing a low-finesse Fabry-Perot cavity between the device-under-test and the cleaved bare fiber

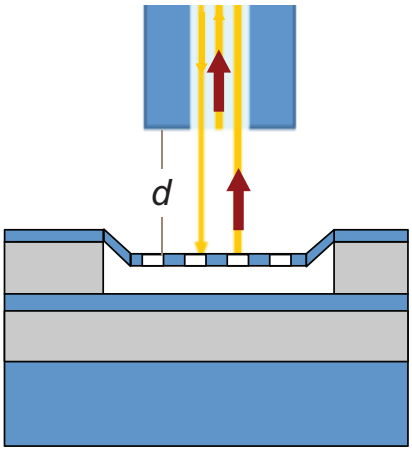

Figure 2.1: Working principle of a fiber interferometer.

(which has a reflectance of 3.6% using the Fresnel coefficient of reflection, and can be drastically boosted by evaporating a thin layer (≈100nm) of gold for a high-finesse cavity [29]). The interference signal between the reflected signal from the bare fiber tip and that from the DUT is recorded by a fast photodetector at the reflected port. The AC motion of the DUT modulates the cavity length and hence the interferometric signals (fringes).

A mathematical description of the interferometric signal is as follows: The reflected signal R_{ref} is given by

$$R_{ref} = \frac{R_{fb} + R(\lambda) - 2\sqrt{R_{fb}R(\lambda)}cos(\frac{4\pi d}{\lambda})}{1 + R_{fb}R(\lambda) - 2\sqrt{R_{fb}R(\lambda)}cos(\frac{4\pi d}{\lambda})}, \tag{2.1}$$

where R_{fb} is the reflectance of the cleaved fiber facet (≈ 0.036), d is the fiber facet-device separation (or the Fabry-Perot cavity length), and $R(\lambda)$ is the reflectance spectrum of the device. Here we assume light exiting from the fiber has no spa-

tial divergence and multiple reflections between the fiber and DUT are accounted for. However in the case of low reflectivity, the interference signal can be well approximated by the case of two-beam interference because the multiply reflected light amplitude is weakened by the fibers low reflectivity, and hence multiple reflections do not contribute significantly to the interference signal.

2.1.2 Experimental realization

Figure 2.2(a) shows the schematic of a typical fiber interferometer setup. A 2×2 fiber coupler is employed. Input light with power I_1 is first split by a certain coupling ratio α which is dependent on the wavelength. One arm is spliced to an angle-polished fiber connector to minimize reflection (60dB attenuation) that could otherwise add to the detected signal as noise. The output light $(1 - \alpha \mathrm{R}(\lambda) I_1)$ may be used as a power reference to obtain the actual total reflectance of the device. The other arm is cleaved to provide a smooth, flat surface which forms a low-reflectance mirror for the fiber interferometry. The reflected light is then collected by the same fiber tip and split by the coupler again. Light that goes back to the laser will be rejected by the laser's isolator, whereas the other path is detected by a photodetector. The reflected, split power detected is given by $\alpha(1\text{-}\alpha)\mathrm{R}(\lambda)I_1$. By dividing the photodetector signal of the device by the photodetector signal of the power reference, one can retrieve the actual total reflectance at the device detection end, given α can be trivially calibrated. Experimentally we observe that the splitting ratio of the nominally 50:50 fiber coupler over the wavelength range of 1480-1680nm varies by at most 3%.

Figure 2.2(b) shows the photographs of the placement of the cleaved optical fiber

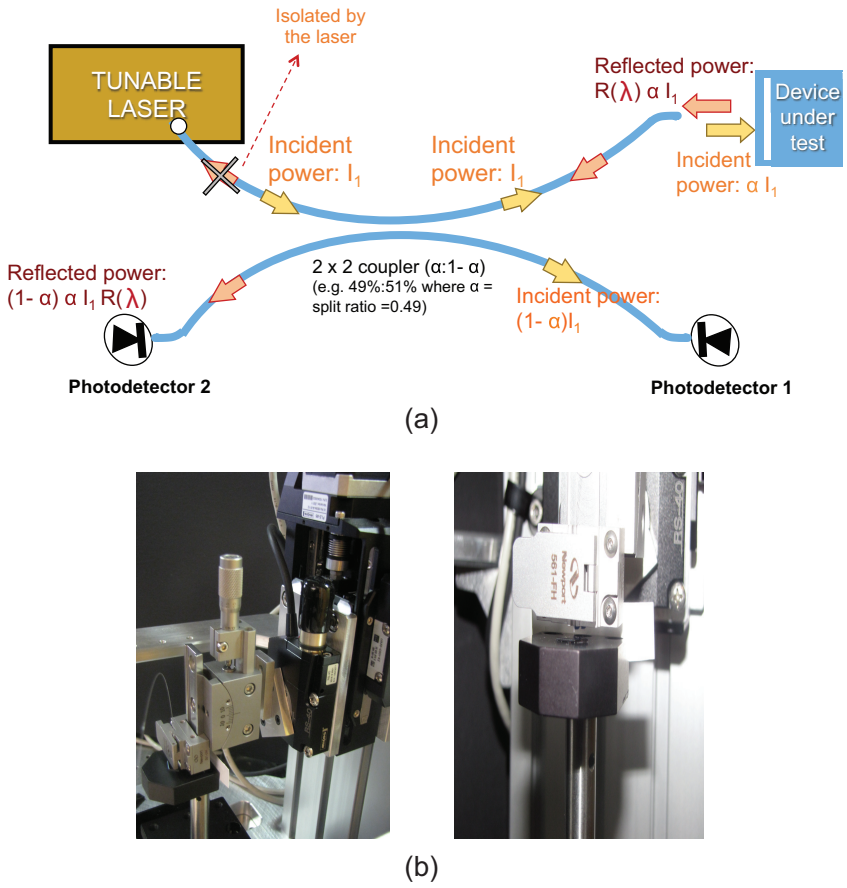

Figure 2.2: (a) Schematic of circuitry of the fiber interferometer and the normalization method. (b) Photographs of the placement of the cleaved optical fiber where minute motion control is enabled by closed-loop motorized and manual linear and angular stages with tip/tilt control.

and the instruments (e.g. goniometer, motorized stage) in the experimental setup.

2.1.3 Static transduction of mechanical displacement

Assume that we operate in a regime where $dR(\lambda)/d\lambda \approx 0$ (which can be inspected from the background envelope of the reflected signal), the *static* fiber facet-device

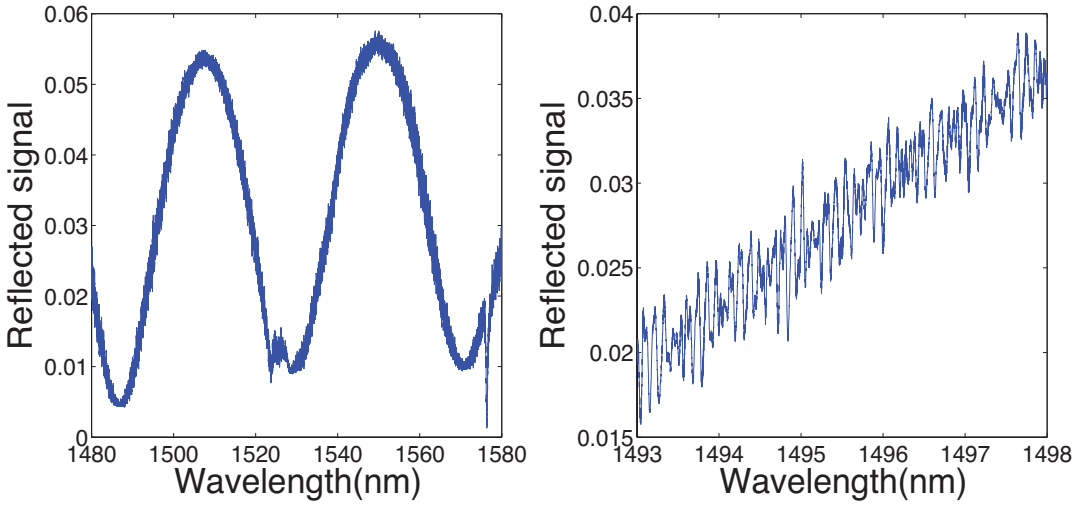

Figure 2.3: Interferometric signal of a device interrogated by fiber interferometry.

separation d_0 can be estimated by

$$d_0 = \frac{1}{2}\left(\frac{\lambda_n \lambda_{n+1}}{\lambda_n - \lambda_{n+1}}\right), \tag{2.2}$$

where λ_n and λ_{n+1} are wavelengths of neighboring peaks or valleys. In order to attain nm precision to independently measure the device's static displacement, we conducted a simple error propagation analysis to evaluate the accuracy we need in extracting the wavelengths λ_n and λ_{n+1}.

$$\delta d = 2d^2 \sqrt{\left[\frac{\delta\lambda_n}{\lambda_n^2}\right]^2 + \left[\frac{\delta\lambda_{n+1}}{\lambda_{n+1}^2}\right]^2}. \tag{2.3}$$

With this analysis we can show that pm precision in extracting the peak/ valley wavelengths is needed to attain nm accuracy in the measurement of d_0. [107] While this is within the reach of our tunable laser sources, we were not able to perform this independent measurement of the static displacement due to the following reason: The finite back-reflection of the incident laser light (with long coherence length)

from the bottom of the silicon handle wafer (approximately 550μm thick) appears as high-frequency nuances with small amplitudes laying over the main fringes. These oscillations introduce uncertainty in fitting the interference fringes of 0.1-0.2nm. This translates to an uncertainty of the fiber-device separation of 89-178nm, rendering the inapplicability of this interferometric method of independently measuring the nanometer optical-force-induced displacement.

Another interferometry technique to calibrate the device displacement is by adjusting the fiber position relative to the device until it rests on the quadrature point which is the most sensitive to displacement [107]. With a similar analysis as above while assuming little change in the reflectance of silicon due to thermo-optic effect by the optical pump, we estimated that about 0.8% change in the maximum voltage signal indicates a $1nm$ displacement. In this experimental condition, our system suffered a 3% fluctuation in the signal due to the high frequency oscillations which drowns out the displacement signal. Recently, by mounting our samples on holders using an adhesive known as Electrodag 502 which consists of carbon particles, we observe the telecom light exiting the sample bottom surface is absorbed. Hence the fringes due to the back-reflection become minimized. Further work to demonstrate sub-nanometer static displacement is in progress. Alternately using a intensity-stabilized light source with low coherence length (e.g. a superluminescent laser diode) or introducing amplitude/ phase modulation may suppress the interferences of reflections from the $\approx$ 0.6 mm range.

2.1.4 Dynamic transduction of mechanical oscillatory motion

An important application of the supreme readout sensitivity of fiber interferometry is the detection of sub-nanometer *oscillatory* movements [104]. It is demonstrated by placing the optical fiber $\approx 70\mu$m above a blank area of a double-SOI sample, which is piezo-driven at 620kHz. The silicon surface is probed with a range of wavelengths of light from 1580nm to 1640nm with an increment of wavelengths of 1nm. At each probe wavelength, the reflected light is analyzed with a real-time spectrum analyzer. The spectral peak at the driven frequency 620kHz is due to the modulation of the fiber-sample separation due to the piezo actuator. The amplitude of the spectral peak at each wavelength is then plotted in Figure 2.4. The signal sensitivity is the strongest at the quadrature point of the fringes. This demonstration verifies the feasibility of the detection of mechanical motion of free-standing devices without optomechanical coupling. Note that the variation in the peak sensitivity over the spectral range (at the quadrature points) could be due to the variation of reflectance of the double-SOI sample over this wavelength range.

2.1.5 Other experimental details

Fiber alignment for optimal coupling

To maximize the coupling and collection efficiency of light to and from the device under study, we manually adjust the tilt of the sample stage relative to the fiber facet. The degree of tilt in both the x-axis and y-axis can first be evaluated by allowing the sample to traverse back and forth by 400μm [108]. When tilt exists, the relative separation of the fiber facet and the sample should vary linearly over the traveling

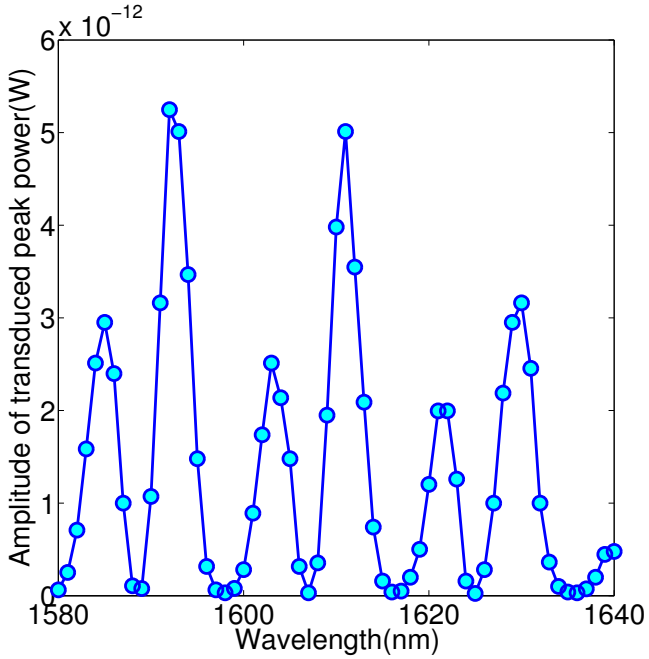

Figure 2.4: Transduction of time-varying mechanical motion by means of fiber interferometry with probe wavelengths from 1580nm to 1640nm. The signal strength is extracted from the amplitude of the detected driven peak signal. It varies sinusoidally with the probe wavelengths. More fringes are intentionally packed into this detection range by positioning the fiber ≈70μm from the sample.

distance. Hence a sinusoidal interferometric fringe signal can be observed. The largest the tilt is, the shorter is the period of the fringes. The goal is to minimize the appearance of the fringe signal by adjusting the tip/tilt knob for the x-direction. The same routine is then repeated for the y-direction. An example of the interferometric fringes during the parallelity adjustment is illustrated in Figure 2.5. Typically the fiber is placed ≈400μm away from the sample such that the fiber tip does not come into contact with the sample during the tilt adjustment, and the effect of the tilt on the fringes can be exaggerated for the correction.

Apart from the tip/tilt correction, the alignment of the fiber tip over the photonic

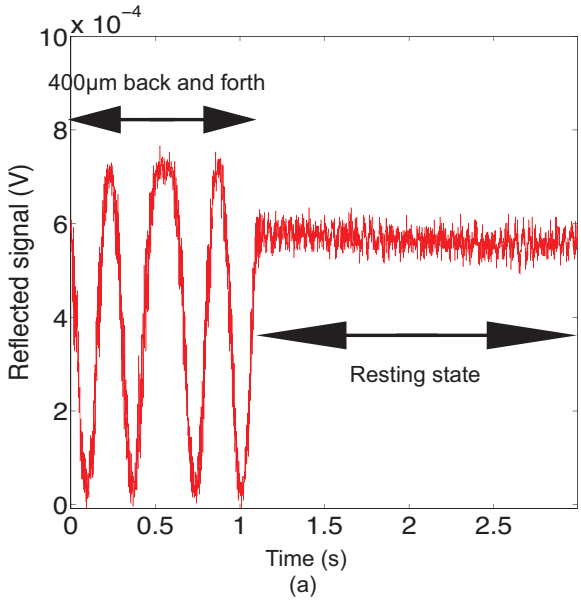

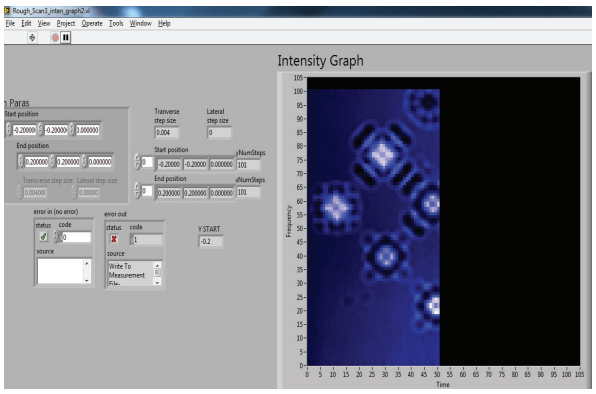

Figure 2.5: (a) An illustration of the tip/tilt alignment: The sample traverse by 400μm back and forth relative to the fiber tip. Tilt in the sample holder is manifested as fiber facet/ sample height variations which produces interferometric signals. The tip/tilt in each axis is then finely adjusted until the signal recorded during the stage's traverse movement becomes as flat as the signal recorded during the stage's rest state. (b) Raster scan automated by a LabVIEW routine for locating the devices under test and aligning the fiber tip at the optimized location with sub-micron resolutions for maximal coupling of light to the photonic devices.

device concerned is performed by performing a raster scan to roughly outline the device map [108], illustrated by a screenshot of the LabVIEW routine developed for this purpose (Figure 2.5(b)). It is possible due to the sufficiently different reflectance/

scattering of the the devices throughout the sample. Then a high-resolution scan over the device interested allows one to choose the most optimal coupling location on an extended device. In particular, if the device is resonant at a certain excitation wavelength, the scan image taken at such wavelength shows a large contrast of reflectance at the best coupling location.

2.2 Vacuum components for fiber interferometry

Vacuum chamber and electrical feedthrough

The detection of the mechanical properties of the optomechanical oscillator is performed in vacuum to minimize the effect of viscous damping. To accommodate the long-range, vacuum-compatible motorized stages, an aluminum vacuum chamber, 18" in diameter and 18" in height illustrated in Figure 2.6(a) and (b), is employed. The initial stage of the experiment soldered all the electrical connections from the linear stages and the encoders to 2 50-pin sub-D connectors. Yet they were fragile and caused minute damage to one of the motorized stages. To save future labor cost in repair, all the electrical connections are directly plugged to five electrical feedthroughs mounted on a 5-way cross, as shown in Figure 2.6(b).

Telescope for monitoring the fiber position

To facilitate placement and monitoring the relative position of the optical fiber to the sample, a telescope is built to relay the image of the optical fiber from the vacuum chamber to the outside. The shortest distance from the center of the vacuum chamber, through the viewport, to the outside is at least 20cm. Hence a lens of

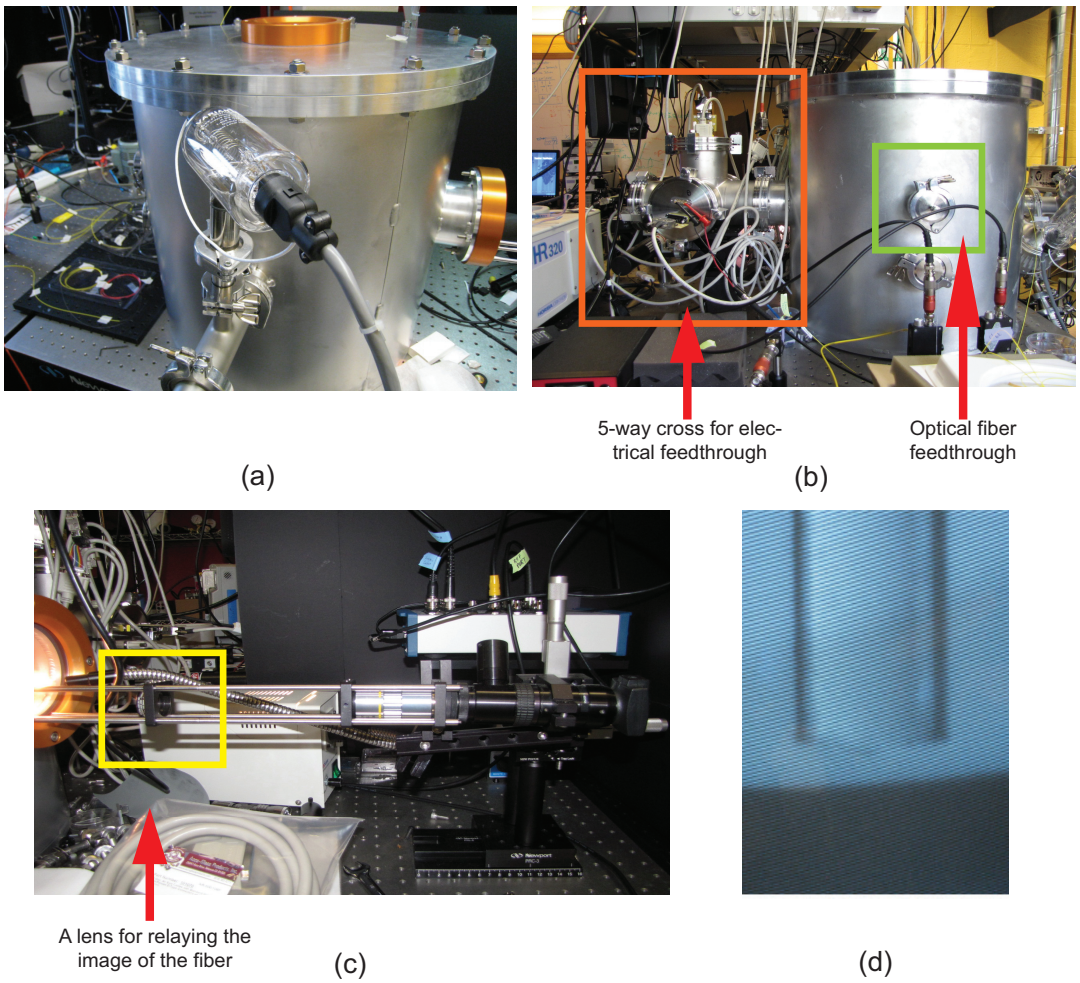

Figure 2.6: (a) An aluminum vacuum chamber, 18" in diameter and 18" in height, capable of high vacuum operation down to 1μTorr. (b) Electrical feedthrough to communicate with the five-axis closed-loop motorized stages via a five-way cross with multiple flanges with D-sub connectors. A simple, home-made teflon ferrule fitted in a swagelock nut is used for optical fiber feedthrough. (c) Telescope for relaying the image of the optical fiber tip to a CCD camera. The relay lens has a focal length of 20cm, and the Mitutoyo objective has a working distance of 3.3cm. (d) CCD image of a cleaved optical fiber tip above a sample. The fiber cladding's diameter is 125μm for an SMF-28 fiber.

focal length = 20cm is inserted to relay the fiber's image to the focal point of a 5x Mitutoyo objective (with long working distance). The setup is shown in Figure 2.6(c) with the imaged cleaved fiber tip hovering over a sample displayed in Figure 2.6(c).

A reflective film (e.g. aluminum foil, or white cardboard) is placed behind the optical fiber to improve image contrast by enhanced scattering.

Optical fiber feedthrough

Access of light to the inside of the vacuum chamber is enabled by using a swagelock nut fitted with a custom-made teflon ferrule [109]. A hole is bore through the ferrule which allows the optical fiber to feed into it. A good vacuum seal is obtained by tightening the swagelock nut.

Vacuum pumps

It suffices to attain a vacuum level as low as 10^{-3}Torr to observe the Brownian motion of the optomechanical devices. In our setup, we can reach 4×10^{-6}Torr. It is achieved by pumping the vacuum chamber with a turbo pump (Agilent TV-301 Navigator) backed by a roughing pump. Due to the sensitive nature of a fiber interferometer, the strong vibrations from the vacuum pump have to be damped out by connecting the vacuum lines to a heavy concrete mass. Otherwise the pump vibrations can lead to oscillatory amplitude as large as 10% of the detected signal.

Other maintenance issues

Finally, proper care of the vacuum chamber includes never exposing the inside of the vacuum chamber to the atmosphere with the chamber lid removed for an extended period of time. The nuts and bolts provided for tightening the chamber lid are *not necessary*. The heavy weight of the chamber lid is sufficient to ensure a good seal as the chamber is pumped. In fact the uneven tightening of the nuts and bolts can

warp the O-ring and lead to significant leak. Finally, with the inclusion of a good vacuum valve and assuming little virtual leak, a high vacuum with the pressure as low as 10^{-5}Torr can be maintained over two weeks without the vacuum pumps on.

Chapter 3

Optomechanics with photonic crystal membranes

3.1 Brief history of the project

In the development of an integrated platform for studying the Casimir force and counteracting it by optical means, we focused on the zeroth-order static effect of exerting an attractive optical force to a mechanically compliant membrane. We were interested in observing the nontrivial effect of the Casimir potential and an optical potential to the equilibrium position of the photonic crystal membrane [110]. The balance of the attractive potential due to the Casimir force and the optical force and the restoring mechanical spring force causes the development of bistable mechanical states. In particular, switching between these bistable states manifests itself as optical bistability. Another means of probing the effect of the Casimir force is to observe the Casimir-induced force gradient as the PhC membrane comes closer to the neighboring

substrate and experiences a stronger Casimir potential [100]. The initial phase of the investigation focused on eliminating and even taking advantage of the presence of compressive stress in silicon-on-insulator substrates which would otherwise prevent the formation of structures with sufficiently small gaps to probe the Casimir effect and achieve sufficiently large optical force. The breakthrough in stress engineering in turn achieved for us unprecedentedly wide tunability of optomechanical coupling strength for vertically coupled structures. Moreover, originally considered as negligible or irrelevant, the rich dynamics of optomechanics demanded proper characterization which had proved to provide us with realistic details for developing and actuating an on-chip Casimir oscillator. In this chapter, we report a full description of the optomechanical properties of our proposed Casimir membrane oscillator [1].

3.2 Stress-relief strategies for suspended thin silicon membranes and device fabrication

Our devices, illustrated in Fig. 3.1(a), consist of a square silicon PhC slab suspended by four support arms ≈ 250 nm above a Silicon-on-Insulator (SOI) substrate.[2] They are fabricated (Fig. 3.1(b)) from a double-SOI platform, formed by oxide-oxide bonding of two thermally oxidized SOI wafers. (See Appendix 1 for details of the fabrication of double-SOI wafers.) Here the sacrificial silicon dioxide layer between

[1] Most of the results shown in this chapter is joint work with Dr. David Woolf and Dr. Eiji Iwase, which are published in [34, 39]

[2] The sacrificial oxide layer in the second generation of double-SOI substrates is 100nm thick. Experimental results with devices fabricated with those platforms are reported in Chapter 4.

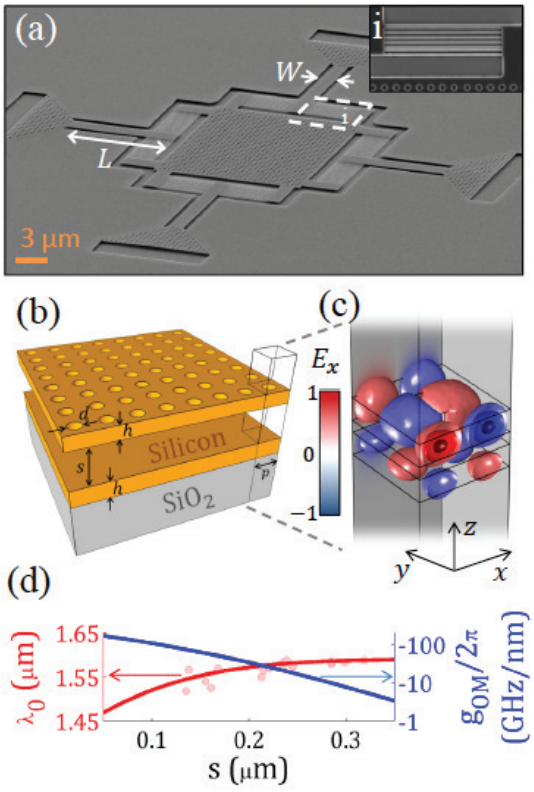

Figure 3.1: (a) An electron micrograph of a free-standing photonic crystal membrane, consisting of a silicon membrane (thickness h = 185nm) patterned with a square lattice with a 30×30 periodic hole array of period p = 0.92 μm and hole diameter d = 0.414 μm. The membrane is suspended over an SOI substrate (silicon device layer 185 nm thick; buried oxide layer 3 μm thick). The membrane is tethered by four arms (L = 19.3 μm, W = 2.75 μm) whose anchors are terminated by arrays of etch holes for engineering the torque due to stress gradient from the uneven oxide etch profile. On the ends close to the membrane the arms are supported by accordion-like structures (inset i). These combined features provide versatile lithographic control of membrane-substrate separations. (c) A 3D illustration of the simulated optical mode of a single unit cell of the geometry in (b) with s = 100 nm. The x-component of the electric field is plotted for an antibonding mode at λ_0=1570 nm. The field symmetry with respect to the plane parallel to the membrane and the substrate is antisymmetric which corresponds to a repulsive optical gradient force. (d) The simulated resonant wavelength λ_0 (red line) of the mode in (c) is plotted. Experimentally extracted resonant wavelengths of 16 devices with different membrane-substrate separations are overlayed over the simulated result. The corresponding optomechanical coupling coefficient of the mode is obtained from simulation (blue line).

the two silicon device layers is $s_0 = 265$ nm thick. Well known to the MEMS community, compressive stress in the device layer of SOI causes buckling to released devices. Moreover, due to the preferential hydrofluoric-acid etch along the bonded plane, the stress gradient along the sacrificial oxide layer leads to upward turning moments and deflects the released devices. Hence stress management techniques [111, 34] were incorporated which allow us to lithographically control the membrane-substrate gaps of various devices. The result is that vertical optomechanical strength tuning becomes possible which is otherwise hard to achieve controllably.

3.2.1 Effect of compressive stress to suspended photonic crystal membranes

In the development of suspended photonic crystal membranes for probing the Casimir effect, it is crucial that the membranes (i) remain flat (or have a very large radius of curvature) and (ii) maintain a small separation distance ($\leq$200nm) from the neighboring substrate for strong manifestation of the Casimir effect. Moreover, the photonic crystal membrane should be sufficiently large to reduce the finite-size effect on guided resonances and to allow a conspicuous exhibition of the Casimir force (scales directly with the interaction area). With these considerations, the photonic crystal membranes are designed to be about 30μm$\times30\mu$m large to accommodate sufficient number of periodically perforated holes, whereas the support arms are soft enough for the expression of the Casimir effect but strong enough to survive when subjected to large attractive potentials including the Casimir force, electrostatic force and optical force. Finally the membranes are supported by four identical arms to provide ample

mechanical support and reduce the membranes' torsional degrees of freedom.

Our starting substrate is a doubly-bonded silicon-on-insulator (SOI) wafer which consists of two thin silicon device layers (185nm thick) separated by a sacrificial oxide layer (265nm thick). In an ideal material, a photonic crystal membrane defined in the silicon device layer should remain flat upon release, and maintain a separation distance of 265nm from the bottom substrate. However, we identified that the compressive stress in the silicon device layer and the stress gradient at the material boundaries caused significant deviations from our designs.

The effect of the compressive stress is first demonstrated using typical commercial SOI wafers, on which an array of cantilevers and doubly clamped beams are fabricated. As shown in Figure 3.2(a), an array of cantilevers of different lengths appear to have rainbow colors along their lengths. In fact, the longest cantilever appears to be out of focused in the optical image. It is because of the large degree of buckling of the cantilever as the compressive stress is released which caused the free cantilever end to be out of the focal plane compared to other shorter cantilevers. As for the rainbow color, it is due to the interference of the white light illumination reflected from the top cantilever surface and the bottom substrate, where the separation between these surfaces vary continuously along the lengths due to the release of the compressive stress. Each repetition of the rainbow color roughly corresponds to changes in the cantilever-substrate separation by half the wavelength of the visible light. The implication of this demonstration is that without any stress-relief mechanism, the compressive stress in a tethered photonic crystal membrane is released toward the membrane itself as illustrated in the cartoon of Figure 3.2(e). It causes the mem-

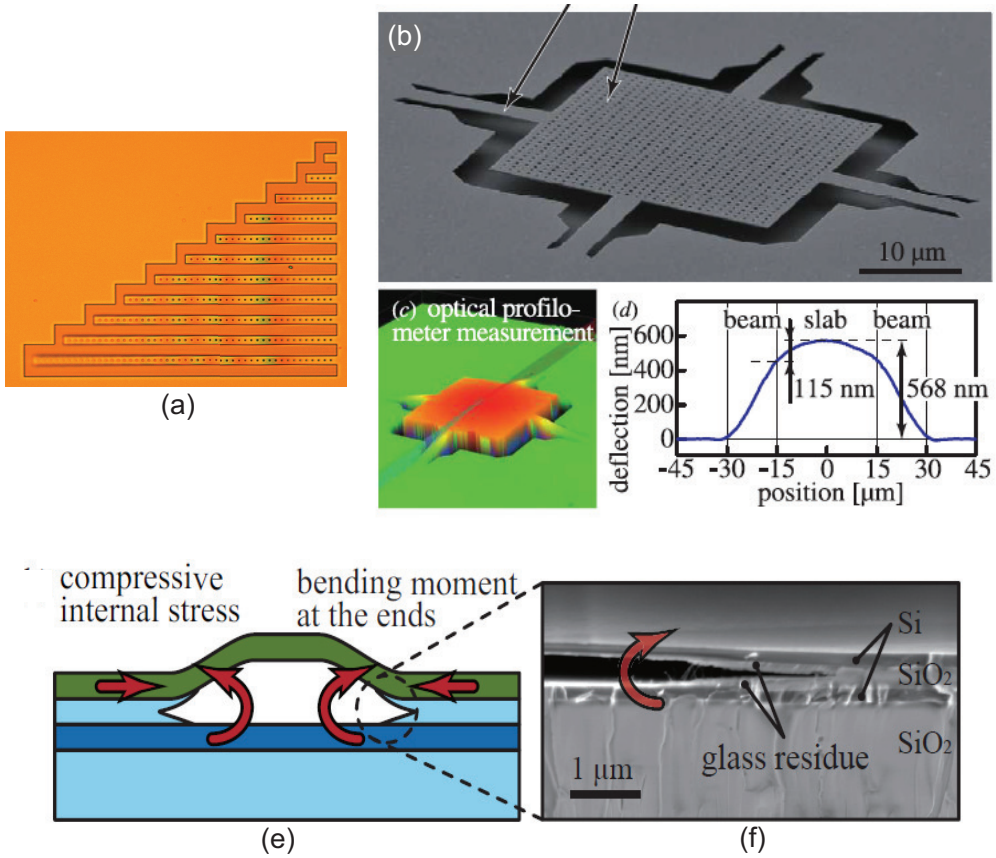

Figure 3.2: (a) Optical image of an array of cantilever of varying lengths to demonstrate the degree of buckling due to compressive stress in a silicon-on-insulator platform. The interference patterns across the beam lengths reflect the buckling amplitudes of the beams. (b) An electron micrograph of a suspended PhC membrane which is $30\times30\mu m^2$ large and supported by four arms without stress-relief designs. (c) 3D optical profiler image of the PhC membrane where the red color shows its upward deflection relative to the surrounding flat surfaces. (d) Quantitative measurement of the membrane's deflection through a cross section along the support beams and the slab. The slab is deflected upward by 568nm due to the release of the compressive stress toward the membrane.

brane to buckle (upward or downward) and become domed, which is illustrated in the scanning electron micrograph in Figure 3.2(b) and the optical profiler image in (c). Quantitatively measurement across the support beam and the membrane (Figure 3.2(d)) shows that the membrane is buckled upward by 568nm and is not flat across

the entire slab.

The prominent influence of the stress gradients, however, stems from the preferential etching of the silicon dioxide along the bonded oxide-oxide interface in a double-SOI platform. Figure 3.2(f) shows the electron micrograph of the cross section of a double-SOI wafer subjected to hydrofluoric acid immersion for ≈ 2 minutes. A widening crack between the two silicon device layers can be seen where some oxide residues with varying thickness are observed. The residue thickness gradient causes a stress gradient across the oxide layer which creates a bending moment on the released device layer. Figure 3.2(e) summarizes the stress-related sources acting on the top silicon membrane and how they each contribute to the out-of-plane deformation, i.e through the axial load and through the bending moment.

3.2.2 Strategies for mitigating in-plane compressive stress and stress gradients

We first tackle the issue of compressive stress. As a result of the in-plane compressive stress being released toward the suspended membrane, the membrane experiences out-of-plane buckling. Hence, a simple principle of eliminating the effect of compressive stress acting directly on the membrane is to provide an alternate pathway for the stress to be released in a preferential direction away from the membrane itself. This can be accomplished by introducing an array of thinner support structures which are more compliant, and hence preferentially subjected to the compressive stress which in turn experiences in-plane deformation instead. Two designs we adopted are support arms formed by (i) narrow curved beams and (ii) narrow lateral beams. How

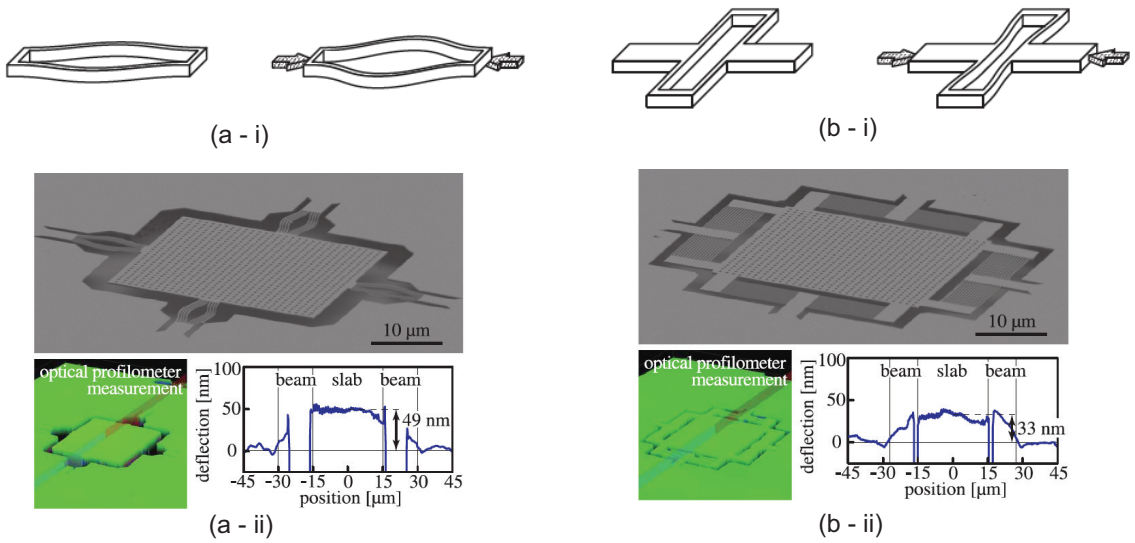

Figure 3.3: (a-i) Schematics of narrow curved beams subject to axial load which lead to in-plane deformation of the beams. (a-ii) Electron micrograph of PhC membranes with multiple narrow curved beams as support arms. The membrane's deflection profile is measured by a 3D optical profilometer. A cross-sectional profile along the support arms and the membrane is recorded, and shows a mere upward deflection of 49nm which is a huge decrease from the unmodified situation. (b-i) Schematics of narrow *lateral* beams subject to axial load which is perpendicular to the deformable beams' lengths. (b-ii) Electron micrograph of PhC membranes with multiple narrow lateral beams as support arms. Similarly, the membrane's deflection profile is measured. Here the recorded cross-sectional profile along the support arms and the membrane shows an upward deflection of 33nm.

the stress is relieved and causes in-plane deformation instead of out-of-plane buckling with these two designs are respectively illustrated with the cartoons in Figure 3.3(a-i) and (b-i). To maintain the out-of-plane stiffness of the support arms in the actual PhC membranes, a number of multiple narrow beams are placed parallel to each other in close proximity. The effectiveness of both stress-relief designs in drastically reducing the out-of-plane buckling of the PhC membranes is shown in Figure 3.3(a-ii) and (b-ii). The electron micrographs of PhC membranes supported by multiple narrow curved beams and by multiple narrow lateral beams depict the actual

mechanical designs. The degree of buckling of the membranes is inspected by a 3D optical profilometer. It is clear that the membranes are flat and leveled with respect to their surrounding blank surfaces of silicon. Quantitatively, the amount of buckling went from 568nm in the unmodified design to 49nm and 33nm respectively in the modified designs.

It should be noted that in the stress-relief design with multiple narrow curved beams, the support arms function both in allowing for mechanical deformation to relieve in the compressive stress and in providing the out-of-plane stiffness and mechanical support for the PhC membrane. For the other design with multiple narrow lateral beams, the deformable stress-relief features are perpendicular to the direction of the axial load due to the compressive stress, and are secondary in providing the out-of-plane stiffness and mechanical support to the PhC membrane. Throughout this thesis, we mostly adopted the the latter design for demonstrating the optomechanical properties and other nonlinear phenomena of the PhC membranes, but also demonstrated interesting optically induced mechanical nonlinear phenomena with the previous design.

Now we tackle the issue of stress gradients in double-SOI platforms. As discussed previously, the preferential etch of the oxide-oxide bonded interface, during the release of the PhC membrane in vapor hydrogen fluoride, causes a bending moment that tangentially torques the support arms and leads to large upward buckling of the PhC membrane. This is illustrated in Figure 3.4(a). One elegant solution is to isolate the bending moments from torquing the long support arms by placing an array of etch holes at the anchors. Now even the bending moments are still developed at the

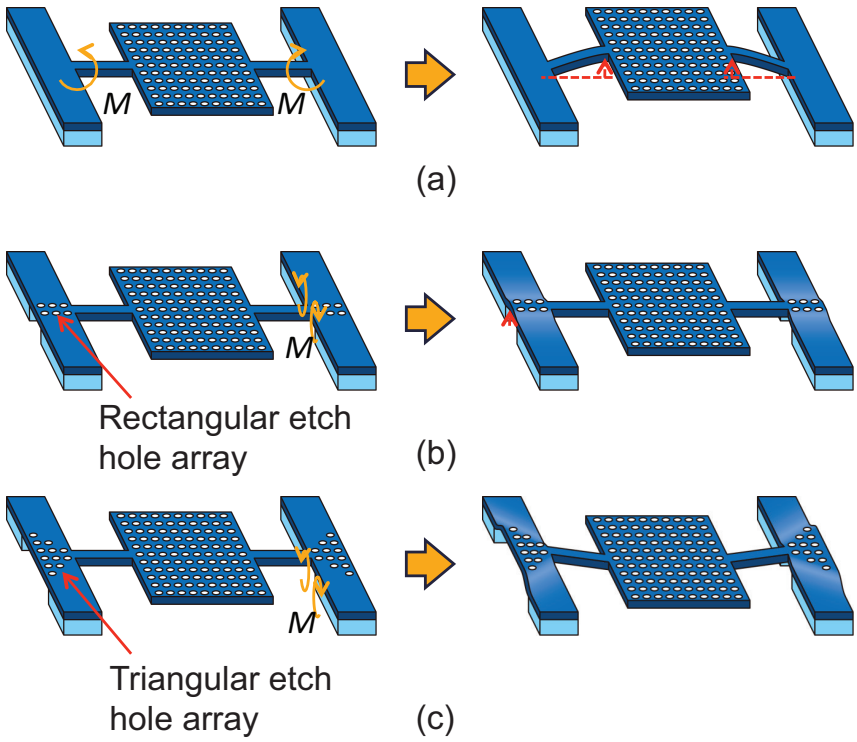

Figure 3.4: Control of membrane deflection by engineering the etch hole arrangement at the anchors.(a) For an unmodified structure, the bending moment caused by the stress gradient at the oxide-silicon interface leads to a large torque on the support arms, and hence a large degree of upward buckling of the membrane. (b) By adding in a rectangular array of etch holes at the end of the anchors, the bending moments are isolated from the support arms, but instead act on the small, stiff region of the etch holes. The membrane is expected to be leveled and flat with respect to its nearby surfaces. (c) It is also possible to create a torque gradient profile by arranging the etch hole array into a triangular shape. With the wide base of the triangle pointing away from the membrane, a net downward torque and hence a downward deflection of the membrane can be attained. Varying the width of the base of the triangle leads to controllable membrane deflection.

end of the etch hole arrays, the moments no longer act on the arms. Instead the moments are now rotated by 90° and act on the much stiffer released regions of the hole arrays. As a result, by placing a rectangular array of etch holes, the membrane's upward deflection is greatly reduced and the membrane-substrate separation can be kept small as a result. What is interesting is that one may arrange the etch holes into

a triangular array, as shown in the schematics in Figure 3.4(c). The torque developed at the wide triangular base is larger than that at the apex of the triangular array. This torque gradient leads to a net downward torque on the support arms of the membrane. Hence, the membrane is bent downward. By controlling the base width of the triangular array, the net torque on the support arms and hence the membrane downward deflection can be engineered. This feature opens up a new avenue of lithographically tunable optomechanical coupling in vertically coupled systems by engineering the geometry of the etch hole arrays at the anchors.

Combining the strategies discussed above including incorporating multiple narrow beams and engineering the anchor etch holes, we demonstrated control in membrane deflections with various etch hole arrangements in a double-SOI platform. Figure 3.5(a) and (b) correspond to the case where there is no stress-relief design or etch hole added. Optical profilometry reveals an upward buckling of 365nm. Figure 3.5(c) and (d) correspond to the case where multiple narrow lateral beams are added for stress relief and rectangular arrays of etch holes are placed at the anchors. Here the amount of upward deflection is merely 35nm. Figure 3.5(e) and (f) correspond to the case which is similar to the previous case but the etch holes at the anchors are arranged in a triangular form. The membrane is now deflected *downward* by 105nm. This versatile technique facilitates a systematic investigation of optomechanics with tunable coupling strength and other near-field interactions whose strengths of expression depend strongly on the membrane-substrate separations. As we will see in the following chapters, these stress-relief strategies were heavily employed in the fabrication of the structures studied throughout the thesis.

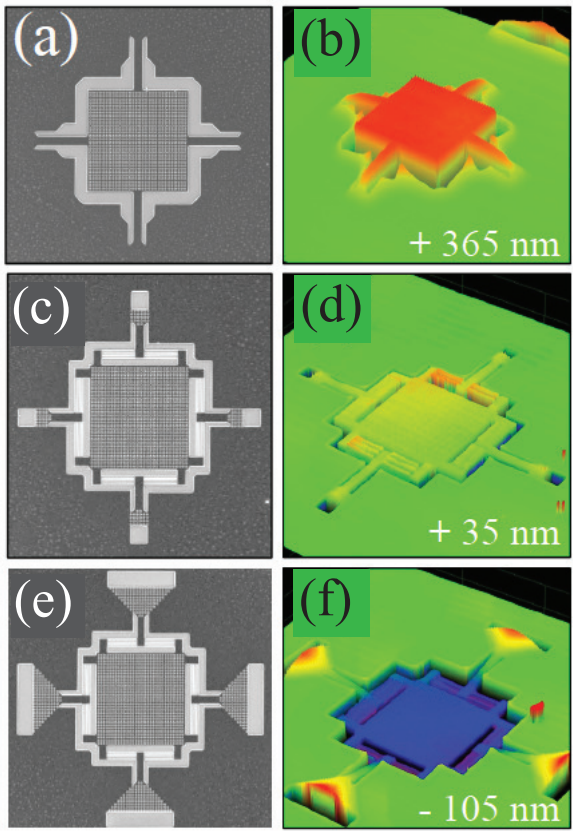

Figure 3.5: Comparison of the deflections of PhC membranes with different stress-relief and stress-gradient controls: (a) An SEM image of a PhC membrane with no stress-relief design or etch hole at the anchors. (b) The corresponding optical profiler image which shows an upward deflection of 365nm. (c) An SEM image of a PhC membrane where stress relief is achieved by incorporating multiple narrow lateral beams and the stress gradient is re-diverted by adding a rectangular array of etch holes. (d) The corresponding optical profiler image which shows a small upward deflection of 35nm. (e) An SEM image of a PhC membrane with similar stress-relief design but the etch holes at the anchors are arranged into triangular arrays. (f) The corresponding optical profiler image which shows a significant downward deflection of 105nm.

3.2.3 Device fabrication

The photonic crystal and other mechanical support patterns are defined by electron-beam lithography where a positive resist ZEP-520A is used. After developing in O-

xylene, the patterns are transferred to the top silicon layer by reactive-ion etch with a fluorine-based chemistry. The device is then released by undercutting the perforated silicon layer with the vapor-phase hydrofluoric acid etch (VHFE). (See Appendix 1 for reliable release techniques of VHFE.) In the demonstration of static displacement of the photonic crystal membrane due to the repulsive optical force which followed the initial investigation of the optomechanical properties and dynamics, an annealing step was performed at 500°C (slow thermal ramp) for 1 hour in a nitrogen environment to the same device [3]. The results are enhanced optical and mechanical quality factors. The separations of the released membranes from the substrate are characterized by a laser confocal microscope (Olympus LEXT OLS-4000). (Typical interferometry-based optical profilometers common to characterizing microscopic structures do not apply to our devices due to the presence of multiple thin layers compared to the interrogating wavelengths.)

3.3 Device characterization

The structure was designed to support an optical antibonding mode in the wavelength range of 1480-1680nm that results from the hybridization of waveguide modes in the membrane and substrate [32, 34]. The precise spectral location of the resonance is determined by the optomechanical coupling between the two modes, the strength of which is defined as $g_{OM} \equiv d\omega/ds$, where ω is the optical resonant frequency. The distribution of the x-component of the electric field in the top membrane is out-of-

[3]Pre-annealing and post-annealing measurements were performed on 18 devices. Quantitatively the mechanical linewidths of chosen devices went from 111Hz, 536Hz and 344Hz to 27Hz, 42Hz and 40Hz respectively.

phase from that in the bottom membrane, as depicted in the simulation results of the whole structure in Fig. 3.1(c), which corresponds to the generation of a repulsive gradient force. Additionally, the field symmetries along the x-z and y-z planes indicate that we are operating with a "dark" mode [112], which theoretically does not couple to normally incident light because of mismatch in field symmetry. However, by breaking the periodicity of the full structure, we can couple to the dark mode and achieve high Q_{opt} [113]. Such devices have been the subject of numerous theoretical and experimental investigations on subjects ranging from the lowering of the laser thresholds [114] to increasing the sensitivity of photonic-crystal-based sensors [115]. Here, the dark mode is made accessible due to the finite size of the membrane and slight fabrication imperfection.

The experimental setup to interrogate the optomechanical properties of the coupled photonic crystal membranes is as follows: An optical fiber (SMF-28) mounted on a z-axis linear stage (stepper motor) couples light to the PhC membrane by centering it above the suspended membrane in the Rugar configuration (shown in Figure 3.6, inset i) [104]. The same fiber also collects the light reflected by the device. (See Ch. 2 for experimental details and analysis of fiber interferometry.) The chip containing the device rests on a sample holder whose in-plane alignment is by a four-axis (x, y, θ_x, θ_y) stage platform. The motorized x-y stage (stepper motor) contains closed-loop feedback for repeatable alignment of the fiber to the sample with sub-100 nm resolution, where the manual θ_x and θ_y tilt controls are adjusted to attain parallelism between the fiber facet and the sample. Such proper alignment procedures ensure maximum coupling efficiency. The typical fiber-substrate height is approximately 25 μm (Figure

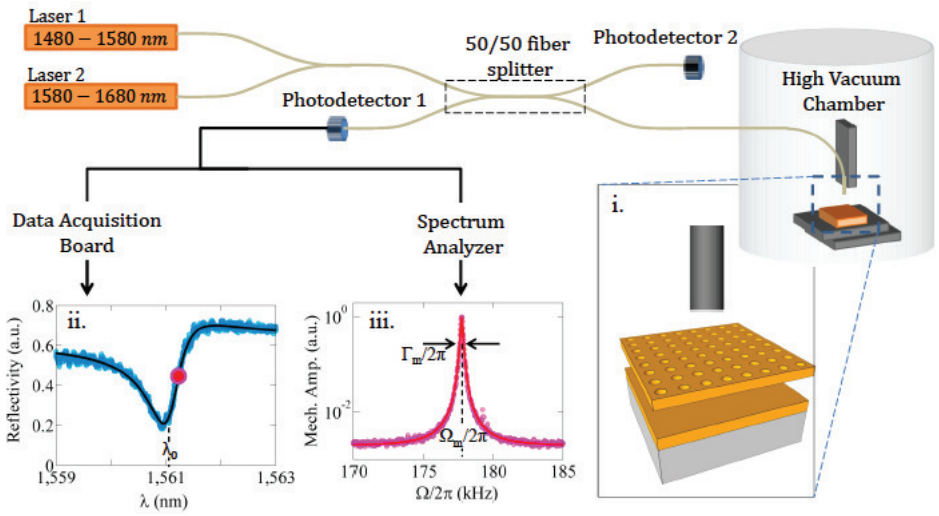

Figure 3.6: Experimental setup: A 2×1 fiber coupler, which admits two separate laser inputs covering the wavelength range of 1480-1680nm (tunable laser TSL500), is spliced to a 50/50 2×2 fiber coupler. One end goes to Photodetector 2 as a power reference. The other end is fed into the vacuum chamber through a customized fiber port. The cleaved optical fiber is mounted vertically and positioned above the PhC membrane, as illustrated in inset (i). The reflected signal of the PhC membrane is collected by the same end and is measured by Photodetector 1. The optical spectra are collected by a data acquisition board. An optical resonance centered at λ_0=1561.1nm is shown in inset (ii) (quality factor = 2500). The mechanical spectra are obtained by measuring the frequency fluctuations of the optical signal, transduced by the mechanical motion. The photodetector signal is sent to a real-time spectrum analyzer to characterize the membrane's mechanical response in the frequency domain. A mechanical spectrum of the membrane fundamental mode (measured at 1561.2nm - shoulder of the optical resonance (red dot in inset (i)) is shown in inset(ii).

3.6, inset i) corresponding to a spot size of approximately 12 μm. The whole setup is placed inside a high vacuum chamber (10^{-5} Torr) to reduce the effect of viscous damping on the detection of mechanical resonances. Optical spectra (Figure 3.6, inset ii) were collected with a fast, low-noise near-IR photodetector (ThorLabs DET10C) by sweeping the wavelengths of tunable laser sources (TSL-510). Mechanical spectra (Figure 3.6, inset iii) were collected at fixed excitation wavelengths on either side of the optical resonance by analyzing the signal reflected off of our membranes in a

real-time spectrum analyzer (Tektronix RSA3303B).

3.4 Dynamic behavior

3.4.1 Optical spring and dynamic backaction

Since the optical force has a nonlinear dependence on the membrane-substrate separation x [31], the optical force can contribute to alter the system's spring constant [116, 13]. This can be easily visualized by Taylor-expanding the expression of the optical force to obtain a Hooke's-law-like term. Alternately it is simply the first-order derivative of the optical force expression. Since the optical force is dependent on the detuning from the optical resonance, the optical spring constant's magnitude and polarity depend on the optical detuning of the excitation. It is evident that the optical spring constant scales linearly with the excitation power as well.

What is unconventional is the occurrence of dynamic backaction which is a consequence of the finite time needed for building up of the optical forces [13]. In our system, there are two optical forces, namely the repulsive gradient force and the photothermal force. The photothermal force arises as a result of the finite linear absorption of the incident light which heats up the suspended PhC membrane. As the heat diffuses away from the membrane to the support arms, thermal stress is formed at the silicon and oxide interface due to the difference in thermal conductances. In the case of a photothermal force, the time needed for heat to be transported for thermal stress to reach to its maximum is on the scale of the thermal time constant which is geometry and material dependent [29, 117]. In the case of an optical gradient force,

the time scale for the build-up of the effect is related to the photon lifetime limited by available dissipative channels. In any case, the non-instantaneous nature of these forces that traverse from point A to B then back to A leads to positive/ negative work done on the optomechanical structure. This is the basis of optomechanical amplification/ cooling [118, 119]. Such effect is manifested as mechanical linewidth narrowing/ broadening which means the viscous damping on the system is reduced/ enhanced. We probe the optical spring effect and dynamic backaction in our system by pumping the membrane with light over a range of excitation wavelengths across the optical resonance, maintained at a certain power. We then measure the resultant mechanical frequencies and mechanical linewidth of the transduced Brownian motion, which corresponds to the fundamental flexural mode of two devices of different membrane-substrate separations. As illustrated in Figure 3.7(a)(and (b)), the membrane that deflects upward (downward) has a separation of 300nm (160nm), which is enabled by stress and torque engineering at the anchors. Their corresponding resonant wavelengths (optical quality factors) are 1576.4nm (6600) and 1561nm (4000) and has the characteristic of an anti-bonding mode (repulsive force). The effect of optical spring (mechanical frequency Ω_m shifts from the unperturbed frequency) and dynamic backaction (change in the mechanical linewidth Γ_m) is extracted by fitting the measured mechanical resonance to a Lorentzian lineshape motivated by the mechanical susceptibility of a classical harmonic oscillator. The best fits for Ω_m and Γ_m are plotted in Figure 3.7(a) and (b) (green circles) as a function of excitation wavelength. Both membranes experience mechanical linewidth broadening when the excitation is red-detuned from the optical resonance and linewidth narrowing when blue-detuned. In

particular, while self-sustained oscillations, accompanied by linewidth narrowing to its fundamental minimum, are supposed to occur on the blue-detuned side of the optical resonances in a fast optomechanical system [118], we observed self-sustained oscillations on the red-detuned side when the membrane is excited above the threshold power (deflected-downward: $\approx 15\mu$W; deflected-upward: $\approx 60\mu$W). This is directly opposite to what is expected in systems subjected to back-action from fast optical forces only. Therefore, we conclude that in our system most of the linewidth change is accounted for by the photothermal force.

With respect to the mechanical frequency shifts, in the deflected-upward case, mechanical softening occurs on the blue-detuned side of the resonance and stiffening occurs on the red-detuned side. The reverse effect happens in the deflected-downward case. Both the gradient force and the photothermal force have comparable contribution to the mechanical frequency shift depending on their relative strengths. In the deflected-downward case, the two silicon layers become more strongly coupled, hence the gradient force per photon greatly increases relative to the photothermal force. Since the back-action due to the fast gradient force dominates, we recover the expected trend in the mechanical frequency shifts with respect to detuning in optomechanics with a fast optical force.

To conclude the experimental resutls, typical optomechanical systems whose dynamics are subjected to the back-action of a fast optical gradient force or radiation pressure, the optical spring effect leads to mechanical stiffening and linewidth narrowing when the excitation is blue-detuned from the optical resonance, whereas softening and linewidth broadening occur when red-detuned. However, when the system is also

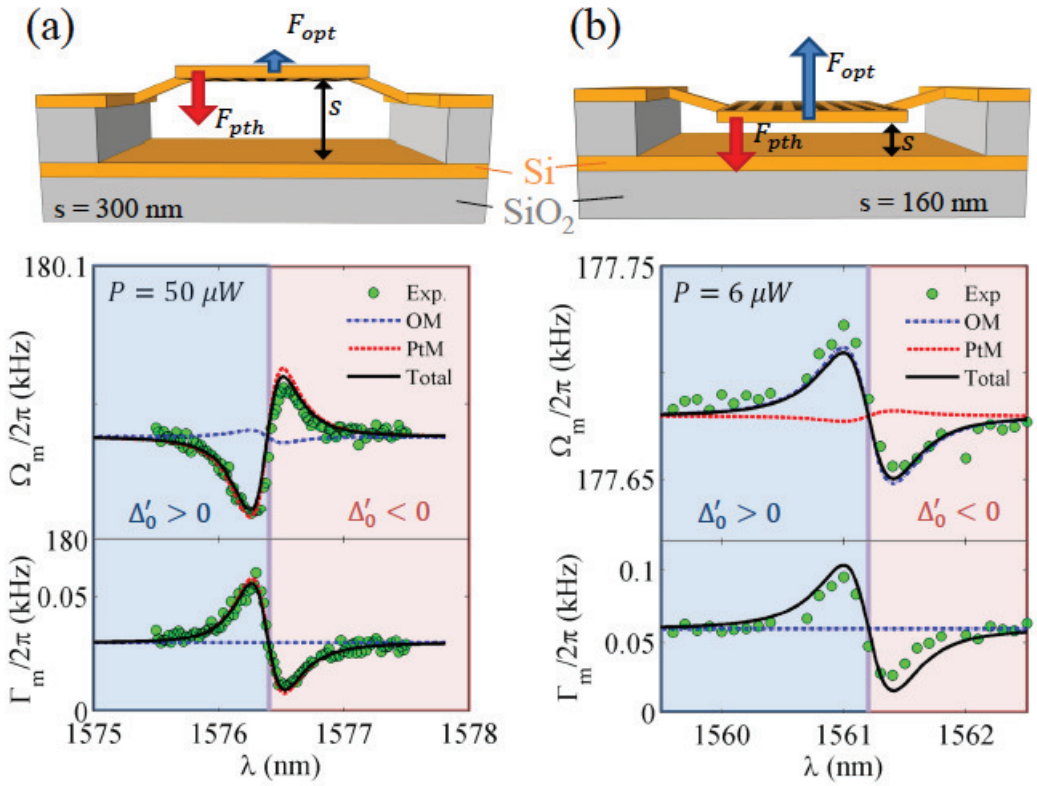

Figure 3.7: Interplay of optical gradient force and photothermal force in the optical spring effect and dynamic back-action: (a) Photonic crystal membrane deflected upward (with a membrane-substrate separation of s=300nm) experiences both the repulsive optical gradient force F_{opt} and the attractive photothermal force F_{ptm}. The fitted value of mechanical frequency $\Omega_m/2\pi$and linewidth Γ_m of the membrane, upon excitations of P=50μW at different optical wavelengths across the optical resonance centered at 1576.4nm, are plotted (green circles). Δ_0' denotes optical detuning. The experimental results are fitted to Eqs. 3.21 (black solid line). The contributions due to the gradient force (blue dashed line "OM") and the photothermal force (red dashed line "PtM"). (b) Photonic crystal membrane deflected downward (s=160nm). Here the measurements are performed with P=6μW. Note that the trend of the mechanical frequency in the downward-deflected case flips compared to the upward-deflected case, when the membrane becomes more strongly coupled and the optomechanical coupling strength is enhanced. The mechanical linewidth change is practically entirely due to the photothermal effect.)

subjected to the back-action of a retarded photothermal force, the optical spring effect with respect to optical detuning could be reversed. The net optomechanical dynamics

is a result of the competition between the optical gradient force and photothermal force which are of very different timescales (e.g. ≈1ps of gradient force vs. ≈10μs of photothermal force). By designing the optomechanical coupling and the timescale of the photothermal force, one can tune the dynamics of the oscillator. For our PhC membrane system, the dynamic backaction effect due to the optical gradient force is negligible or below the detection limit because of the moderate quality factor of the optical modes. By taking into account the contribution from the photothermal force, we elucidate the interplay of the optical gradient force and the photothermal force on the dynamics of the membranes in the framework of coupled-mode theory [120].

3.4.2 Coupled-mode theory for the dynamics of optomechanics in the presence of the optical gradient force and the photothermal force

In this model, the thermomechanical force F_{ptm}, driving our membrane together with the optical gradient force F_{opt}, is added to the equation of motion. F_{ptm} is modelled to be directly proportional to the temperature increase T of the membrane as a result of the absorption of stored optical energy $|a(t)|^2$. Since it is important to account for the delay in the thermomechanical force due to its finite heat diffusion time, the Newton's cooling law is included to describe the intricate dynamics of heat with optics and mechanics. The three governing equations of our optothermomechanical

system are given by

$$\frac{da}{dt} = -\frac{\Gamma}{2}a - i(\Delta_0 + g_{OM}x - \frac{d\omega}{dT}T)a + \kappa s \tag{3.1}$$

$$\begin{aligned}\frac{dT}{dt} &= -\gamma_{th}T + c_{th}^{-1}(\Gamma_{lin} + \Gamma_{TPA})|a|^2 \\ &= -\gamma_{th}T + c_{th}^{-1}(\Gamma_{lin} + \sigma\frac{\beta_{Si}c^2}{V_{TPA}n_g^2}|a|^2)|a|^2\end{aligned} \tag{3.2}$$

$$\frac{d^2x}{dt^2} + \Gamma_m\frac{dx}{dt} + \Omega_m^2 x = -\frac{g_{OM}|a|^2}{m^*\omega_0} + \frac{D}{m^*}T. \tag{3.3}$$

In the equation for the time evolution of the intracavity field a given by Eqn 3.1, $a(t)$ is the time-dependent intra-cavity field stored in the PhC, Γ is the total decay rate of the field due to the external coupling rate κ, the linear absorption by the PhC Γ_{lin} and two-photon absorption Γ_{TPA} which proves to be negligible, Δ_0 is the optical tuning of the excitation light from the optical resonance of the PhC, g_{om} is the optomechanical coupling coefficient, $\frac{d\omega}{dT}$ is the thermo-optic coefficient of silicon, and $|s|^2$ gives the input power of the excitation light. The first term on the right-hand side of the Eqn 3.1 describe the total decay (out-coupling) of the intra-cavity field. The second term accounts for the dispersion of the PhC resonance due to the optomechanical effect and the thermo-optic effect. The last term is the coupling of external excitation into the PhC.

As for the equation for the time evolution of the temperature increase $T(t)$ of the PhC given by Eqn 3.2, γ_{th} is diffusion time constant of heat in the PhC, c_{th} is the specific heat capacity of silicon, σ is the cross-section area for two-photo absorption, c is the speed of light, n_g is the group index of light in silicon, β_{Si} is the bulk silicon two-photon absorption coefficient, V_{TPA} is the effective volume of the mode that contributes to two-photon absorption. The equation essentially accounts for heat loss

by diffusion (first term on the right-hand side) and heat input to the PhC due to non-radiative processes.

Finally, in the equation of motion of PhC given by Eqn 3.3, $x(t)$ is the time-dependent displacement of the membrane, Γ_m is the mechanical decay constant, Ω_m is the angular mechanical frequency, m^* is the effective mass of the membrane with respect to the fundamental mode, ω_0 is the resonant frequency of the PhC, and D is a coefficient that relates the magnitude of the photothermal force to the temperature increase T and has the unit of N/K. The terms on the right-hand side of the equation of motion accounts for the two forcing terms due to the optical gradient force and the photothermal force.

Assuming a small perturbation in the membrane's position around its equilibrium, we linearize the equations above by separating out the static and the time-varying components of $x(t)$, $a(t)$ and $T(t)$ by the ansatz $x(t) = x_0 + \delta x(t), a(t) = a_0 + \delta a(t), T(t) = T_0 + \delta T(t)$.

Linearizing the intracavity field equation (3.1)

$$\begin{aligned}&\frac{d}{dt}(a_0+\delta a(t))\\&=-\frac{\Gamma}{2}\left(a_0+\delta a(t)\right)-i\left[\Delta_0+g_{OM}\left(x_0+\delta x(t)\right)-\frac{d\omega}{dT}\left(T_0+\delta T(t)\right)\right]\left(a_0+\delta a(t)\right)+\kappa s\end{aligned} \tag{3.4}$$

$$\Rightarrow\begin{cases}0 &= -\frac{\Gamma}{2}a_0-i\left(\Delta_0+g_{OM}x_0-\frac{d\omega}{dT}T_0\right)a_0+\kappa s\\ \frac{d}{dt}\delta a(t) &= -\frac{\Gamma}{2}\delta a(t)-i\left(g_{OM}\delta x(t)-\frac{d\omega}{dT}\delta T(t)\right)a_0-i(\Delta_0+g_{OM}x_0-\frac{d\omega}{dT}T_0)\delta a(t)\end{cases} \tag{3.5}$$

Define $\Delta_0' = \Delta_0 + g_{OM}x_0 - \frac{d\omega}{dT}T_0$. Working in the Fourier domain (where $\frac{d}{dt} \to -i\omega$)

$$\begin{cases}a_0 = \dfrac{\kappa s}{\frac{\Gamma}{2}+i\underbrace{\left(\Delta_0+g_{OM}x_0-\frac{d\omega}{dT}T_0\right)}_{\Delta_0'}}\\ \left(-i\omega+i\Delta_0'+\Gamma/2\right)\delta a(\omega) = -i(g_{OM}\delta x(\omega)-\frac{d\omega}{dT}\delta T(\omega))a_0\end{cases} \tag{3.6}$$

$$\Rightarrow\boxed{\begin{cases}a_0 = \dfrac{\kappa s}{\frac{\Gamma}{2}+i\Delta_0'}\\ \delta a(\omega) = \dfrac{-i\left(g_{OM}\delta x(\omega)-\frac{d\omega}{dT}\delta T(\omega)\right)}{-i(\omega-\Delta_0')+\Gamma/2}a_0\end{cases}} \tag{3.7}$$

The quantity $a_0\delta a^*(\omega)+a_0^*\delta a(\omega)$, soon to be crucial for the rest of the calculation,

is evaluated to be

$$a_0\delta a^*(\omega)+a_0^*\delta a(\omega)=|a_0|^2\left[\frac{i(g_{OM}\delta x(\omega)-\frac{d\omega}{dT}\delta T(\omega))}{-i(\omega+\Delta_0')+\Gamma/2}+\frac{-i(g_{OM}\delta x(\omega)-\frac{d\omega}{dT}\delta T(\omega))}{-i(\omega-\Delta_0')+\Gamma/2}\right]$$

$$=i|a_0|^2\left(g_{OM}\delta x(\omega)-\frac{d\omega}{dT}\delta T(\omega)\right)\left[\frac{1}{-i(\omega+\Delta_0')+\Gamma/2}-\frac{1}{-i(\omega-\Delta_0')+\Gamma/2}\right] \tag{3.8}$$

$$=-|a_0|^2\left(g_{OM}\delta x(\omega)-\frac{d\omega}{dT}\delta T(\omega)\right)\frac{2\Delta_0'}{(\Gamma/2-i\omega)^2+\Delta_0'}$$

Note that in (3.8), the expression in the square brackets has the property of $f(-\omega)=-f^*(\omega)$.

Linearizing the Newton's cooling law (3.2)

$$\begin{aligned}
&\frac{d}{dt}\left(T_0+\delta T(t)\right)\\
&=-\gamma_{th}\left(T_0+\delta T(t)\right)+c_{th}^{-1}\Gamma_{lin}(a_0+\delta a(t))(a_0^*+\delta a^*(t))\\
&\qquad+\frac{c_{th}^{-1}\sigma\beta_{Si}c^2}{V_{TPA}n_g^2}\left(a_0^2+2a_0\delta a(t)\right)\left(a_0^{*2}+2a_0^*\delta a^*(t)\right)\\
&=-\gamma_{th}\left(T_0+\delta T(t)\right)+c_{th}^{-1}\Gamma_{lin}(|a_0|^2+a_0\delta a^*(t)+a_0^*\delta a(t))\\
&\qquad+\frac{c_{th}^{-1}\sigma\beta_{Si}c^2}{V_{TPA}n_g^2}\left(|a_0|^4+2|a_0|^2(a_0\delta a^*(t)+a_0^*\delta a(t))\right)
\end{aligned}$$

Working in the Fourier space,

$$\begin{cases}
0= & -\gamma_{th}T_0+c_{th}^{-1}\Gamma_{lin}|a_0|^2+c_{th}^{-1}\sigma\dfrac{\beta_{Si}c^2}{V_{TPA}n_g^2}|a_0|^4\\
\dfrac{d}{dt}\delta T & =-\gamma_{th}\delta T\\
& +c_{th}^{-1}\left(\Gamma_{lin}+\dfrac{\sigma\beta_{Si}c^2|a_0|^2}{V_{TPA}n_g^2}\right)(a_0\delta a^*+a_0^*\delta a)
\end{cases} \tag{3.9}$$

$$\Rightarrow \boxed{\begin{cases} T_0 = |a_0|^2 \dfrac{c_{th}^{-1}}{\gamma_{th}} \left(\Gamma_{lin} + \dfrac{\sigma \beta_{Si} c^2}{V_{TPA} n_g^2} |a_0|^2 | \right) \\ \delta T(\omega) = \dfrac{c_{th}^{-1} \left(\Gamma_{lin} + \dfrac{2\sigma \beta_{Si} c^2}{V_{TPA} n_g^2} |a_0|^2 | \right)}{-i\omega + \gamma_{th}} \left(a_0 \delta a^*(\omega) + a_0^* \delta a(\omega) \right) \end{cases}} \tag{3.10}$$

Linearizing the equation of motion (3.3)

$$\begin{aligned} &\frac{d^2}{dt^2}\delta x(t) + \Gamma_m \frac{d}{dt}\delta x(t) + \Omega_m^2 (x_0 + \delta x(t)) \\ &\qquad = -\frac{g_{OM}}{m^* \omega_0} \left(|a_0|^2 + a_0 \delta a^*(t) + a_0^* \delta a(t) \right) + \frac{D}{m^*} (T_0 + \delta T(t)) \end{aligned}$$

$$\begin{cases} \Omega_m^2 x_0 = -\dfrac{g_{OM} |a_0|^2}{m^* \omega_0} + \dfrac{D}{m^*} T_0 \\ \dfrac{d^2}{dt^2}\delta x(t) + \Gamma_m \dfrac{d}{dt}\delta x(t) + \Omega_m^2 \delta x(t) = -\dfrac{g_{OM}}{m^* \omega_0} \left(a_0 \delta a^*(t) + a_0^* \delta a(t) \right) + \dfrac{D}{m^*} \delta T(t) \end{cases} \tag{3.11}$$

$$\Rightarrow \boxed{\begin{cases} x_0 = \dfrac{1}{m^* \Omega_m^2} \left[-\dfrac{g_{OM} |a_0|^2}{\omega_0} + \dfrac{D}{m^*} T_0 \right] \\ \delta x(\omega) = \dfrac{\left[-\dfrac{g_{OM}}{m^* \omega_0} (a_0 \delta a^*(\omega) + a_0^* \delta a(\omega)) + \dfrac{D}{m^*} \delta T(\omega) \right]}{-\omega^2 - i\Gamma_m \omega + \Omega_m^2} \end{cases}} \tag{3.12}$$

Sieving out the optical spring effect and dynamical backaction

In (3.12), the dynamics of the membrane motion has an explicit contribution from the dynamics of light, proportional to $a_0 \delta a^*(t) + a_0^* \delta a(t)$, and from the dynamics of temperature, proportional to $\delta T(t)$. The calculation can be performed by assuming $\delta x(t) = cos(\Omega_m t)$, work in the Fourier domain and express the quantities $a_0 \delta a^*(\omega) + a_0^* \delta a(\omega)$ and $\delta T(\omega)$ in terms of $\delta x(\omega)$. Manipulating the expressions in the Fourier

domain, one should be able to identify an in-plane component and a quadrature component that correspond to $cos(\Omega_m t)$ and $\Omega_m sin(\Omega_m t)$.

Contribution from the gradient force

To relate (3.8) to $\delta x(\omega)$, one needs to express $\delta T(\omega)$ in terms of $a_0\delta a^*(\omega)+a_0^*\delta a(\omega)$ using (3.10).

$$\begin{aligned} &a_0\delta a^*(\omega) + a_0^*\delta a(\omega) \\ &\quad = i|a_0|^2\left[\frac{1}{\Gamma/2 - i(\omega+\Delta_0')} - \frac{1}{\Gamma/2 - i(\omega-\Delta_0')}\right] \\ &\quad\quad \times \left[g_{OM}\delta x(\omega) - \frac{d\omega}{dT}\frac{c_{th}^{-1}\left(\Gamma_{lin} + \frac{2\sigma\beta_{Si}c^2}{V_{TPA}n_g^2}|a_0|^2\right)}{-i\omega+\gamma_{th}}\left(a_0\delta a^*(\omega) + a_0^*\delta a(\omega)\right)\right] \end{aligned} \tag{3.13}$$

$$\begin{aligned} &a_0\delta a^*(\omega) + a_0^*\delta a(\omega) \\ &= \frac{ig_{OM}|a_0|^2\delta x(\omega)}{\left[\frac{1}{\Gamma/2 - i(\omega+\Delta_0')} - \frac{1}{\Gamma/2 - i(\omega-\Delta_0')}\right]^{-1} - i|a_0|^2\frac{d\omega}{dT}\frac{c_{th}^{-1}\left(\Gamma_{lin} + \frac{2\sigma\beta_{Si}c^2}{V_{TPA}n_g^2}|a_0|^2\right)}{-i\omega+\gamma_{th}}} \end{aligned} \tag{3.14}$$

Define $H(\omega, \Delta_0', |a_0|^2)$

$$= \frac{1}{\left[\frac{1}{\Gamma/2 - i(\omega+\Delta_0')} - \frac{1}{\Gamma/2 - i(\omega-\Delta_0')}\right]^{-1} - i|a_0|^2\frac{d\omega}{dT}\frac{c_{th}^{-1}\left(\Gamma_{lin} + \frac{2\sigma\beta_{Si}c^2}{V_{TPA}n_g^2}|a_0|^2\right)}{-i\omega+\gamma_{th}}}$$

which possesses the properties of $f(-\omega) = -f^*(\omega)$. This allows us to reduce (3.14) to

$$a_0\delta a^*(\omega) + a_0^*\delta a(\omega) = -ig_{OM}|a_0|^2 H(\omega)\delta x(\omega). \tag{3.15}$$

Here, replace $x(\omega)$ with $x(\omega) = \frac{1}{2}(\delta(\omega - \Omega_m) + \delta(\omega + \Omega_m))$. The quantity $a_0\delta a^*(\omega) + a_0^*\delta a(\omega)$ peaks at $\omega = \pm\Omega_m$.

$$\begin{aligned} a_0\delta a^*(\omega) + a_0^*\delta a(\omega) &= -\frac{i}{2}g_{OM}|a_0|^2\left(H(\Omega_m)\delta(\omega-\Omega_m) + H(-\Omega_m)\delta(\omega+\Omega_m)\right) \\ &= -\frac{i}{2}g_{OM}|a_0|^2\left(H(\Omega_m)\delta(\omega-\Omega_m) - H^*(\Omega_m)\delta(\omega+\Omega_m)\right) \\ &= -\frac{1}{2}g_{OM}|a_0|^2\left[iRe[H(\Omega_m)](\delta(\omega-\Omega_m) - \delta(\omega+\Omega_m)) - Im[H(\Omega_m)](\delta(\omega-\Omega_m) + \delta(\omega+\Omega_m))\right] \end{aligned} \tag{3.16}$$

Converting back into the time domain,

$$\boxed{a_0\delta a^*(t) + a_0^*\delta a(t) = -g_{OM}|a_0|^2\left[\frac{Re[H(\Omega_m)]}{\Omega_m}\delta\dot{x}(t) - Im[H(\Omega_m)]\delta x(t)\right]}. \tag{3.17}$$

Contribution from the thermomechanical force

We could repeat the same procedure of separating out the in-plane and quadrature components in the previous section for $\delta T(t)$, but one has to be careful with the front factor of $\dfrac{1}{-i\omega + \gamma_{th}}$ in (3.10). Substituting the results in (3.16),

$$\begin{aligned} \delta T(\omega) =& \frac{c_{th}^{-1}\left(\underbrace{\Gamma_{lin} + \frac{2\sigma\beta_{Si}c^2}{V_{TPA}n_g^2}|a_0|^2|}_{\tilde{\Gamma}_{abs}}\right)}{-i\omega + \gamma_{th}}\left(a_0\delta a^*(\omega) + a_0^*\delta a(\omega)\right) \\ =& \frac{i}{2}c_{th}^{-1}\tilde{\Gamma}_{abs}|a_0|^2 g_{OM}\left[\frac{H(\Omega_m)\delta(\omega-\Omega_m)}{-i\Omega_m + \gamma_{th}} + \frac{H(-\Omega_m)\delta(\omega+\Omega_m)}{i\Omega_m + \gamma_{th}}\right] \end{aligned} \tag{3.18}$$

$$
\begin{aligned}
&= -\frac{c_{th}^{-1}\tilde{\Gamma}_{abs}|a_0|^2 g_{OM}}{2i}\left[\frac{H(\Omega_m)\delta(\omega-\Omega_m)}{-i\Omega_m+\gamma_{th}} - \frac{H^*(\Omega_m)\delta(\omega+\Omega_m)}{i\Omega_m+\gamma_{th}}\right] \\
&= -\frac{c_{th}^{-1}\tilde{\Gamma}_{abs}|a_0|^2 g_{OM}}{2i(\Omega_m^2+\gamma_{th}^2)}\times \\
&\quad\left[\Big((\gamma_{th}Re[H(\Omega_m)]-\Omega_m Im[H(\Omega_m)])+i(\Omega_m Re[H(\Omega_m)]+\gamma_{th}Im[H(\Omega_m)])\Big)\delta(\omega-\Omega_m)\right. \\
&\quad\left.-\Big((\gamma_{th}Re[H(\Omega_m)]-\Omega_m Im[H(\Omega_m)])-i(\Omega_m Re[H(\Omega_m)]+\gamma_{th}Im[H(\Omega_m)])\Big)\delta(\omega+\Omega_m)\right] \\
&= -\frac{c_{th}^{-1}\tilde{\Gamma}_{abs}|a_0|^2 g_{OM}}{\Omega_m^2+\gamma_{th}^2}\left[\Big(\gamma_{th}Re[H(\Omega_m)]-\Omega_m Im[H(\Omega_m)]\Big)\frac{\delta(\omega-\Omega_m)-\delta(\omega+\Omega_m)}{2i}\right. \\
&\quad\left.+\Big(\Omega_m Re[H(\Omega_m)]+\gamma_{th}Im[H(\Omega_m)]\Big)\frac{\delta(\omega-\Omega_m)+\delta(\omega+\Omega_m)}{2}\right] \qquad (3.19)
\end{aligned}
$$

Converting back into the time domain,

$$
\begin{aligned}
&\delta T(t) = c_{th}^{-1}\tilde{\Gamma}_{abs}|a_0|^2 g_{OM}\times \\
&\qquad\left[\delta\dot{x}(t)\frac{\gamma_{th}Re[H(\Omega_m)]-\Omega_m Im[H(\Omega_m)}{\Omega_m(\Omega_m^2+\gamma_{th}^2)} + \delta x(t)\frac{\Omega_m Re[H(\Omega_m)]+\gamma_{th}Im[H(\Omega_m)}{\Omega_m^2+\gamma_{th}^2}\right] \qquad (3.20)
\end{aligned}
$$

Putting everything together,

$$
\begin{cases}
\Delta\Omega_m^2 = -\dfrac{g_{OM}^2|a_0|^2}{m^*\omega_0}Im[H(\Omega_m)] - \dfrac{D}{m^*}c_{th}^{-1}\tilde{\Gamma}_{abs}|a_0|^2 g_{OM}\dfrac{\Omega_m Re[H(\Omega_m)]+\gamma_{th}Im[H(\Omega_m)]}{\Omega_m^2+\gamma_{th}^2} \\
\Delta\Gamma_m = \dfrac{g_{OM}^2|a_0|^2}{m^*\omega_0}\dfrac{Re[H(\Omega_m)]}{\Omega_m} - \dfrac{D}{m^*}c_{th}^{-1}\tilde{\Gamma}_{abs}|a_0|^2 g_{OM}\dfrac{\gamma_{th}Re[H(\Omega_m)]-\Omega_m Im[H(\Omega_m)]}{\Omega_m(\Omega_m^2+\gamma_{th}^2)},
\end{cases} \qquad (3.21)
$$

where $H(\omega, \Delta_0', |a_0|^2)$

$$
= \frac{1}{\left[\dfrac{1}{\Gamma/2-i(\omega+\Delta_0')} - \dfrac{1}{\Gamma/2-i(\omega-\Delta_0')}\right]^{-1} - i|a_0|^2\dfrac{d\omega}{dT}\dfrac{c_{th}^{-1}\left(\Gamma_{lin}+\frac{2\sigma\beta_{Si}c^2}{V_{TPA}n_g^2}|a_0|^2\right)}{-i\omega+\gamma_{th}}}
$$

and $\tilde{\Gamma}_{abs} = \Gamma_{lin} + \dfrac{2\sigma\beta_{Si}c^2}{V_{TPA}n_g^2}|a_0|^2$.

Having the expressions derived for the mechanical frequency and linewidth change as a function of excitation wavelengths in the presence of the optical gradient force, photothermal force and the thermo-optic effect, we fitted our experimental data shown in Figure 3.7(a) and (b). The individual contributions from the gradient force and the photothermal force are plotted explicitly. Γ_e and Γ are extracted by fitting to the optical resonance. g_{om} is obtained from simulations. Γ_{th} is obtained experimentally. Here we neglected two-photon absorptions due to large mode volumes of guided resonances and hence low optical intensity.

3.4.3 Photothermal cooling

On the blue-detuned side of the optical resonance, the photothermal force does negative work to the optomechanical system which effectively further damps the mechanical motion of the membrane. Experimentally we observe an increase in the linewidth of the mechanical resonance concerned as the power of the pumping light increases. To extract the effective temperature of the cooled mechanical mode, one could perform a simple calculation invoking the equipartition theorem and the fluctuation-dissipation theorem and obtain a simple expression relating the mechanical linewidth and the mode's effective temperature. Alternately, one may opt to use the area under the curve of the transduced signal to calibrate the effective temperature. Here the details of the transduction mechanism are presented to obtain a proper understanding of the normalization procedure.

With an input light of power P_{in}, the reflected power from the photonic crystal is simply $R(\Delta)P_{in}$ where R is the reflectance of the PhC depending on the optical

detuning Δ. The reflected light is converted into a photodetector signal, which will then be sent to a spectrum analyzer that outputs the frequency spectrum of the photodetector signal. One should note that the frequency spectrum obtained reveals the *power* spectrum density (multiplied with the detection window bandwidth) of the photodetector signal. Hence the amplitude of the power spectrum density scales linearly with the square of P_{in}. As a result, to obtain the frequency response of the displacement noise of the photonic crystal which is embedded in R, one has to normalize the measured frequency spectrum by P_{in}^2. In the case of simple optomechanical transduction with negligible optical spring or dynamic backaction, the power spectra detected with varying input powers, though appear to drammatically increase in the signal strength measured at the spectrum analyzer, should all overlap after being normalized by P_{in}^2.

Here we discuss how the displacement fluctuation $x(t)$ is embedded in the reflectance R. Due to the optomechanical coupling, any displacement leads to an optomechanical dispersion $g_{om}x(t)$ in the optical resonance. Hence the displacement fluctuation leads to optical frequency fluctuation, which is measured as fluctuation in the reflectance. We may relate the change in the reflectance to the displacement fluctuation by the following algebraic manipulation [63]:

$$dR(t) = \frac{dR}{d\Delta}\Delta(t) = -g_{om}\frac{dR}{d\Delta}x(t) \tag{3.22}$$

where g_{om} is the optomechanical coupling. Consider an underdamped harmonic oscillator driven by thermal noise. We may write the following equation of motion [121]:

$$\frac{d^2x}{dt^2} + \Gamma_m\frac{dx}{dt} + \Omega_m^2 x \quad = f_L(t) \tag{3.23}$$

, where the subscript L of $f_L(t)$ denotes the Langevin force due to the thermal bath. Note that the thermal Langevin force averages to zero in time, i.e. $< f_L(t) >_t = 0$, and is delta-correlated in time as a white noise, i.e.

$$< f_L(t) f_L(t+\tau) >_t = 2 m_{eff} \Gamma_m k_B T \delta(\tau), \tag{3.24}$$

where m_{eff} is the effective motional mass for each mechanical mode concerned, k_B is the Boltzmann constant, T is the mode temperature and τ is the time lag of the thermal force. From the equipartition theorem, the root-mean-squared oscillation amplitude driven by the thermal force at temperature T is related by $\frac{1}{2} m_{eff} \Omega_m^2 \int dt < |x(t)|^2 >= \frac{1}{2} k_B T$. To infer the mode's temperature, we need to calibrate $\int dt < |x(t)|^2 >$ which is equivalent to finding $\int d\Omega |x(\Omega)|^2$ by the Parseval's theorem. Since experimentally we have access to the frequency response of the displacement fluctuation, we now work in the frequency domain. From (3.23), we obtain

$$\left[-\Omega^2 - i\Omega\Gamma_m + \Omega_m^2 \right] x(\Omega) = f_L(\Omega)/m \tag{3.25}$$

with the correlation function for the Langevin force given by $< f_L(\Omega) f_L(\Omega') >= 4\pi m_{eff} \Gamma_m k_B T \delta(\Omega + \Omega')$. To calculate $\int d\Omega |x(\Omega)|^2$, one first obtains the power spectral density of the displacement fluctuation:

$$\begin{aligned} S_{xx}(\Omega) &= \int d\Omega' \, \langle x(\Omega) x(\Omega') \rangle \\ &= \int d\Omega' \frac{< F_L(\Omega) F_L(\Omega') > /m^2}{(\Omega_m^2 - \Omega^2 - i\Omega\Gamma_m)(\Omega_m^2 - \Omega'^2 - i\Omega'\Gamma_m)} \\ &= \frac{2\pi \Gamma_m k_B T}{m \Omega_m} \frac{1}{(\Omega_m - \Omega)^2 + (\Gamma_m)^2}. \end{aligned} \tag{3.26}$$

By integrating $S_{xx}(\Omega)$ over the entire frequency range, we should retrieve the equipartition theorem. What this implies experimentally is that finding the area under the curve of a optomechanically transduced Lorentzian response obtains for us the mode's temperature, off by a proportionality constant that accounts for the photodetector conversion factor, electrical signal transmission efficiency and the factors in Eq. 3.22. However, for evaluating a mode's new effective temperature as a result of photothermal cooling upon stronger optical excitation, holding all other experimental parameters constant, there are two methods of calibration which eliminates the need for the proportionality constant. First, we notice that S_{xx} peaks at $\Omega = \Omega_m$ from Eq. 3.26, and evaluates to be $S_{xx}(\Omega_m) = \frac{2\pi k_B T}{m\Omega_m\Gamma_m}$. Upon photothermal cooling, Γ_m increases and Ω_m changes (due to both optical gradient force and the photothermal force in our system). These two parameters can be fitted and the relative amplitude of $S_{xx}(\Omega = \Omega_m)$ can be read off experimentally. With the proper normalization procedure (i.e. dividing out the factor of P_{in}^2), the relative temperature of the mode concerned at different pump powers can then be calibrated by comparing the ratio of the peak amplitudes. Second, we may write

$$\frac{k_B T_{eff}}{k_B T_0} = \frac{\Omega_{meff}^2(P_{in})}{\Omega_{m0}^2} \frac{|x_\Omega(P_{in})|^2}{|x_\Omega(P_{in} \approx 0)|^2} \tag{3.27}$$

$$\rightarrow \qquad \frac{T_{eff}}{T_0} = \frac{\Gamma_{m0}}{\Gamma_{meff}}. \tag{3.28}$$

This shows that by merely knowing the mechanical linewidth, we may calibrate the effective mode temperature.

Here we evaluate the extent of photothermal cooling in our optomechanical system. For the purpose of clearer illustration, the extensive data set chosen refers to a device whose mechanical frequency is 256.3kHz. The PhC membrane is pumped

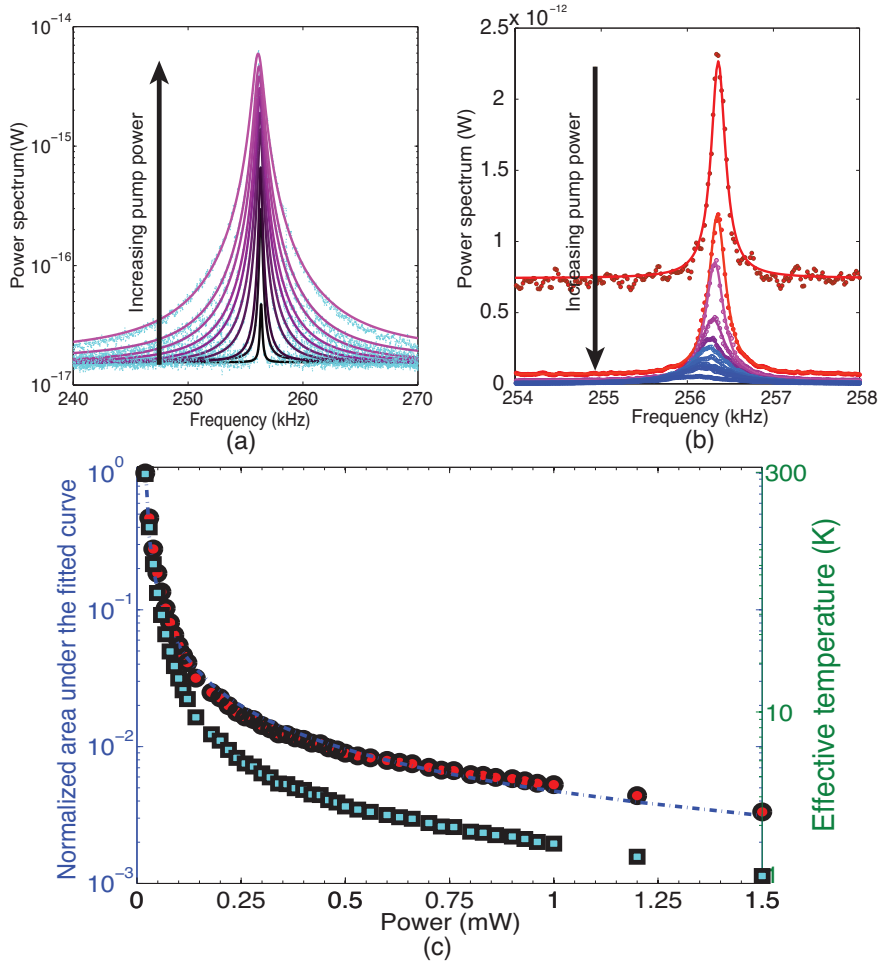

Figure 3.8: Evaluation of photothermal cooling: (a) Raw mechanical spectra of the PhC membrane pumped at 1608.8nm (blue-detuned from resonance) at increasing optical powers up to 345μW. The overal amplitude increases and the linewidth broadens as the pump power increases. Cyan dots are the experimental data where the purple lines are Lorentzian fits to the data to extract the mechanical linewidth. (b) Mechanical spectra of the membrane normalized by the square of the excitation powers. While the linewidth remains broadened, the overall amplitude decreases dramatically as the pump power increases (from red to purple to blue). (c) Integrated area under the curve (red squares) over various pump powers of the cooling laser, normalized by the area obtained at the lowes pump power. The corresponding effective temperature is plotted on the right axes (green squares). Note the x-axis refers to the power directly from the laser; it should be scaled by a factor of 0.23 to obtain the true excitation powers to the membrane.

by laser light with increasing excitation powers of the wavelength of 1608.8nm, blue-detuned from the optical resonance. The frequency response at each pump power is recorded and plotted accordingly in Figure 3.8(a). As discussed above, the frequency response is expected to rise in overall amplitude and the mechanical linewidth broadens. However, to reveal the true relative amplitude of the thermal motion, we apply the calibration technique delineated previously to obtain Figure 3.8(b). It shows that the frequency response indeed increases upon stronger excitations, signifying blue-detuned optical cooling. To calibrate the temperature of the mode for each pump power, we first evaluate the area under the Brownian peak for each measured spectrum. We obtain an effective temperature as low as 1 Kelvin with a cooling laser power of 345μW, starting from room temperature.

3.4.4 Self-oscillations mediated by photothermal force

On the red-detuned side of the optical resonance, the photothermal force now does positive work to the optomechanical system which reduces the damping the membrane experiences. In Figure 3.9(a-c), the mechanical spectra of the membrane excited at 1609.3nm (red-detuned from the optical resonance) with 1.59μW, 73.53μW and 276μW are shown. The mechanical linewidths of the spectrum taken with increasing pump powers are plotted in Figure 3.9(e). The effective mechanical linewidth decreases linearly with the excitation power, as shown in Eq. 3.21 until it reaches a minimum bounded by a relation similar to the Schawlow-Townes linewidth in laser theory. As the power increases further, the membrane undergoes self-oscillation where a continuous-wave excitation causes it to oscillate as a free oscillator without damp-

ing. Another lasing-like signature we observe is in the amplitude of the mechanical peak as a function of pump power: The amplitude increases drastically by orders of magnitude as the membrane excitation transits from below-threshold to above-threshold power. As the threshold is crossed, the amplitude increases linearly. Note that the oscillator is now in an out-of-equilibrium state where the analysis with the equipartition theorem breaks down.

As the PhC membrane undergoes self-oscillation, harmonics of the fundamental peaks appear. While it could be a result of nonlinear mechanics, it could also be due to the nonlinear transduction of the mechanical motion. The nonlinear transduction occurs when the optomechanical coupling strength is so large that the self-oscillations cause dispersion in the optical resonances by more than an optical linewidth and the probe wavelength is away from its initial linear quiescent point. One may distinguish between the two effects by probing with an optical resonance with lower g_{om}.

3.5 Static behavior: Optical bistability and hysteresis

Rapid developments in the field of optomechanics have opened up avenues for fundamental research on quantum state manipulation with macroscopic structures [26] and show promise for optomechanical sensors [63] and technologies for both radio-frequency [77, 78] and telecom applications.[70] While most attention has been devoted to compact structures featuring low (picogram) mass and ultrahigh-frequency (gigahertz) mechanical modes,[122, 120] the technological implications of static defor-

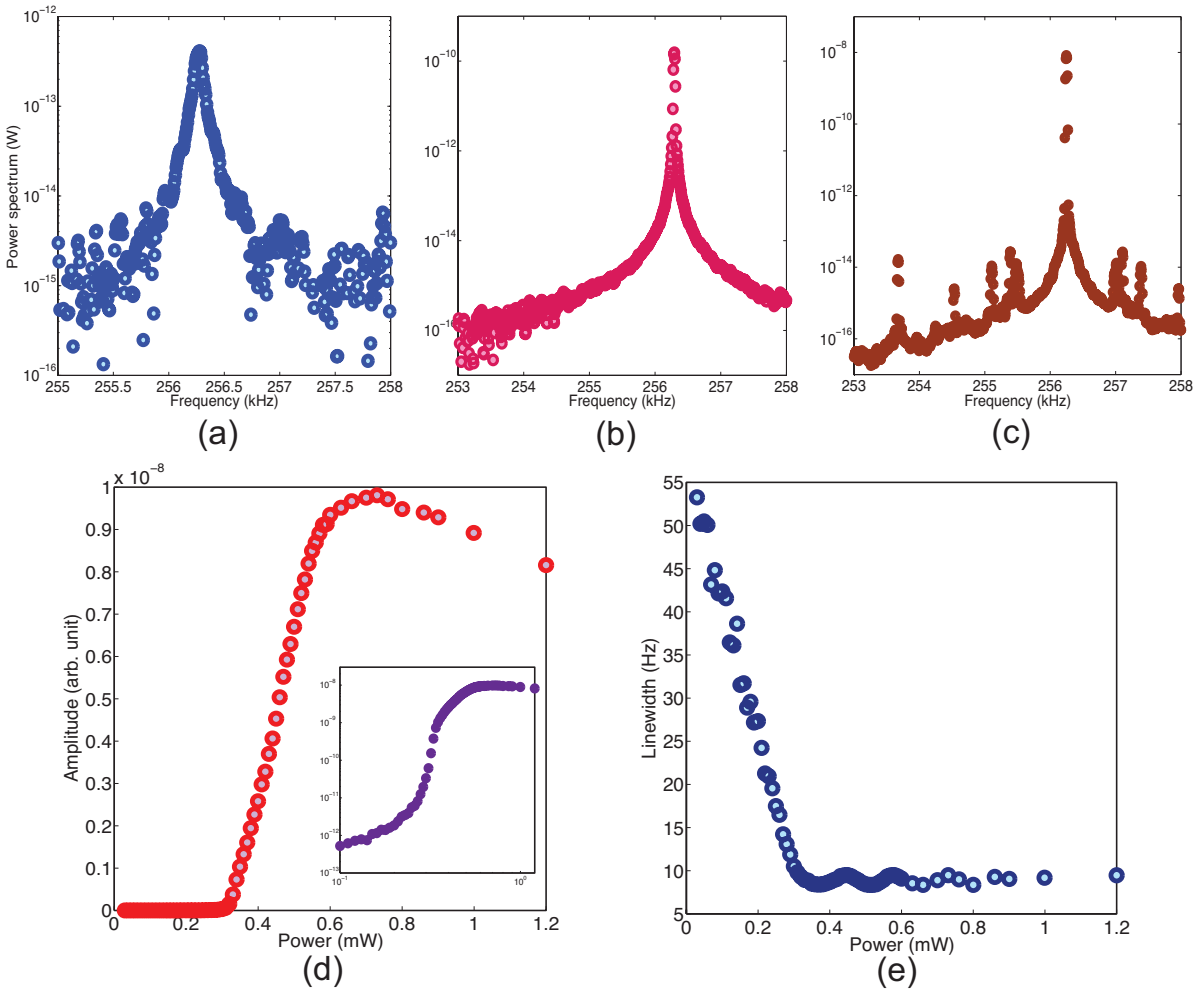

Figure 3.9: Self oscillations mediated by photothermal force: Mechanical spectra of the membrane pumped at 1609.3nm (red-detuned) with (a) 1.59μW, (b) 73.53μW and (c) 276μW. (d) The peak amplitudes of the mechanical spectra are extracted and plotted against the pump powers in the linear scale. A clear threshold behavior where the amplitude response is drastically enhanced akin to lasing is observed. The extrapolated threshold power is 86μW. Above the threshold power, the peak amplitude increases linearly with the pump power until $\approx$ 0.6mW, likely due to significant optomechanical and photothermal dispersion. Inset shows the same data in the logarithm scale. (e) Mechanical linewidths fitted/ approximated plotted against the pump power. The linewidth decreases linearly as the pump power increases and eventually saturates at a minimum value. Note the x-axis of both (d) and (e) refers to the power directly from the laser; it should be scaled by a factor of 0.23 to obtain the true excitation powers to the membrane.

mation due to optical forces have been less explored.[17] In coupled photonic waveguide geometries,[31, 14] bonding and anti-bonding optical modes are supported and the corresponding attractive and repulsive optical forces exerted on a pliant structure (low mechanical frequency) could serve to broaden the range of motion of integrated microelectromechanical devices. This translates to improvement in the detection range of pressure and displacement sensors and the actuation range of electrostatic actuators. In particular, the pull-in limit of electrostatic actuators could be extended by increasing the plate separation with a repulsive optical force. Additionally, schemes for preventing stiction, which occurs when attractive forces like the Casimir force and electrostatic force become overwhelmingly large compared to the mechanical restoring force, have been proposed [84] using a real-time monitoring of the structure's displacement and a counteracting feedback repulsive force (of the order of nano-Newtons and linear with excitation power). In this paper, we demonstrate nanometer-pulling of a thin silicon photonic crystal (PhC) membrane under low vacuum with a repulsive optical gradient force and an attractive photo-thermo-mechanical force. Furthermore, optical bistability induced by optical forces and thermo-optic effect is observed at large excitation powers.

The high Q_{opt} of the dark mode, together with the mode's large optomechanical coupling coefficient $g_{OM}/2\pi = -23$ GHz/nm (at $s_0 = 220.6nm$), boosts the strength of the optical force and hence the range of actuation. A low power (25 μW) wavelength sweep is shown in the inset of Fig. 3.10(d) (red curve) taken with a free-space resonance scattering setup in a low vacuum condition described in Fig. 3.10(d), revealing a cavity resonance centered at $\lambda_0 = 1581.55$ nm. To account for interference

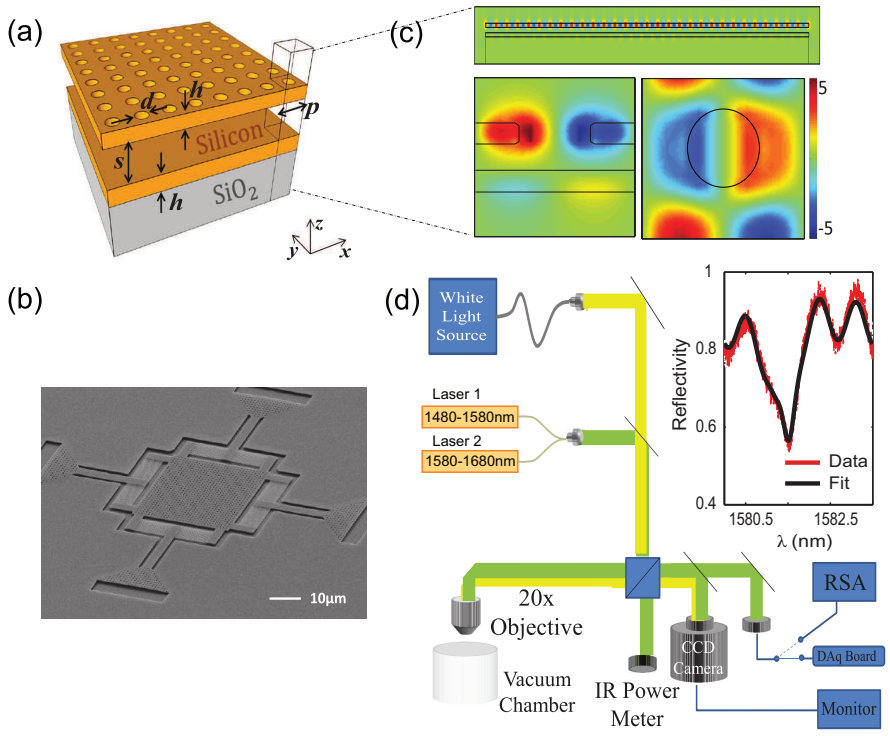

Figure 3.10: (a) Schematic of membrane geometry consisting of a suspended silicon membrane above a silicon-on-insulator substrate. The top membrane is perforated by a 30×30 array of holes with diameter d = 0.414μm and period p= 0.92μm. Both silicon layers have thickness h = 185 nm. The width of the membrane is 27.6 μm on each side. (b) An electron micrograph of a device. (c) Top diagram shows the FDTD simulated E_x field profile for the antibonding mode at $\lambda_0 = 1584.85$ nm in the vertical cross-section of the full structure. Bottom left diagram shows the zoomed-in view of E_x field profile in the vertical cross-section of a unit cell. Bottom right diagram shows the E_x field profile in the horizontal cross-section of a unit cell, revealing the mode to be a dark mode. (d) Free-space coupling setup. A white-light source and output from a near-IR laser are combined and sent through a 50-50 beam splitter, sending half of the signal to an IR power meter and half through a 20x objective placed above a vacuum chamber. The reflected signal is sent back through the beam splitter and can be directed onto a CCD camera allowing us to carefully align the laser spot to the membrane and to a photodetector (PD) to collect optical spectra via the DAq board and mechanical spectra via the real-time spectrum analyzer (RSA). Inset at right shows the reflection spectrum of the device around the resonance centered at $\lambda_0 = 1581.55$ nm.

fringes from parasitic reflections, we carefully fit both the optical resonance and the oscillating background (black line) to an expression which has the form

$$R = |r|^2 = \left| r_d(\lambda) e^{-i\phi} + \frac{\kappa_e}{-i\Delta_0 + \kappa/2} \right|^2 \tag{3.29}$$

where $r_d(\lambda)$ is the background reflectivity, ϕ is the relative phase between the underlying background reflection and the optical cavity, κ is the full-width half-max linewidth of the optical resonance, κ_e is the external coupling rate. Δ_0 is the detuning (expressed in frequency) of the sweep wavelength from λ_0. Fitting parameters correspond to an optical cavity with $\kappa_e = 0.3\kappa$ and $Q_{opt}^{tot} = \omega_0/\kappa = 3400$.

As previously described[84], the potential of a mechanical harmonic oscillator with equilibrium position s_0, when perturbed by the potential of an optical "spring" [123] centered at s_l for a laser wavelength λ_l can create a multi-well potential with two stable mechanical equilibria. The transition between these mechanical equilibria is reflected by the occurrence of optical bistability, due to the the dependence of the resonance frequency on s. Yet the direct observation of the optomechanically-induced optical bistability can easily be obscured in actual systems by other competing mechanisms including the thermo-optic effect due to two-photon absorption, free-carrier dispersion and the Kerr nonlinearity[16]. We designed our geometry to minimize these effects by exciting a guided resonance which is delocalized throughout the PhC membrane. We estimate the total mode volume to be $\approx 260(\lambda/n_g)^3$ from simulation. Due to its large modal volume, the thermal and electronic nonlinearities (which scale inversely with the modal volume) are dramatically reduced. This is in contrast with many of the optomechanical structures being studied, which have modal volumes $\approx (\lambda/n_g)^3$ and

where thermal nonlinearities could be readily observed at even modest input powers. Here with the coupled PhC membrane of the current separations, optomechanical detuning is larger than thermo-optic detuning that originates from linear absorption due to defects introduced during the fabrication processes, which is two orders of magnitude larger than the intrinsic material absorption of bulk silicon.

We solve for the the optical and mechanical equilibria in the presence of the thermo-optic effect within the coupled-mode theory framework [13]. In particular, the stored optical energy in the system $|a|^2$ is given by

$$|a|^2 = \frac{\kappa_e}{(\kappa/2)^2 + \Delta^2} P_{in} \tag{3.30}$$

where P_{in} is the power incident on the structure, and κ_e/κ represents the fraction of incident power coupled into the cavity. The detuning Δ of the laser excitation frequency ω_l from the perturbed optical resonant frequency can be written as

$$\Delta = \omega_l - [\omega_0 + (d\omega/dT)\Delta T + g_{OM}\Delta x]. \tag{3.31}$$

The third term in Eq. 3.31 is the thermo-optic detuning, with $d\omega/dT = (d\omega/dn)(dn/dT)$, n is the refractive index of silicon, $d\omega/dn$ is obtained from simulations and approximately $-2\pi \times 10^{14}$ Hz and dn/dT is the thermo-optic coefficient of silicon equal to $2 \times 10^{-4} K^{-1}$.[124] The absorbed optical power and hence the temperature change of the system is given by

$$\Delta T = \frac{\Gamma_{abs}|a|^2}{C_{th}\kappa_t} \tag{3.32}$$

where Γ_{abs} is the absorption coefficient of the system, C_{th} is the heat capacity, κ_t

is the thermal diffusion rate. The fourth term in Eq. 3.31 is the optomechanical detuning. In particular, the displacement of the membrane due to the respective photo-thermo-mechanical force and the repulsive gradient force is given by

$$\Delta x = \frac{D\Delta T}{K} + \frac{|a|^2 g_{OM}}{\omega_l K} \tag{3.33}$$

where K is the spring constant of the mechanical resonator and D is the thermal-mechanical force coefficient in units of Newtons per Kelvin.[125] We neglect the Duffing nonlinearity in our mechanical model as the extent of the optical actuation is still well within the linear regime for our structures: the amplitude is much less than the membrane thickness ($185nm$) and the compressive stress in the silicon device layer is alleviated by thin accordion structures as shown in Fig. 3.10(b). The above equations can be solved self-consistently to yield Δ and hence the perturbed optical resonant frequency $\omega_0' = \omega_0 + (d\omega/dT)\Delta T + g_{OM}\Delta x$ at a given ω_l and P_{in}.

The values of $\lambda_0' = 2\pi c/\omega_0'$ at which solutions of Eq. 3.31 exist are plotted in Fig. 3.11, as a function of laser wavelength $\lambda_l = 2\pi c/\omega_l$ for incident powers of 0.275 mW (green line), 0.775 mW (blue line), 1.275 mW (red line), 1.525 mW (purple line), 1.775 mW (orange line) and 2.275 mW (black line). The unperturbed optical resonance occurs at $\lambda_0 = 1581.55$ nm. The dashed portions of the curves correspond to unstable equilibria. At high powers, a clear bistable region exists in which there are two stable configurations of the membrane for fixed power and laser wavelength, due to both optomechanical and thermo-optic detunings whose magnitudes are comparable. The boundaries of the bistable region are denoted by λ_f and λ_b, representing the hysteretic transition wavelengths for a laser swept forward (left to right) and backward (right

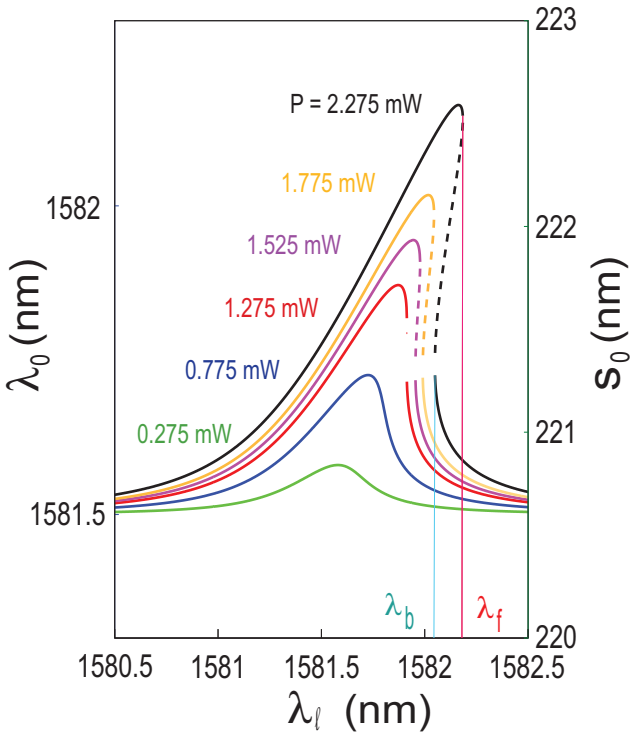

Figure 3.11: Calculated stable locations of the optical resonance as a function of laser wavelength, for six optical powers: 0.275 (green line), 0.775 (blue line), 1.275 (red line), 1.525 (purple line), 1.775 (orange line) and 2.275 mW (black line). At $P \geq 1.275$ mW, the system has three solutions (two stable – solid line, one unstable – dashed line) for a certain range of wavelengths. Due to the intracavity-power dependence of optical detunings from optomechanical and thermo-optic effects, the system is bistable in this wavelength range, and displays hysteresis when the laser is swept continuously from short to long wavelengths (forward sweep) or vice versa (backward sweep). Two hysteretic transition points occur at λ_f for the forward sweep and λ_b for the backward sweep.

to left) across the resonance.

We can model the reflectance of the system as a function of laser wavelength at multiple powers ($P = 0.275$ mW to 2.275 mW - same powers as in Fig. 3.11) with Eq. 3.29 (with Δ_0 replaced by Δ_0') and the respective equilibria calculated in Fig. 3.11. The results are shown in Fig. 3.12(a) (offset for clarity), and are compared to our experimental observations shown in Fig. 3.12(b). The experimental data were

collected by sweeping the tunable laser output from short to long wavelength (red curve) and then back (blue curve) at a fixed tuning speed of 1 nm/s. We find excellent agreement between experiment and theory, which display an overall redshift of the mode and increasing hysteresis at higher powers. In particular, we directly compare the locations of the forward and backward bistable jumps, λ_f and λ_b respectively, in Fig. 3.12(c). The locations of these transitions were extracted from the data shown in Fig. 3.12(b) by finding the minima of the reflectivities of forward and backward wavelength sweeps at each power. We see strong agreement between experiment (red/ blue circles) and theoretical predictions from Eq. 3.31 (red/ blue line) on the locations of λ_f and λ_b.

Alternately, we can investigate the range of actuation of the optical force by sweeping the *laser power* up and down at fixed wavelengths slightly red-detuned from the unperturbed cavity resonance. Theoretical predictions and experimental results are plotted in Fig. 3.13(a) and (b), respectively, showing the reflected power plotted against the incident laser power at nine red-detuned wavelengths: 1581.65 nm (black line), 1581.7 nm (grey line), 1581.75 nm (blue line), 1581.8 nm (cyan line), 1581.85 nm (green line), 1581.9 nm (magenta line), 1581.95 nm (violet line), 1582 nm (brown line), and 1582.05 nm (red line). The curves for the eight longer wavelengths are each vertically offset from the $\lambda_l = 1581.65$ nm curves for clarity. Again, we see good agreement between the calculated and experimental results: For small detunings ($\lambda_l = 1581.65$ to 1581.9 nm), the path traversed during an increase in input power from 0-2.25 mW (solid line) and a decrease in power (dashed line) coincide. At larger detunings, P_{out} experiences hysteresis. As the power is increased,

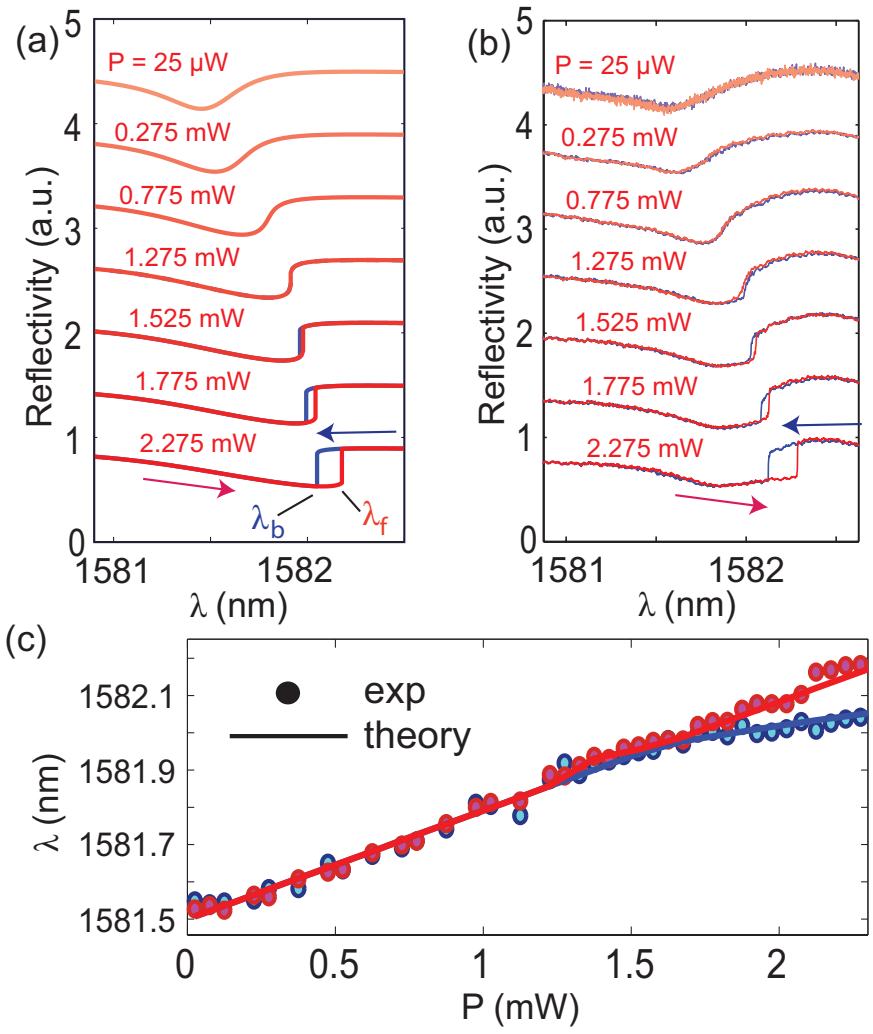

Figure 3.12: Calculated (a) and experimental (b) reflection spectra for forward (red lines) and backward (blue lines) swept lasers from P =0.275 mW to 2.275 mW at *low vacuum* ($\approx$ 10 mTorr). Hysteresis is predicted to onset around 1.525 mW. (c) Locations of bistable transitions during forward and backward wavelength sweeps. The transition wavelength during the forward sweep λ_f (red circles) is linear, and matches well to calculations from Eq. 3.31 (red line). The backward transition wavelength λ_b (blue circles) also show good agreement in the transition wavelength locations and the onset power for hysteresis.

the membrane enters the bistable region in the lower mechanical state and remains there until λ_b has redshifted such that $\lambda_b = \lambda_l$, at which point the membrane jumps to the lower curve, signifying an abrupt increase in the membrane separation. When

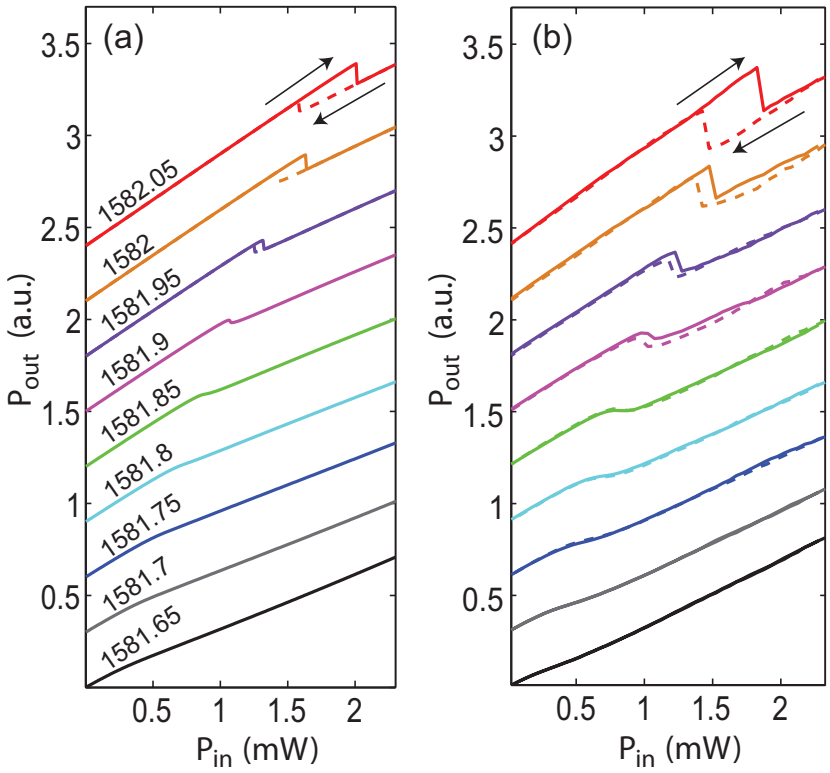

Figure 3.13: Predicted (a) and experimental (b) P_{in}-P_{out} curves of the device. Curves (with equal vertical offsets for easier visualization) are plotted for five red-detuned wavelengths: $\lambda = 1581.65$ nm (black line), 1581.7 nm (grey line), 1581.75 nm (blue line), 1581.8 nm (cyan line), 1581.85 nm (green line), 1581.9 nm (magenta line), 1581.95 nm (violet line), 1582 nm (brown line), and 1582.05 nm (red line). Solid lines represent the power output as a function of increasing laser power, while dashed lines represent power output as a function of decreasing input power. Modeling predicts hysteresis will occur at all wavelengths longer than 1581.95 nm.

decreasing the power, the membrane remains in the up-state until λ_f blue-shifts back to λ_l, forcing the membrane to jump to the upper curve which indicates an abrupt hop back to the pulled initial equilibrium position.

When we decompose the perturbation to the optical resonance into its constituent parts, we find optomechanically induced bistability to be the dominant effect. For

example, at $P_{in} = 2.275$ mW, optomechanical effects correspond to a peak resonance shift $\Delta\lambda_{OM} = 0.44$ nm, while thermo-optic contributions lead to $\Delta\lambda_{PT} = 0.23$ nm and photo-thermal-mechanical contributions lead to $\Delta\lambda_{PTM} = -0.01$ nm. This corresponds to a membrane which is mechanically pushed upward 2.3 nm by the optical gradient force and 0.1 nm downward by the photo-thermal-mechanical force, resulting in a net upward displacement of 2.2 nm. These results hold promise for large actuation range with repulsive optical forces by designing membranes which are less mechanically stiff and generate larger repulsive forces per mW of incident optical power by increasing Q_{opt}. For instance, Q_{opt} is currently limited by fabrication imperfections and the finite size effect of the PhC and could be boosted by simply increasing the number of unit cells in the membrane [114]. To maintain the same compactness of the structure which is related to its dynamic range, the optical design could be modified with a smaller lattice constant and/ or graded hole modulation [126].

In conclusion, we demonstrated actuation of a micron-scale membrane with a repulsive optical force using an extended guided resonance in a coupled silicon PhC membrane. The net red-shift displayed in the optical resonance of our doubly-bonded SOI platform is a result of an optomechanically induced red-shift, a thermo-optic red-shift, and a photo-thermo-mechanically induced blue-shift. Furthermore, simulations indicate that absorption in our system is dominated by surface defects and adsorbents, resulting in a linear absorption coefficient two orders of magnitude larger than that expected from bulk silicon. By minimizing these effects through fabrication process and design modifications, we can further isolate and exploit the unique optomechanical properties of this platform. Since multi-photon nonlinearities do not

occur until the excitation power exceeds ≈ 1 W with the use of a delocalized optical mode, the extent of pulling of the PhC membrane can be many tens of nanometers. Our silicon-based device provides a simple, non-intrusive solution to extending the actuation range of MEMS devices.

3.6 Summary

We demonstrated an optomechanical structure which features a tethered silicon photonic crystal membrane (30um×30um) suspended above a typical silicon-on-insulator (SOI) substrate. The large interaction area allows for strong expression of the Casimir effect that relaxes the signal-to-noise requirement in our detection. The square lattice of perforation serves as a polarization-insensitive second-order grating for coupling normally incident light, in contrast to the typical tapered fiber-coupled optomechanical structures. The large mode volume of the delocalized guided resonance drastically reduces the intracavity optical intensity and hence minimizes multi-photon events, including two-photon absorption, free carrier absorption, which plague typical silicon photonic devices as mentioned before. As for the optomechanical properties, we probe and actuate with a bandedge dark guided resonance (which corresponds to a repulsive force in the telecom range. For vertically coupled optomechanical devices, tunability of the optomechanical coupling strength is not well controlled or would otherwise require a new substrate with different sacrificial layer thickness. We achieved wide-range (from 120nm to 300nm) tuning of the optomechanical coupling strength on the same substrate by engineering the in-plane compressive stress of the silicon device layer and the stress-gradient-induced torque and hence

controlling the membrane-substrate separations. Measurements of the optical spring effect and the dynamic back-action in systems with respective g_{om}=-$2\pi\times5$ GHz/nm and g_{om}=-$2\pi\times66$ GHz/nm reveal interesting competition between the gradient force contribution F_{opt} and the photothermal force contribution F_{ptm}. In particular, the polarity of the mechanical linewidth change across the optical resonance is reverse of what would be expected with the conventional optical force; the amplitude of the effect is larger what could be achieved with our low-Q optical resonance albeit the large g_{om}. This suggests the presence of the photothermal force and we attribute the photothermal force to linear surface-state absorption of telecom light in silicon. The dynamic back-action mediated by photothermal coupling led to blue-detuned optomechanically cooling of the membrane to 1 Kelvin from room temperature or undergo red-detuned lasing-like self-oscillations with an amplitude greater than 10nm. Furthermore, we demonstrated nanometer-range pulling (1nm/1mW) and optomechanically induced optically bistability and hysteresis with the repulsive optical gradient force. In the calculation of the membrane's equilibrium position upon the exertion of the repulsive force, care was taken to account for the photothermal force and the thermo-optic effect due to the linear absorption. This allows one to infer the membrane's equilibrium position by inspecting the membrane's bistable transition wavelength. This allows one to infer the membranes equilibrium position by inspecting the membranes bistable transition wavelength. With the ingredients above combined, the prospect of real-time monitoring and controlling of MEMS/NEMS through this new optomechanical degree of freedom is promising.

Chapter 4

Approaches of measuring the Casimir effect and mechanical nonlinearity in optomechanical structures

Some of the earliest Casimir measurement is based on static detection of the counteracting force required to remain at a certain equilibrium position. Nowadays, due to more superb signal-to-noise performance, most of the current demonstrations of the Casimir force rely on the detection of the mechanical resonant frequency shift (or the force spatial gradient) due to the Casimir potential [127]. The principle works all forces whose strength is distance-dependent including the electrostatic force, magnetic force and optical force. The force gradient change is then plotted for each separation between the interacting objects to extract the power dependence. Unique to the

Casimir force, there are two signatures experimentalists seek to gain access to such quantum electrodynamical effect:

1. Casimir-induced mechanical frequency shift;

2. Casimir-induced mechanical nonlinearity at low oscillation amplitude.

We describe the measurements of these signatures and the corresponding challenges in our coupled silicon photonic crystal platform below.

4.1 Multiple-device measurement

Most experimental demonstrations of the Casimir effect involve controllably placing an external test body to another object with the help of modern high-precision (closed-loop), high-resolution (sub-nanometer) motorized stages [87, 88, 89, 90, 91, 92, 93, 94, 95, 127]. Careful calibration procedures of piezo-drivers which display hysteretical beahviors, and minimizing systematic errors due to thermal drifts in experimental apparatus during measurements, are required. With the Casimir effect probed in various material and geometrical systems, it is high time to progress to integrating Casimir oscillators to a realistic MEMS/NEMS platform. Not only can the transition to on-chip integration be beneficial to removing the need of sophisticated instrumentation for external alignment, but it also paves the way of harnessing the Casimir effect for ultra-compact sensing and studies of nonlinear dynamics. The ability to controllably displace a test body on-chip can be reaped from the fruitful progress made in electrostatic and, more recently, optomechanical actuators. Yet, while utilizing forces with nonlinear separation-dependence, a corresponding spring effect is often

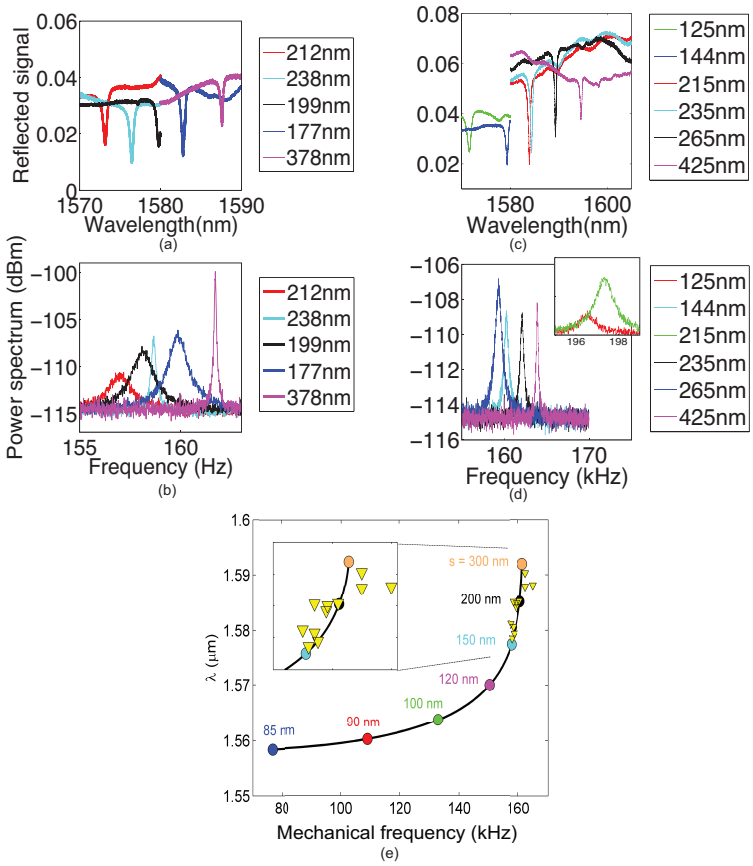

Figure 4.1: Feasibility of probing the Casimir effect by correlating the optical and mechanical resonances: (a) The optical spectra and (b) mechanical spectra of a group of coupled photonic crystal membranes, with hole periodicity of 920nm and diameter of 368nm and membrane-substrate separations of 177nm, 199nm, 212nm, 238nm and 378nm. The plots are vertically aligned with each other to allow for direct comparisons of the relative orders of the optical and mechanical resonances. (c) The optical spectra and (d) mechanical spectra of a group of coupled photonic crystal membranes, with membrane-substrate separations of 125nm, 144nm, 215nm, 235nm, 265nm and 425nm. The measured optical resonances may not consistently order with the membrane-substrate separations whose measurements could be prone to errors. However the generally consistent relative orders of mechanical and optical resonances may pave a new approach of uncovering the Casimir effect. Variabilities also exist in the mechanical response among the fabricated devices which lead to outlying data points, as shown in the inset of (d). (e) Mechanical and the corresponding optical resonances of 11 devices are overlayed on the calculated results that correlate the expected Casimir-shifted mechanical frequencies and the optomechanically sensitive optical resonances.

introduced, obscuring the measurement of the force gradient concerned [94]. One may circumvent such problem by designing the force landscape where the force gradient is zero at particular conditions. For instance, when an optomechanical resonator is pumped on resonance, there will only be a change in the equilibrium position without introducing the optical spring effect. Here we propose adopting a drastically different method of probing the Casimir effect without external actuation, namely fabricating numerous Casimir oscillators where the membrane-substrate separation is controlled by stress/torque-engineering. By achieving PhC membranes with a wide range of membrane-substrate separations, we could map out the Casimir-induced mechanical frequency shifts as a function of the membrane-substrate separations. Moreover, due to the strong optomechanical coupling, the optical resonances are indicative of the membrane-substrate separations. Hence, the trend of the mechanical frequencies against the measured optical resonances may reveal the Casimir-induced force gradients obtained at low probe powers.

In Chapter 3, we demonstrated the optomechanical properties and dynamics of the coupled photonic crystal membrane systems where the device layers are 185nm thick, and the starting sacrificial layer is 265nm thick. We also measured the optical resonances and mechanical frequencies of devices at low probe powers which have membrane-substrate separations (measured by the optical profilometer) ranging from 125nm to 425nm. Figure 4.1 shows 11 sets of data to illustrate the feasibility of uncovering the Casimir effect by correlating the relative positions of the mechanical and optical resonances. As a quick review, the photonic crystal membranes has a hole periodicity of 920nm and diameter of 368nm. They support an anti-bonding mode

whose resonant wavelength blue-shifts as the membranes come closer to the bottom substrate. Figure 4.1(a) and (b) show the optical spectra of the anti-bonding modes for five devices with different separations and the corresponding mechanical spectra. In the optical spectra, we observe that optical resonances of membranes of increasing separations do not consistently red-shift. In particular, the device with a separation of 177nm has a longer resonant wavelength than that of 238nm. Otherwise, devices with separations of 212nm, 238nm and 378nm do show the anti-bonding mode characteristic. However, when we compare the relative orders of the optical and mechanical resonances' locations, they are mostly identical. We performed a similar measurement for six other devices with various membrane separatoins. Their optical and mechanical spectra are plotted in Figure 4.1(c) and (d). There, the optical resonances do order that reflect the characteristic of an anti-bonding mode. When we consider the mechanical resonance's relative order, however, the agreement with the optical resonance's relative order is fair except for two outliers whose frequencies are close to 200kHz as opposed to ≈160kHz. With these observations, we evaluate the feasibility of probing the Casimir effect by measuring multiple devices of different separations. First, the consistency of the mechanical resonance orders and the corresponding optical resonance orders, and the lack of consistency of the optical resonance orders with respect to the optical profilometer measurements of the membrane separations may suggest that the profilometer readings could be prone to errors. Alternately, structural changes may have occurred in between profilometer measurements and device characterization in the vacuum chamber. Thus, under the shadow of these possible sources of errors that could affect the interpretation of the trends of the mechanical

resonances against the supposed membrane separations, the relatively satisfactory consistency of the orders of the mechanical and optical resonances may lead us to an alternate form of demonstrating the Casimir effect which uses the optical resonant wavelengths as the indicator of the membrane separations. While outliers do exist due to fabrication variabilities, we hope that measurements of a large number of devices may provide a qualitative signature of the Casimir effect. In Figure 4.1(e), we plot the calculated curve that correlates the expected Casimir-shifted mechanical frequency with the expected optical resonant wavelengths for devices of various membrane separations. We then overlay the mechanical resonant frequencies and the corresponding optical resonant wavelengths of 11 different devices on the calculated results. Preliminary agreement over a small range is observed. We further pursue this measurement approach with another double-SOI wafer system with a smaller initial gap to sample the range close to or even below 100nm of membrane separations.

The starting wafer system has a sacrificial oxide layer of 100nm. However, the yield of surviving devices after vapor hydrogen fluoride etch (VHFE) to release the PhC membranes was poor. Various experimentations of different support arm designs were conducted, and eventually the yield becomes satisfactory by improving on the VHFE protocol. Further details can be found in Appendix 1. Structural changes relevant to the following characterizations include fabricating membranes with shorter and hence stiffer support arms, slightly modifying the dimensions of the stress-relief structures and introducing etch holes to the arms for more homogeneous etch throughout the devices. Applying the stress-relief control techniques developed for the previous optomechanics experiments to the current photonic crystal mem-

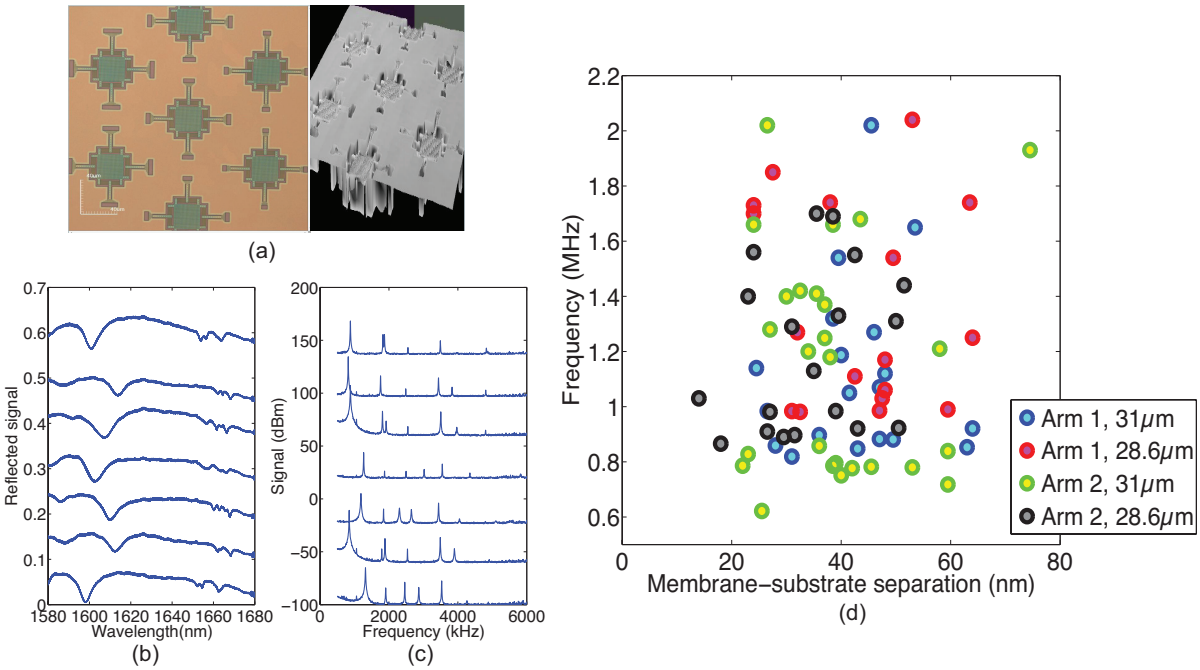

Figure 4.2: Large variations in mechanical resonant frequencies of small-gap PhC membranes: (a) Optical micrograph of an array of seven suspended PhC membranes and the corresponding 3D illustration of the height profiles measured by the profilometer. A series of seven (b) optical spectra and (c) mechanical spectra of devices with membrane separations smaller than 60nm are shown. (d) The mechanical resonant frequencies of the fundamental peaks are plotted against their measured membrane-substrate separations for four different mechanical designs. The variance in the fundamental mechanical frequency spans $\approx$ 1MHz.

branes, we achieved membrane-substrate separations ranging from 20nm to 140nm as measured by the laser profilometer (error bar +/- 10nm). The hole periodicity of the photonic crystal membrane is 840nm and the hole diameter is 334nm. Several samples, each with hundreds of devices, were fabricated and the devices' mechanical and optical responses were recorded. However, we notice that the approach aforementioned of correlating the mechanical and optical resonances to reveal the Casimir effect in this new substrate was not successful. The mechanical resonance frequencies were several factors off from the simulation results. Also there is huge variation in

the mechanical resonant frequencies among devices of similar dimensions. Here we provide a brief summary of the observed results in two different samples. Figure 4.2(a) shows the optical micrograph of an array of seven released photonic crystal membranes and a 3D reconstruction of the height profile of the membranes measured by the laser confocal profilometer. The membranes are properly released with no apparent oxide left underneath. Figure 4.2(b) shows a series of optical spectra of the same design but with membrane separations of 38.5nm, 43m, 40nm, 63nm, 47nm, 31nm, and 49.5nm (from bottom to top). A broad resonance is identified in the 1600-1620nm range, and two more weakly coupled ones in the 1650-1670nm range. The low-Q nature of the stronger resonance causes difficulty in using the mode as a convincing membrane-separation indicator. The corresponding mechanical spectra are shown in Figure 4.2(c). The mechanical frequencies of the fundamental peak vary between 819kHz and 1.32MHz, which is several factors off the simulated value around 160kHz. Also the large variance of the measured frequencies among a group of similar devices is abnormal. Conclusive correlations cannot be made among the mechanical resonances, optical resonances and the membrane separations. This is further verified by plotting the mechanical frequencies of 4 slightly different mechanical designs against the membrane-substrate separations, shown in Figure 4.2(d).

A similar phenomenon is observed with another sample but here the support arms are slightly shorter. Figure 4.3(a) and (b) shows the broadband optical and mechanical spectra of a device. Again three pronounced optical resonances are observed. We attempt to correlate the resonance locations with profilometer readings of the membrane-substrate separations in Figure 4.3(c-e) for four different mechanical de-

signs but no obvious trends can be observed. This may mean the optomechanical coupling strength is too small to guard against fabrication variability among devices. Figure 4.3(f) plots the fundamental mechanical frequencies over membrane separations. Interestingly the mechanical resonant frequencies is around 500kHz. Similar to the previous demonstrations, there is large variance in the mechanical resonant frequencies from device to device.

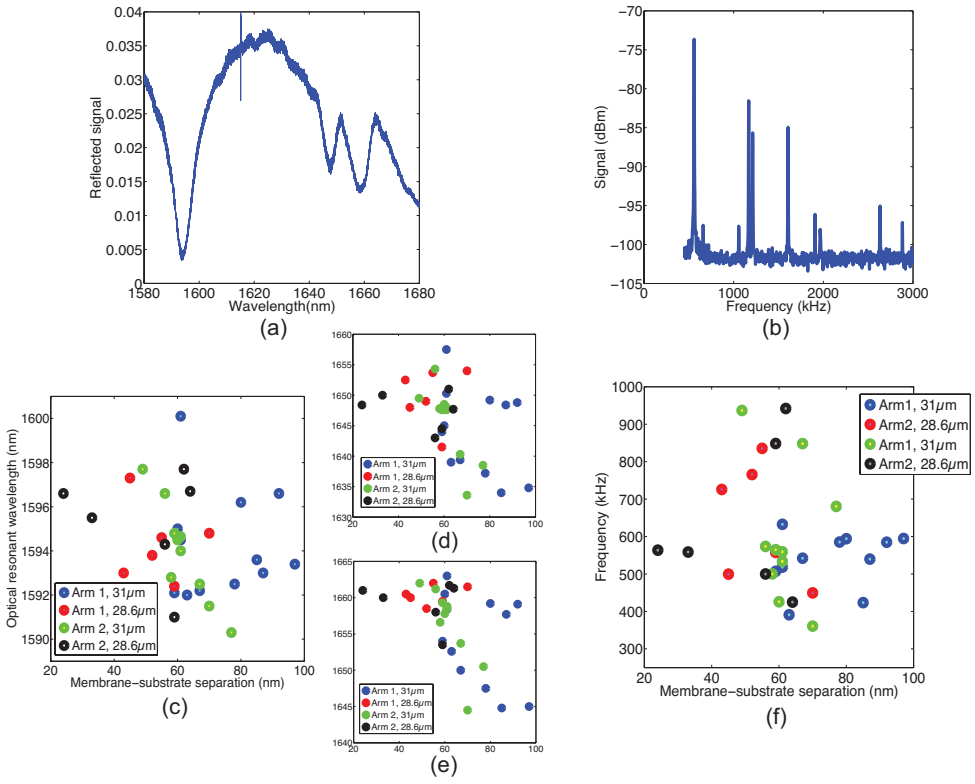

Figure 4.3: Another demonstration of large variance of mechanical resonant frequencies: (a) Broadband optical and (b) mechanical spectra of a typical suspended PhC membrane. The main optical resonance is in the range of 1590 to 1600nm, whereas the remaining two are in 1630-1660nm and 1645-1665nm. Their resonant wavelengths are plotted against the membrane-substrate separations reported by the optical profilometer. (f) Frequencies of the fundamental mechanical mode for four slightly different mechanical designs are plotted against the membrane separations. Similar to Figure 4.2(d), no conclusive trends can be observed.

The estimated Casimir-induced shift in the mechanical frequency is in the range of tens of kHz for membrane-substrate separations in the sub-100nm range. However the large variance of the mechanical frequencies forbids us to establish convincing results of the Casimir effect despite the positive outlook from the old substrate and the availability of small-gap devices in the current substrate. It is hypothesized that the device layer contains a significant stress gradient across the cross section, causing in-plane curling of the support arms. A curled support arm is much stiffer than an uncurled one, causing such large mechanical resonant frequencies. The variability may be due to the uncontrolled amount of curling acting on the support arms. Careful measurement of the stress gradient in the device layer is called for. Also support arms that are composed of multiple narrow beams in parallel may help to reduce the curling effect. Hence this arm design is adopted for the experiments discussed in Section 4.2.2. It is also hypothesized that some optically inaccessible oxide residues are left on the underside of the device layers. Using PDMS to peel off the suspended membranes to reveal the underside, which is a demonstrated MEMS troubleshooting technique, may help us verify this speculation.

4.2 Casimir-induced and optical force-induced mechanical nonlinearity

The Casimir force landscape is highly nonlinear as the interacting bodies approach each other in the separation range of hundreds of nanometers. The idea is to sample the Casimir anharmonicity by coherently driving the flexural motion of the photonic

crystal membrane whose oscillatory amplitude can reach the nanometer range. Readily read off from the equation of motion in the frequency domain, the response of the membrane to the force at the mechanical resonant frequency Ω_m is amplified by the mechanical quality factor $Q_m = \Omega_m/\Gamma$. Here we adopt two coherent driving mechanisms, namely piezo-stack drive and optical-gradient-force drive, to harness the Casimir nonlinearity.

4.2.1 Coherent drive by harmonic piezo-actuation

The piezo-stack actuator employed is the PL022.30 chip actuator whose dimensions are 2mm × 2mm × 2mm. The sample is mounted to the actuator with Electrodag 502. [1] While the option of mounting the sample with the bottom in contact with air (for reasons explained in Chapter 2) is not available, Electrodag 502 effectively absorbs telecom light as graphite is a good light absorber. This is verified by the absence of large-amplitude, fast optical fringes due to the back reflections in the optical spectra. The sinusoidal driving signal is provided by a function generator (HP 33120A) whose amplitude is $10V_{pp}$. Electrical connections for driving signal transmission are made through spare electrical ports in the vacuum chamber. Setting of the input drive from the function generator is accordingly incorporated in the LabVIEW automation.

While PL022.30 is successfully incorporated in laser systems requiring fast response in laser cavity stabilization [128], we observe that the chip actuator does

[1] Electrodag 502 is a graphite-based quick-drying adhesive and can be easily dissolved in acetone.

not have a flat mechanical response in the frequency window concerned [2], rendering studies of driving-power dependent mechanical bistability and hysteresis difficult [3]. Instead of studying the dynamics over a full range of excitation frequencies, the rich nonlinear dynamics of the PhC membranes at single excitation frequencies with increasing large drive amplitude is presented in this section.

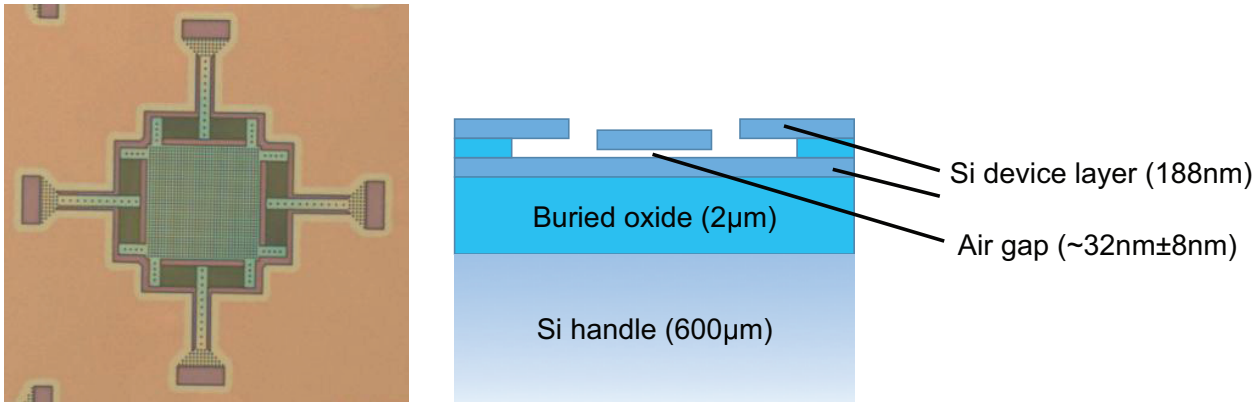

Figure 4.4: An optical micrograph of the kind of photonic crystal membrane under study. Note that the arms have added etch holes along the lengths to ensure more uniform etch throughout the structure. Accordion-like stress-relief structures are employed. The membrane thickness is close to 200nm where the membrane-substrate separation is ≈32nm. Hole periodicity = 840nm; hole diameter = 340nm.

Figure 4.4 shows the optical micrograph of a photonic crystal membrane with the identical design (except the etch hole arrangements at the anchors) and the relevant dimensions. The hole periodicity is 840nm and the diameter is 340nm. Starting with

[2]PL022.30 is specifically designed for fast response for static extension instead of AC driving. As a result of the square profile of the actuator and the composition of multiple piezoelectric layers, in-plane and out-of-plane interferences of the acoustic waves occur [129]. Hence we observe multiple resonant features directly from the chip actutator in the spectral domain. Also it is observed that signal leakage (presence of signals from the function generator despite the absence of probing light) is significant in some frequency windows above 620kHz.

[3]While proper adjustment in the driving signal is possible to obtain a flat response, the piezo's resonant response at 1.24MHz is at least 10 times larger than other nearby driving frequencies. Hence the dynamic range of the drive may be limited.

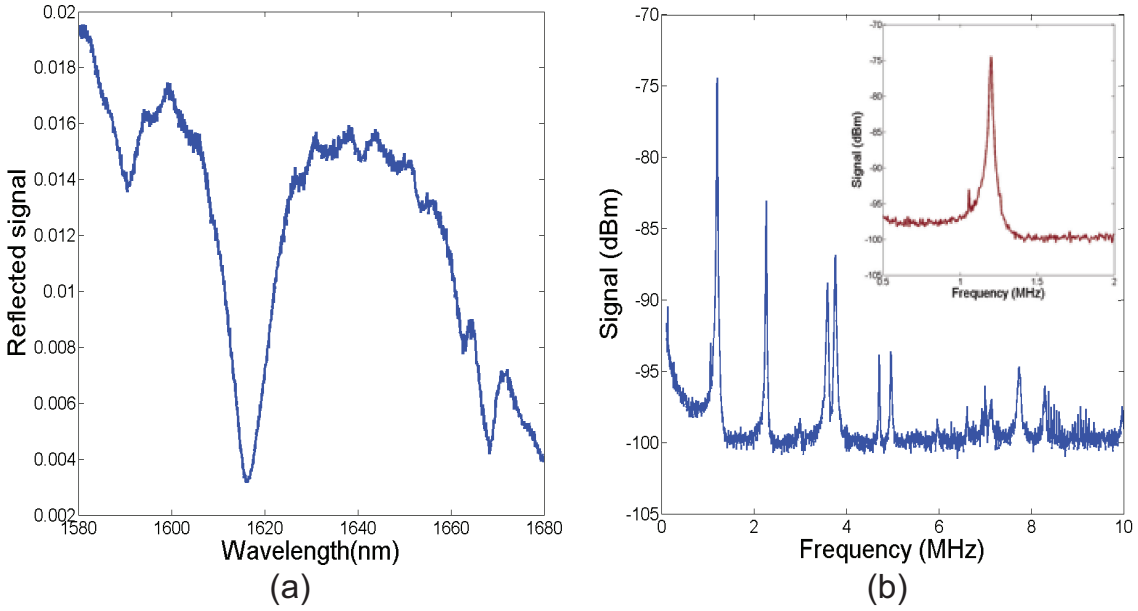

Figure 4.5: (a) Optical spectrum of the photonic crystal membrane. The most prominent resonance is centered at λ =1617nm with an optical quality factor of ≈200. Two other neighboring, less coupled resonances are centered at 1590nm and 1667nm. (b) Mechanical spectrum of the PhC from 0.5MHz to 10MHz, taken with the probe light parked at the shoulder of the optical resonance. Inset shows the fundamental peak of the membrane (resonant at 1.2MHz) which corresponds to the flexural mode. The small sharp peak at 1.05MHz is from the laser.

100nm of sacrificial oxide layer, the membrane-substrate separation of the device under study is 32nmpm8nm as measured by the optical profilometer; the gap is small enough for the pronounced expression of the Casimir effect. Figure 4.5(a) shows the optical resonances of the PhC in the U-band wavelength range. The most prominent resonance is centered at λ =1617nm with an optical quality factor of ≈200. Figure 4.5(b) shows the mechanical spectrum of the PhC up to 10MHz where the inset shows the fundamental peak centered at 1.2MHz.

Given the small membrane-substrate separation of 32nm, the optomechanical coupling strength can be expected to be large. Though optomechanical dispersion by a

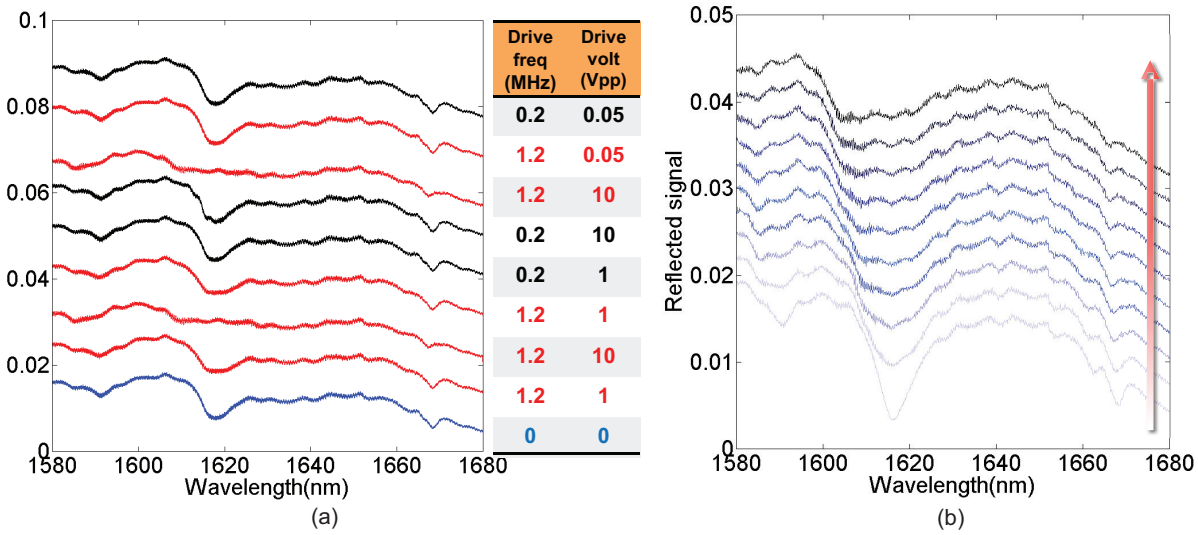

Figure 4.6: (a) Optical spectra of the photonic crystal membrane subjected to different piezo excitation frequencies and drive amplitudes. The drive parameters of each spectrum are tabulated and juxtaposed to the corresponding spectrum. Blue denotes no drive; red denotes resonant drive; and black denotes off-resonance drive. The optical resonance at 1617nm shows significant broadening upon large-amplitude resonant drive where off-resonant drive has no effect to the resonance. The broadening occurs likely due to time-averaging of the optomechanical dispersion. (b) Optical spectra with the membrane driven at 1.24MHz with increasing drive amplitude from $1V_{pp}$ to $10V_{pp}$ (increment of $1V_{pp}$ from spectrum to spectrum). Curves are offset to facilitate direct comparison. The extent of resonance broadening increases as the resonant drive amplitude increases.

CW optical pump was not observed due to the low-Q of the optical mode and insufficient laser power, when coherently driven close to the mechanical resonance, the optomechanical dispersion becomes conspicuous. Figure 4.6(a) shows a sequence of optical spectra (offset for clear illustration) taken at various driving parameters. The bottommost spectrum is the reference taken without any drive. Then the driving signal at 1.2MHz (resonant frequency of the PhC) is turned on, first with a medium drive amplitude $1V_{pp}$, proceeded with $10V_{pp}$ and back to $1V_{pp}$. The optical spectra (red, bottom) are recorded respectively. At $1V_{pp}$, the optical resonance around

1618nm broadens slightly relative to the reference spectrum. At $10V_{pp}$, the resonance broadens significantly while the neighboring resonances around 1590nm and 1667nm appear to blue-shift. As the drive strength returns to $1V_{pp}$, we recover the previous optical spectrum with good consistency. The result of such sequence suggests that the large amplitude of mechanical oscillations does affect the membrane optically, which is seldom observed in typical optomechanics experiments. It is postulated that the large oscillation amplitude x_0 causes large optomechanical dispersion of the resonance at 1618nm. For each wavelength around the resonance, the probe light goes in and out of resonance over the oscillation period. As the optical spectra are taken quasi-statically (assuming the dwell time of each laser probe wavelength is much longer than the oscillation period), the time-varying optical reflected signal is time-averaged, and hence a much shallower resonance response is observed. Numerically integrating (4.1), the instantaneous reflectance of a resonantly driven PhC membrane, over the typical laser dwell time ΔT (e.g. 1ms), we also observe a broadened optical resonance $|a_{out}^{-}|^2$ that qualitatively conforms with the data. We also observe from the computed time series that the optical output gradually deviates from the sinusoidal shape and eventually evolves into signals with other harmonic components.

$$|a_{out}^{-}|^2 = \int_t^{t+\Delta T} \frac{dt}{\Delta T} \frac{\kappa_e P_{in}}{(\kappa/2)^2 + (\omega - \omega_0 - g_{om} x_0 cos(\Omega t))^2} \tag{4.1}$$

where κ_e is the external coupling linewidth, κ the total linewidth of the resonance, g_{om} the optomechanical coupling strength, Ω_{drv} the angular mechanical driving frequency. We roughly estimate the oscillation amplitude to be 1-2nm assuming a g_{om}

of 230GHz/nm. In Figure 4.6(b) the PhC membrane is driven at 1.24MHz [4] with increasing drive amplitude from $1V_{pp}$ to $10V_{pp}$ where each spectrum represents an increment of $1V_{pp}$. The degree of resonance broadening is progressively enhanced as the drive amplitude grows. We further confirm the broadening effect's dependence on the drive frequency by choosing an off-resonance frequency, and record the optical spectra (shown in Figure 4.6(a)) for both medium $1V_{pp}$ and high drive amplitudes $10V_{pp}$, which are identical to what we obtained for the reference

Having established that the resonant drive could generate sufficiently large amplitude of membrane oscillations, we proceed to seek signatures of nonlinear mechanical response at single frequency excitations. In the following demonstration, we illuminate the membrane with light at 1614nm (blue-detuned from resonance) at 3mW and piezo-drive the membrane with different drive parameters. The PhC membrane is driven at f_{dr} =1.24MHz (40kHz detuned from mechanical resonance) where the drive amplitude increases from 50mV_{pp} to $9.85V_{pp}$ with an increment of $0.25V_{pp}$ from scan to scan. From the mechanical response, we observe (i) harmonics of drive signal, (ii) sum and difference frequency generation, and (iii) non-trivial interactions of the Brownian peak and the drive signal.

First, in Figure 4.7, the PhC membrane is driven at $0.85V_{pp}$ and $6.65V_{pp}$ respectively. A train of harmonics (multiples of driving frequency f_{drv}=1.24MHz) appear in the measurement bandwidth of 10MHz. At a low drive amplitude, the spectrum (blue) does not significantly deviate from the weakest drive spectrum (cyan) and the main drive peak has the strongest response. At a higher drive amplitude, the

[4]The piezo actuator has its own resonance response at 1.16MHz and 1.24MHz, which allows for a greater degree of coherent drive.

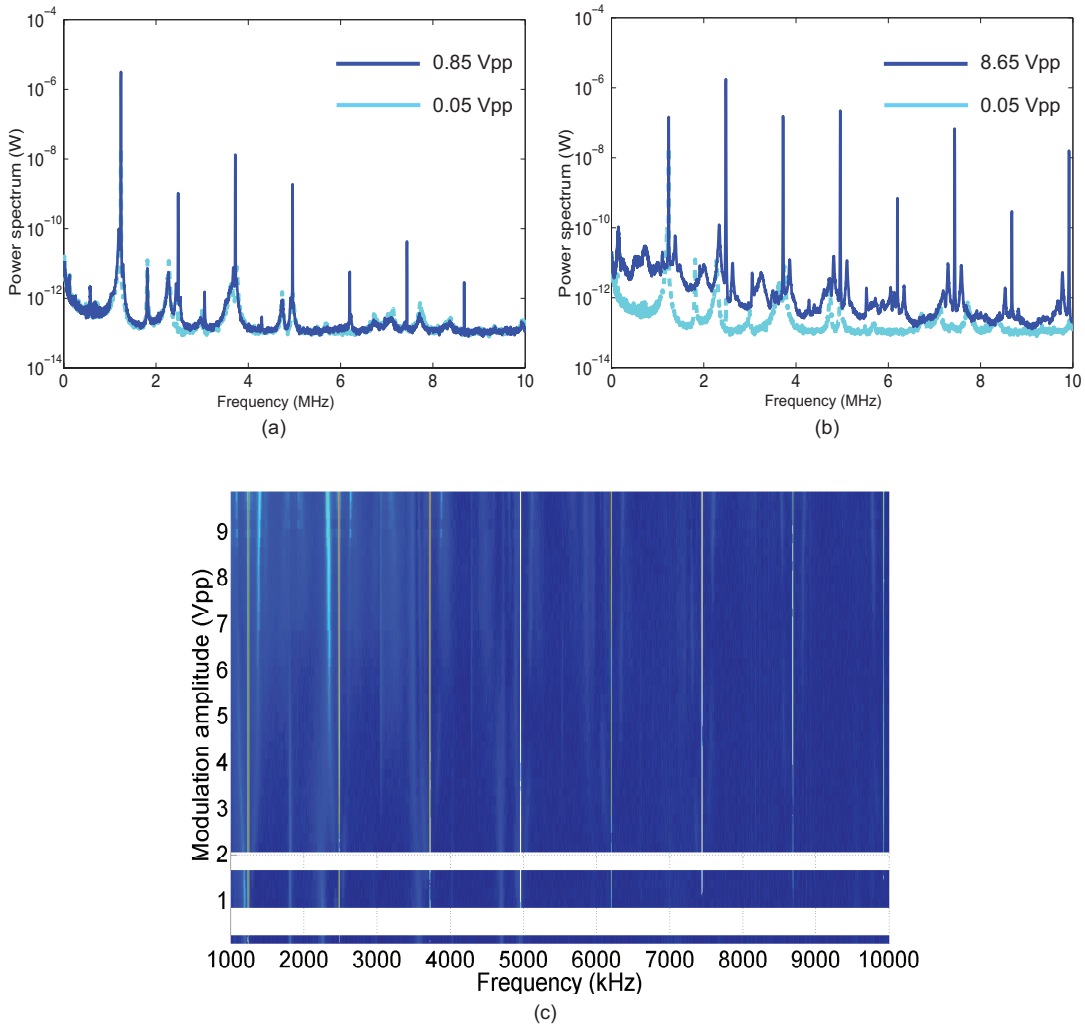

Figure 4.7: Emergence of harmonics in the transduced signals: (a) Mechanical spectrum of the PhC membrane driven at 1.24MHz with $0.85V_{pp}$ (blue) and $0.05V_{pp}$ (cyan) respectively. Emergence of harmonics of 1.24MHz due to nonlinear optical transduction. b) Mechanical spectrum of the PhC membrane driven at 1.24MHz with $8.65V_{pp}$ (blue) and $0.05V_{pp}$ (cyan) respectively. New spectral features generated in the vicinity of the drive signal also displayed at the higher harmonics. (c) Compilation of mechanical spectra of the membrane driven with increasing drive strength from $50\text{m}V_{pp}$ to $9.85V_{pp}$ (increment of $0.2V_{pp}$). Higher harmonics become more apparent upon stronger drive. White stripes represent missing data for certain drive strengths. Colorbar scale is in log scale (units of Watt).

spectrum are very different from the low drive case, showing rich, nontrivial interactions in this strongly driven system. The first few harmonics share similar response

strength with the fundamental drive signal, with new spectral features generated in the vicinity, and"copied" around the harmonics. It is particularly interesting that the first harmonic is slightly stronger than the fundamental drive peak. The origin of the harmonics with a low drive is due to nonlinear optical transduction. As discussed in the optical resonance broadening experiment in Figure 4.6, higher harmonics are expected as the probe light samples through the Lorentzian optical lineshape upon large optomechanical dispersion. However, in the high-drive case, it is possible that harmonics are generated as a result of mechanical nonlinearity. For instance, odd harmonics can be generated in the presence of cubic Duffing mechanical nonlinearity $O(x^3)$. Thus, to properly differentiate between optical transduction nonlinearity and *bona fide* mechanical nonlinearity, we need to resort to probing the mechanical response with another optical mode with sufficient, yet low optomechanical coupling strength. While a proper pump-probe experiment with a suitable wavelength-division multiplexer (WDM) is not available at the moment, this is pursued in section 4.2.2.

Second, in Figure 4.8(a), we show the spectral shape (red) around the fundamental mode as the membrane is driven at 1.24MHz, $1.05V_{pp}$. Compared to the reference spectrum (fluorescent green) taken at the weakest drive, the Brownian peak originally at 1.2MHz now shifts to 1.191MHz. Moreover a similar mirror image of the Brownian peak emerges on the other side of the drive peak at 1.289MHz (i.e. 49kHz away). At higher drive at $9.45V_{pp}$, we see in Figure 4.8(b) that not only do the closest sidebands move further away from the drive peak by $\approx$ 140kHz, but also a new pair of sidebands emerges as well. Currently we are not certain of the origin of these phenomena - that the Brownian peak appears to move away and pairs of sidebands symmetric to the

central drive peak emerge, but the spectral features are reminiscent of reports of injection locking of oscillators where a weak oscillator has non-trivial interactions with a nearby strong drive signal. Their relative phases eventually are locked to each other in time and sidebands are formed as well [130, 131].

Third, in Figure 4.9(a), we show the mechanical spectrum (blue) of the PhC membrane driven at $1.05V_{pp}$ in a frequency window up to 5MHz. Compared to the reference spectrum (fluorescent green), we notice new spectral components generated at 572kHz, 3.052MHz and 4.292MHz. They are sum and different frequencies due to the mixing of the strong coherent drive f_{drv}=1.24MHz and the second mechanical mode f_1=1.812MHz, and specifically 572kHz = $f_1 - f_{drv}$, 3.052MHz = $f_1 + f_{drv}$ and 4.292MHz = $f_1 + 2f_{drv}$. The mixing of the first two new spectral peaks is mediated by a quadratic nonlinearity whereas the mixing of the third peak is mediated by a cubic nonlinearity. In fact the sidebands emerging around the drive peak are also mixed and "down-converted" to a peak in the low kHz range. At a drive voltage of $5.45V_{pp}$, a relatively large peak is observed at 136kHz, which is the difference frequency of f_{side}=1.376MHz and the drive f_{drv}=1.24MHz. With this, we speculate that the upper sideband that mirrors the Brownian peak relative to the drive signal might be due to nonlinear mixing of the Brownian peak and the drive signal mediated by a cubic nonlinearity, namely $2f_{drv} - f_0$.

Finally, we characterize the mechanical response of the difference frequency signal due to $f_{drv} - f_{side}$ with increasing drive amplitude from $50mV_{pp}$ to $9.85V_{pp}$ (increment of $0.2V_{pp}$). Here we point out that the mechanical spectrum data below 1MHz are separately measured as opposed to the large-frequency-window measurements to

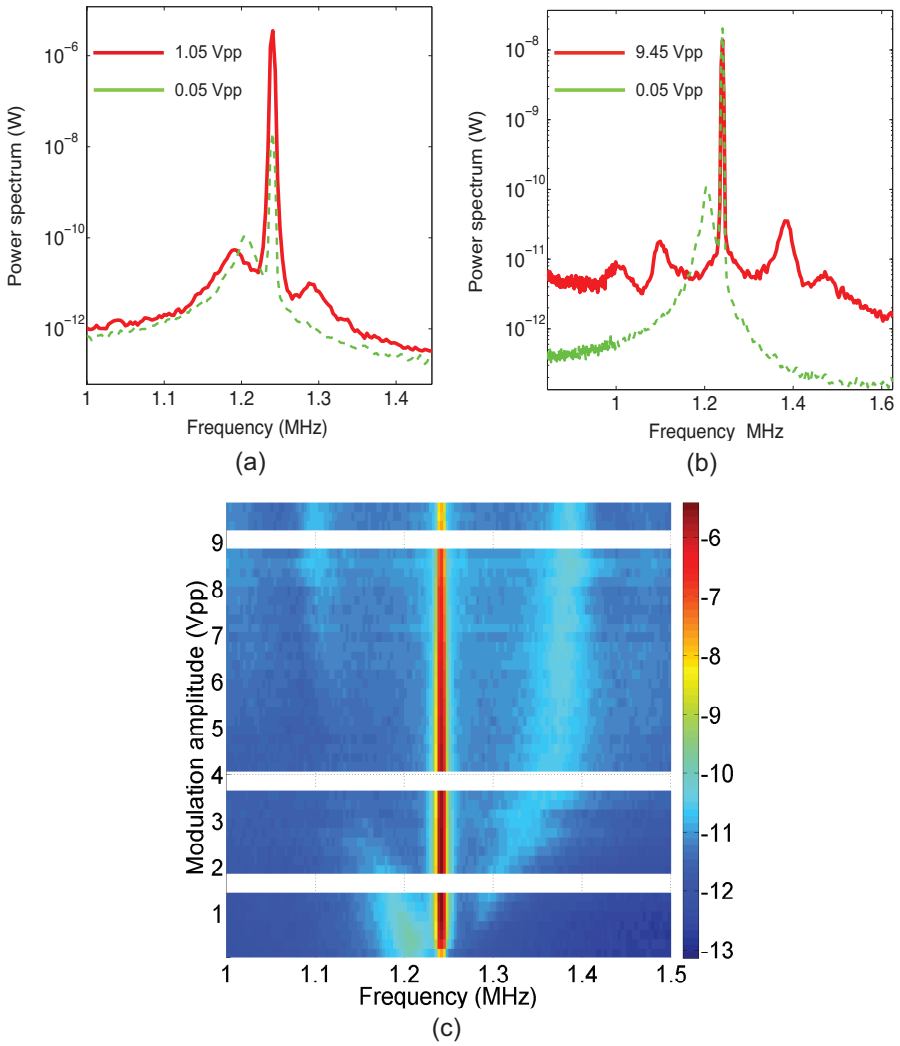

Figure 4.8: Emergence of sidebands around the drive peak: (a) Mechanical spectrum of the PhC membrane driven at 1.24MHz with $1.05V_{pp}$ (blue) and $0.05V_{pp}$ (cyan) respectively. The Brownian peak shifts by 49kHz from 1.2MHz. A sideband mirroring the Brownian peak is formed at 1.289MHz. b) Mechanical spectrum of the PhC membrane driven at 1.24MHz with $9.45V_{pp}$ (blue) and $0.05V_{pp}$ (cyan) respectively. The Brownian peak moves further out to 1.1MHz and the corresponding sideband moves accordingly. Another new pair of sidebands is formed upon stronger drive. White stripes represent missing data for certain drive strengths. Colorbar scale is in log scale (units of Watt).

obtain much higher frequency resolution for recording subtle frequency shifts and linewidth variations. Also in the low frequency window, the system is susceptible to

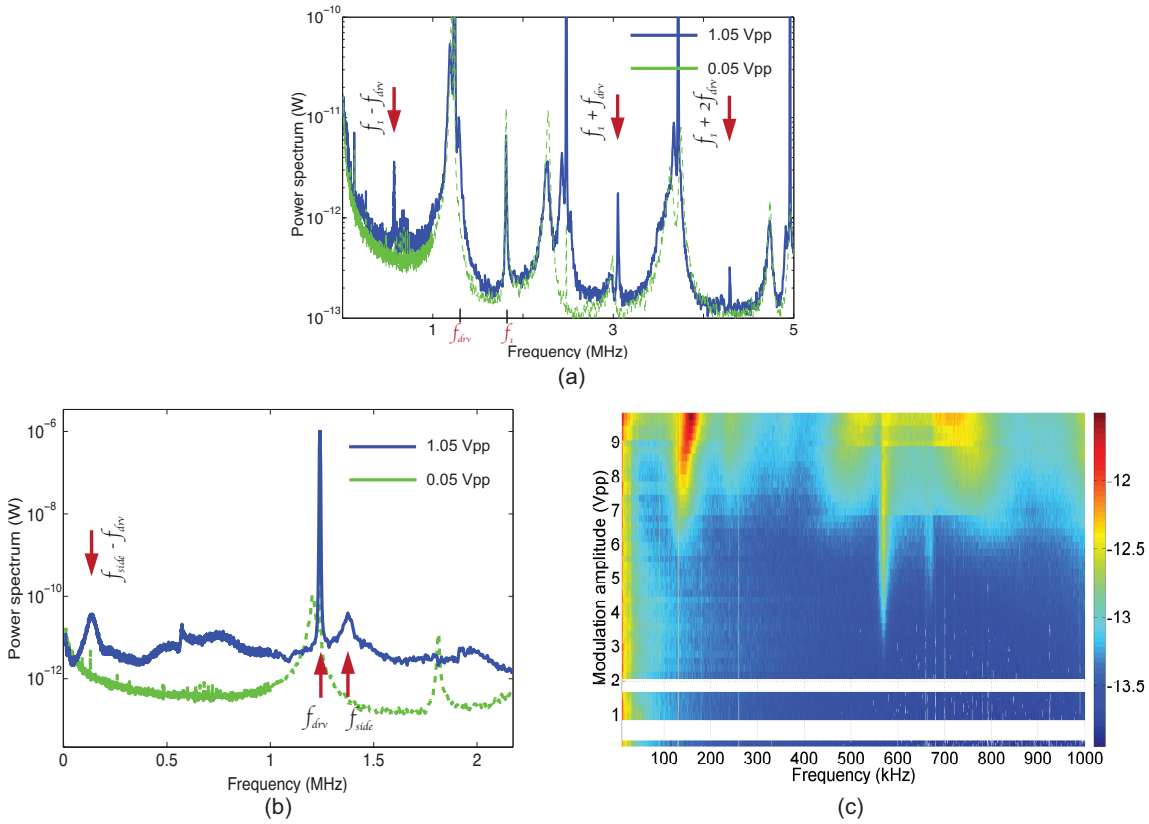

Figure 4.9: Nonlinear mixing of strong drive signal with mechanical modes: (a) Mechanical spectrum of the PhC membrane driven at f_{drv} 1.24MHz with $1.05V_{pp}$ (blue) and $0.05V_{pp}$ (green) respectively. Besides the pronounced harmonics mentioned in Figure 4.7, new spectral peaks are formed at 572kHz $= f_1 - f_{drv}$, 3.052MHz $= f_1 + f_{drv}$ and 4.292MHz $= f_1 + 2f_{drv}$, where f_1 is the second mechanical mode of the membrane at 1.812MHz. The mixing is mediated by quadratic and cubic mechanical nonlinearity. b) Mechanical spectrum of the PhC membrane driven with $5.45V_{pp}$ featuring the subharmonic range. The quadratic mixing of the sideband and the drive peak leads to a difference frequency peak at 136kHz. (c) Mechanical spectra (normalized to that taken with the lowest drive)in the subharmonic range with increasing drive strength from $50\text{m}V_{pp}$ to $9.85V_{pp}$ (increment of $0.2V_{pp}$). Rich spectral features emerge due to nonlinear mixing. White stripes represent missing data for certain drive strengths. Colorbar scale is in log scale (units of Watt).

large laser intensity noise and other electronic noise sources. Thus, while spectral information buried under the noise floor cannot be retrieved, we normalize each mechanical spectrum with that taken at the weakest drive strength to reveal the new

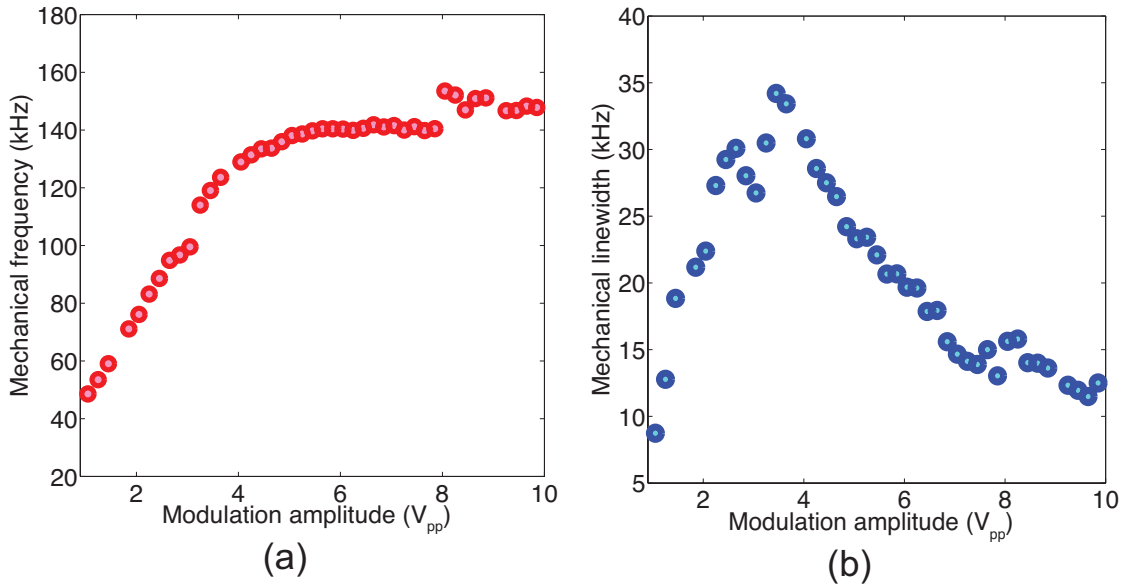

Figure 4.10: Mechanical response variation of the "down-converted" signal: (a) Extracted mechanical frequency of the difference frequency signal due to mixing of the drive peak and the shifted Brownian peak at various drive amplitudes. The subharmonic signal is fitted to a Lorentzian lineshape. (b) Corresponding extracted mechanical linewidth of the difference frequency signal.

spectral features. The difference signals are fitted to a Lorentzian lineshape. The fitted mechanical frequencies and linewidths at various drive amplitudes are plotted in Figure 4.10(a) and Figure 4.10(b). The mechanical frequency of the difference signal increases as the drive becomes stronger but eventually plateau to $\approx$ 140kHz, whereas the mechanical linewidth first increases from $\approx$ 10kHz to 35kHz and slowly reduces to the initial value upon stronger drive. Since the difference signal reflects changes in the Brownian peak, we note that the frequency shifts of the Brownian peak from the drive signal do increase and eventually saturate as shown in Figure 4.8(c).

4.2.2 Coherent drive by modulating the optical gradient force

Another approach of resonantly driving the PhC membrane without considering the spectral output homogeneity of a piezo actuator is by exerting a time-varying optical force. Similar to the piezo scheme, the oscillation amplitude of the membrane is enhanced by the mechanical factor Q_m. Given the sufficiently efficient optomechanical transduction, here we could carry out studies in the mechanical bistability and hysteresis as we are free from the complications of the piezo's own resonant response.

Moreover, due to the unique existence of back-action in the optomechanical interactions, both the static/DC component and dynamic/AC component of the optical force can be modulated to perform not only amplitude modulation but also parametric drive. Specifically, in Chapter 3, we illustrate that the optical force, which is intrinsically nonlinear in the separation of the coupled elements x, can lead to significant change to the mechanical resonant frequency and the mechanical linewidth to the first order. The extent of the frequency and linewidth tuning is dependent on the excitation power and the optical detuning. Thus, by sending in a harmonic optical excitation, the optical spring constant and the mechanical linewidth could be modulated in time accordingly. For instance, we achieve parametric oscillation at the frequency f_0 by modulating the optical spring constant at $2f_0$ where f_0 is chosen within the bandwidth of the fundamental mechanical mode.

The photonic crystal membrane for the optical-drive experiment is supported by a different stress-relief arm design where the arms are formed by a collection of thin, curly strings which are more susceptible to the deformation as the in-plane compressive stress is released. This change in the mechanical design is adopted in view of the

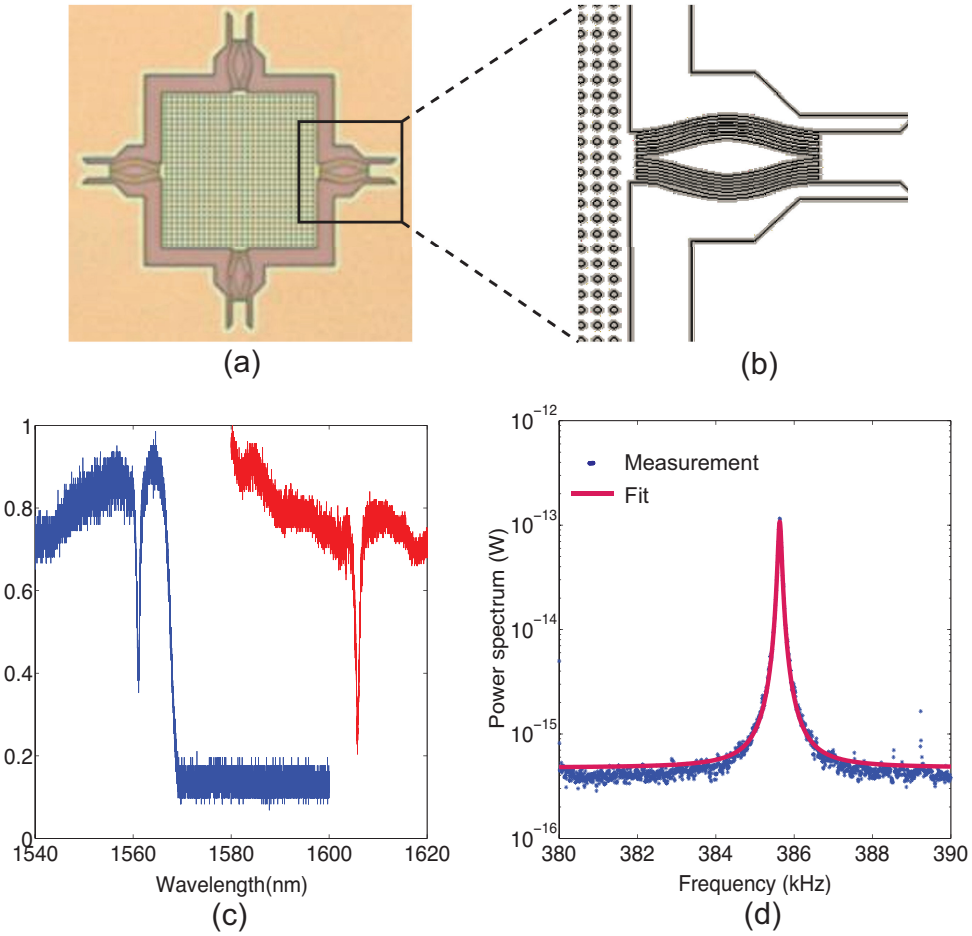

Figure 4.11: (a) An optical micrograph of the photonic crystal membrane supported by arms of a new stress-relief design shown in the magnified illustration in (b). The arms are composed of multiple curved narrow beams which are more compliant and permit preferential release of in-plane compressive stress. The hole periodicity is 1μm and the diameter is 400nm. (c) Optical resonances of the PhC membrane in the telecom range, centered at 1561nm and 1606nm. The presence of two traces (blue and red) is a result of separating the reflected light by a wavelength-division multiplexer. (d) Fundamental mechanical mode of the membrane (resonant frequency = 384.8kHz) fitted to a Lorentzian lineshape (red).

drastic deviation of the quantitative values of the mechanical modes from simulations using the previous mechanical design. Empirically, the current mechanical design does provide a softer mechanical spring for stronger manifestation of other external

force gradients. Figure 4.11(a) shows the optical micrograph of a photonic crystal membrane with the new stress-relief design (illustrated in Figure 4.11(b)). The hole periodicity is $1\mu m$ and the diameter is 400nm. Starting with 100nm of sacrificial oxide layer, the membrane-substrate separation of the device under study is 104nmpm8nm as measured by the optical profilometer. Previous designs engineer the arrangement of the etch holes at the end of the anchors to alter the effect of stress-gradient-induced torque from the sacrificial oxide underneath. Here in order to preserve a large number of working devices, we terminated the release process of PhC membrane at the curly arms. Hence the large degree of controlled gap-substrate tuning is not present on this particular sample. Figure 4.11(c) shows the two optical resonances of the PhC in the C/L-band and U-band wavelength range. They are centered at 1561nm and 1606nm whose quality factors are $\approx$ 2000. The optomechanical coupling for both modes is strong, as evidenced by the occurrence optical spring effect and dynamic back-action, readily observed at low optical powers. Figure 4.11(d) shows the PhC's fundamental peak centered at 384.8kHz and the quality factor is $\approx$6000.

To characterize the optomechanical effects in this current system, we pump the PhC membrane at various optical detunings across the optical resonance with a specified excitation power and measure the resultant mechanical response of the PhC membrane, as performed in the experiments delineated in Chapter 3. Figure 4.12(c,d) and (e,f) show the respective mechanical frequency and linewidth of the membrane (extracted from a Lorentzian fit), pumped and probed across the optical resonances centered at 1561.25 nm (Figure 4.12(a)) and 1606.32nm (Figure 4.12(b)) at $5\mu W$. First, we note that in both Figure 4.12(e,f) the mechanical linewidth increases non-

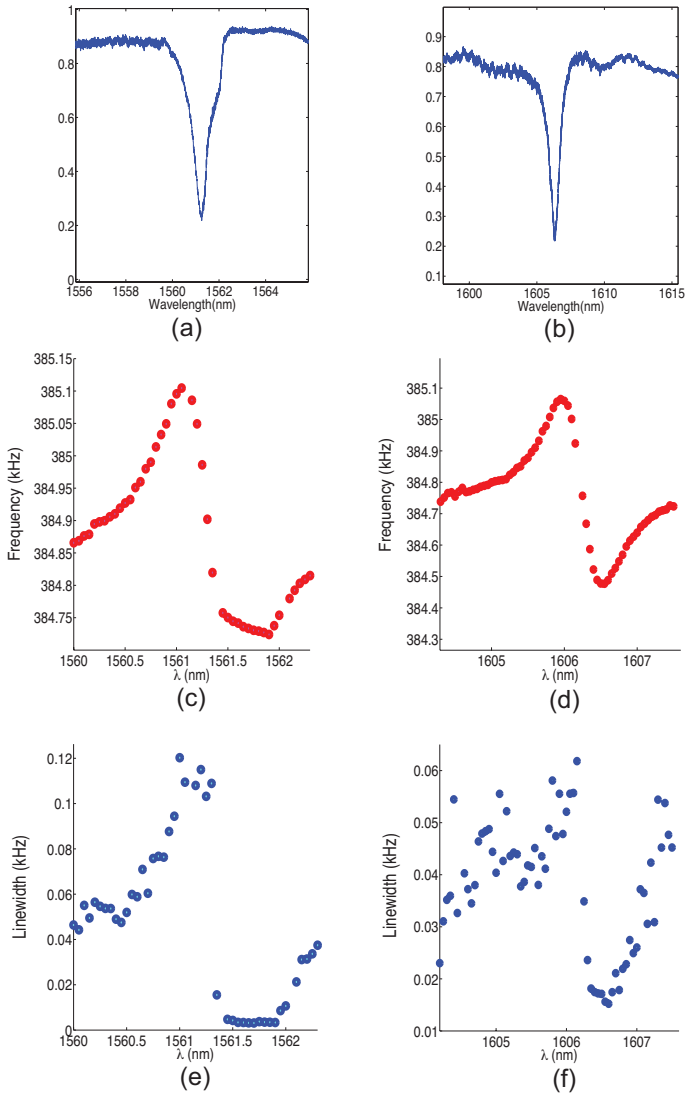

Figure 4.12: Characterization of the optical spring effect and dynamic backaction on the two optomechanically sensitive optical resonances: (a) and (b) show the guided resonances supported by the coupled PhC membranes in the C/L band and in the U band, centered at 1561.25nm and 1606.32nm respectively. (c, d) and (e, f) show the fitted mechanical frequencies and linewidths of the fundamental mechanical mode when pumped with 5μW across the optical resonances. As shown in (e), self-oscillations occur readily at this relatively low excitation powers on the red-detuned side of the optical resonance.

monotonically on the blue-detuned side of the optical resonance and decreases on the red-detuned side. We established in Chapter 3 that such trend of the dynamic

backaction is opposite to what would be expected for the pure gradient-force effect (regardless of the sign of the optomechanical coupling), and there has to be a photothermal effect to cause the anomaly. Thus we conclude the photothermal effect exists in our system (which we will utilize for driving the membrane to sample the Casimir nonlinearity), and the photothermal effect and the gradient-force effect act in opposite directions. On the other hand, the mechanical frequency in both Figure 4.12(c,d) also first increases non-monotonically on the blue-detuned side of the optical resonance and decreases on the red-detuned side. It corroborates with the conventional optical spring effect due to the optical gradient force. This is expected as the small separation between the silicon device layers facilitates significant optomechanical coupling and the expression of the gradient-force effect should dominate over the photothermal effect. The relative optomechanical coupling strength of both optical resonances (of similar quality factor) can be compared by the following observation: In Figure 4.12(e) the mechanical linewidth reaches the minimal detection-limited value in the range of 1561.45nm to 1561.9nm, denoting the occurrence of self-oscillations at an input power as low as $5\mu W$, whereas in Figure 4.12(f), the mechanical lineshape does narrow in the red-detuned side but is still non-vanishing. Hence we infer that the resonance centered at 1561.25nm (C/L-band) has a slightly higher optomechanical coupling strength than the other resonance centered at 1606.32nm (U-band). Yet, due to the constraint of available laser powers (up to 2mW) for the C/L-band mode, the optical actuation is performed with the U-band mode instead (up to 13mW).

The existence of two optical modes with strong optomechanical response that are well situated in both the C/L band (1480-1580nm) and the U band (1580-1680nm)

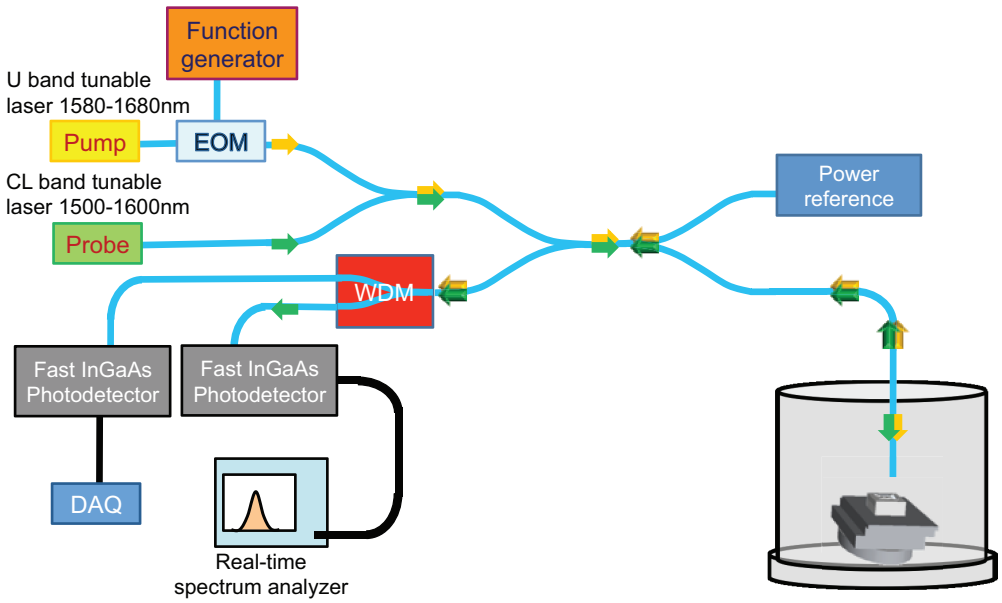

Figure 4.13: Experimental setup for coherently driving the PhC membrane: A tunable laser output in the U-band, intensity-modulated by an electro-optic modulator (EOM), is used to modulate the optical force and hence drive the PhC membrane resonantly. The modulator signal and DC bias to the EOM are provided by a function generator. The modulated output and a separate probe laser light from the C/L-band are combined by a 2×1 fiber coupled, which is then sent to one of the arms of a 2×2 fiber coupler. One of the output arms is used for calibrating the powers sent to the PhC membranes. The other output arm enters the vacuum chamber with a custom-made optical fiber feedthrough and illuminates the device under study. The reflected light is then collected by the same fiber tip and returns to the fiber coupler to reach the photodetector. The drive and probe signals are separated by a wavelength-division multiplexer (WDM). The probe signal is sent to a real-time spectrum analyzer, and the drive signal is sent to a data acquisition board (DAQ) for monitoring the coupling condition in case of mechanical drifts in the setup.

allows us to perform pump-probe measurements which are useful in (i) calibrating the membrane's oscillation amplitude by relating to the thermal motion, and (ii) differentiating between the actual nonlinear mechanical response and optical readout nonlinearity - a difficulty we encountered in the previous piezo-actuation experiment. As illustrated in Figure 4.13, the original fiber interferometry setup now incorporates a 2×1 fiber coupler that admits both the pump and probe lights. The signal reflected

by the device is then passed through a wavelength-division multiplexer (WDM) to separate out the pump and probe responses. The pump output is sent to a photodetector for monitoring the coupling condition to the membrane, which is subjected to mechanical drifts. The probe output is fed to an RF amplifier and then to the real-time spectrum analyzer. In the case of resonantly driving the PhC membrane by intensity-modulating the input light, the pump light will then be sent to an electro-optic modulator, which intensity-modulates the input laser power by sending in a sinusoidal drive signal from a function generator (or possibly a network analyzer), is included for providing a harmonic drive of the optical force.

Having characterized the optomechanical properties of the PhC membrane, we proceed to sample the mechanical nonlinearity (e.g. Casimir nonlinearity) of the system by inducing large-amplitude oscillations. Before we investigate resonance driving of the PhC membrane by amplitude-modulation of the input excitation power, we first explore the possibility of inducing large-amplitude motion by means of self-oscillations which we can easily achieve even at low CW excitation powers. The calibration of the oscillation amplitude of the membrane can be performed by introducing a separate probe light whose Brownian peak without any external pump serves as a calibration reference by relating to the thermal motion amplitude. For the simplicity of first-order analysis, here we assume the detuning of the probe light remains constant upon large optical excitation, i.e. optomechanical dispersion and/or thermo-optic effect of the probe light is negligible.[5]

[5]This assumption may be compromised at sufficiently large excitations due to the probe light's strong optomechanical coupling strength. In this case the transduction efficiency which is dependent on the optical detuning needs to be adjusted as the optical resonant frequency shifts as a result of optomechanical dispersion.

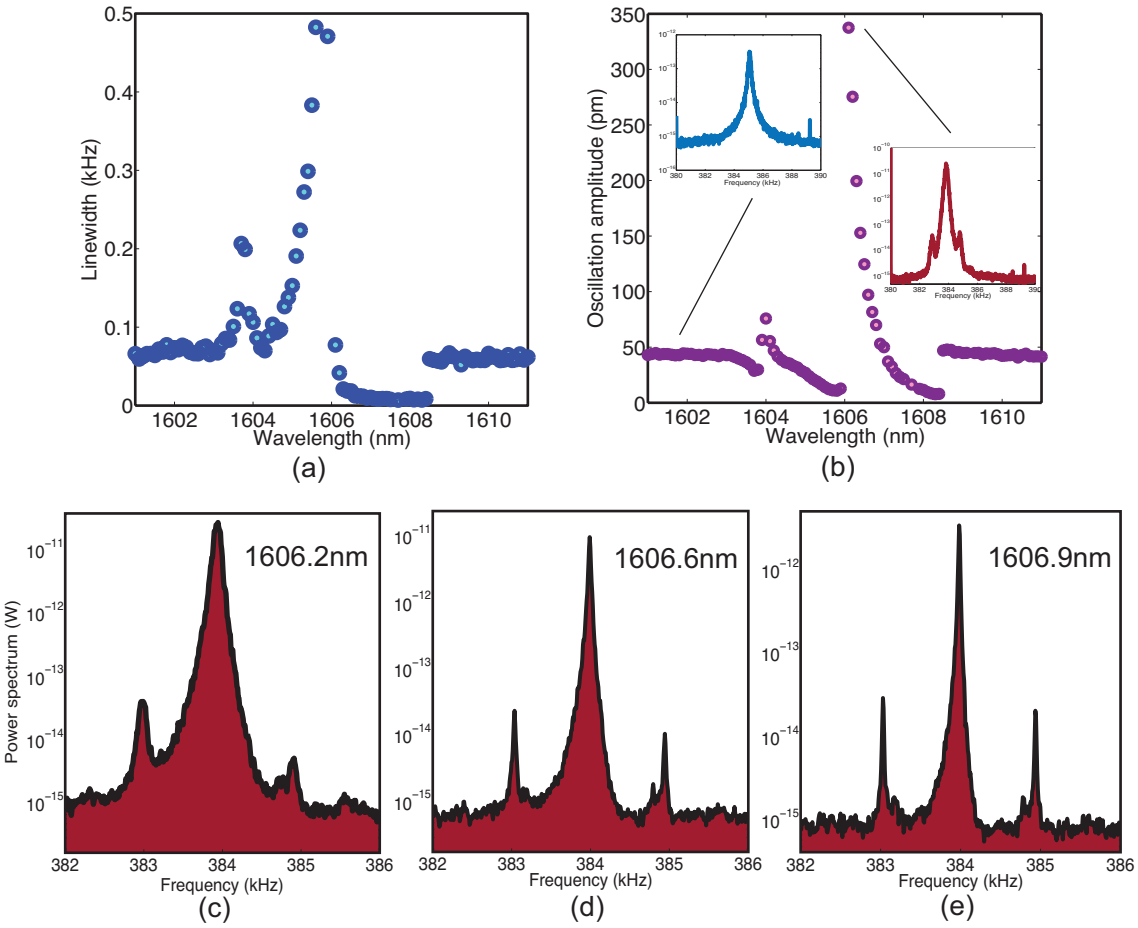

Figure 4.14: Large-amplitude motion induced by self-oscillations when the PhC membrane is pumped at 125μW: (a) The fitted mechanical linewidth across the optical resonance. Self-oscillations occur from 1606.2nm to 1608.8nm. (b) Calibrated oscillation amplitude obtained by comparing the relative areas of the mechanical response and scaling by the thermal motion. The inset (left-blue) shows the thermal motion transduced with the probe mode and (right-red) shows the transduced motion during self-oscillations. The maximum response obtained is 350pm. (c-e) show the mechanical spectra recorded at optical excitation wavelengths of 1606.2nm, 1606.6nm and 1606.9nm, which are on the red-detuned side of the pump mode. Note the increasingly conspicuous asymmetry towards the higher frequency. The side peaks are due to mixing of the turbo pump's vibration by the amplified motion of the mechanical resonance.

We illuminate the PhC membrane with a probe light of 1561nm at 5μW and a pump light in the U-band at 125μW. Only the transduced response of the probe light

is monitored with a spectrum analyzer. Figure 4.14(a) shows the optical spectrum of the resonance in the U-band. When the membrane is pumped off-resonance (e.g. in the range of 1601-1603nm, 1609-1611nm), the probe response remains unaltered and hence the response in those ranges can serve as the reference that relates the driven oscillation amplitudes to thermal motion. Using a motional mass of 3.67×10^{-13}kg, temperature of 300K, we estimate the unperturbed thermal motion amplitude to be $\approx$ 44pm. Then we calibrate the membrane's oscillation amplitudes across the pumped optical resonance by comparing the area under the curve of the transduced signal. (Note that the area under the curve gives the squared value of the motion amplitude, and thus one has to take the square root of the area to obtain the amplification factor of the reference thermal motion.) The calibrated result of the amplified oscillation amplitude is plotted in Figure 4.14(b). At the current pump power of 125μW, the maximum amplitude is $\approx$0.34nm at 1606.1nm. We observe the the mechanical spectra in the red-detuned range, where mechanical motion is dramatically amplified, are skewed from the Lorentzian lineshape. Three instances of this asymmetry are shown in Figure 4.14(c-e) where the respective pump wavelengths are 1606.2nm, 1606.6nm and 1606.9nm. Careful inspection of the lineshapes leads to the observation of lightly lopsided lineshapes tilted towards the higher-frequency edge, signifying the occurrence of mechanical hardening nonlinearity. This is opposite to what is expected in the presence of the Casimir force where the mechanical nonlinearity is a softening one upon large mechanical oscillation. To understand the origin of the hardening nonlinearity, we first review the physics of the optomechanically driven self-oscillator. In the presence of thermal noise, the PhC membrane is excited by CW light which exerts

an optical gradient force and an "antagonistic" photothermal force whose strengths explicitly and implicitly depend on the membrane-substrate separation x. The time delay present in the build-up of the photothermal force is translated to positive or negative work done on the membrane which amplifies or damps the motion of the membrane. When the motion is sufficiently amplified that elicits non-negligible response from higher-order nonlinear forcing terms (due to the intrinsically nonlinear gradient force, photothermal force and even the Casimir force), the mechanical susceptibility now deviates from the Lorentzian form in the linear case: the mechanical frequency has nonlinear dependence on the oscillation amplitude. The equation of motion in the presence of nonlinearity now reads

$$\ddot{x} + (\Gamma_{m0} + \Gamma_m^{ptm})\dot{x} + \left[\Omega_{m0}^2 + (\Omega_m^{opt})^2 + \sum_i \alpha_i x + \sum_i \beta_i x^2\right] x \quad = f_L(t) \qquad (4.2)$$

, where Γ_m^{ptm} is the mechanical linewidth modification by the photothermal force, Ω_m^{ptm} is the angular mechanical frequency modification by the optical gradient force, $\sum_i \alpha_i x$ and $\sum_i \beta_i x^2$ represent frequency modification due to the respective quadratic and cubic nonlinearity from the Casimir force, optical gradient force and the photothermal force. As we delay the discussion of the optical-force-induced nonlinearity to the following session, we point out that a simplified situation of a Duffing oscillator driven by a white noise was studied by Dykman in the 80's.

Though self-oscillations can be exploited to drive the PhC membrane by a large amplitude without introducing a modulator and function generator, which is an appealing approach in a real-life detection environment, the dynamics of such positive-feedback nonlinear system can be quite complex. To help decipher the different sources of nonlinearities in our current system, we resort to the conventional reso-

nant drive scheme. Here we resonantly drive the membrane with an optical force where the excitation light is intensity-modulated with an electro-optic modulator (EOM) [55]. The detection method is as follows: A sinusoidal signal is sent to the EOM to modulate the input laser light. Increasing the signal amplitude increases the modulation depth. A DC bias is also applied to the EOM to ensure a maximum linear output. The rest of the pump-probe setup remains the same as the previous pump-probe experiment. Here the optomechanical system now is driven by a single-frequency excitation as opposed to the broadband thermal noise in the previous experiment. To observe the mechanics bistability at large drive amplitude, a frequency sweep of the modulation signal is provided, while the spectrum analyzer captures the spectral response for each frequency excitation. The aggregate amplitude response for demonstrating the mechanical bistability is obtained by choosing the MAXHOLD function of the analyzer where only the maximum response for each resolved frequency component throughout the entire frequency sweep is recorded. At an input power of 31.25μW,[6] we drive the PhC membrane at several fixed wavelengths across the optical resonance centered at 1606.1nm. As for the drive signal, at each modulation amplitude (0.05V_{pp}, then an increment of 0.1V_{pp} from 0.1-0.6V_{pp}) the frequency sweeps from 380kHz to 390kHz. Figure 4.15(a) shows the optical resonance of the PhC when statically pumped at 31.3μW. Optical bistability occurs at ≈1606.1nm, then self-oscillations take place until 1607.3nm. Figure 4.15(b-d) show the driven, mechanical response for three different excitation wavelengths, namely 1605.9nm, 1606.1nm and 1606.15nm. At 1605.9nm which is on the blue-detuned side

[6]Nominally 1mW from the laser but discounted to 1/8 of the power after passing through the EOM and further reduced through the fiber coupler

of the optical resonance (Figure 4.15(b)), the mechanical resonance is centered at 386.55kHz, which is different from the value reported earlier due to the optical spring effect incurred by the pump light. As the drive amplitude increases, the amplitude of the driven response rapidly increases. Moreover, the frequency at which the driven resonance peaks gradually decreases, and the lineshape deviates from the Lorentzian form. At a drive amplitude of $0.3V_{pp}$, mechanical bistability occurs at the transition frequency of 385.62kHz. This type of mechanical nonlinearity is known as mechanical softening nonlinearity. At 1606.1nm which is very close to the transition wavelength of the optically bistable resonance pumped at 31.3μW (Figure 4.15(c)), again the driven response amplitude increases upon increasing modulation strength. However the mechanical frequency does not display much shift (from 384.75kHz at low drive to 384.95kHz at $0.6V_{pp}$) and the lineshape remains Lorentzian. Finally, at 1606.15nm where the PhC membrane undergoes self-oscillation (signified by the amplified response in the mechanical spectrum), mechanical bistability occurs readily at a low modulation amplitude of $0.1V_{pp}$, but towards the higher frequency side. This type of nonlinearity is known as mechanical hardening nonlinearity.

A systematic investigation of recording the mechanical driven response at a number of excitation wavelengths across the optical resonance shows a consistent trend of mechanical softening nonlinearity on the blue-detuned side of the optical resonance and hardening nonlinearity on the red-detuned side. Given all other experimental conditions held constant, we infer that the mechanical nonlinear behaviors observed are due to the intrinsically nonlinear optical force. In principle, a blue-detuned optical force excitation leads to stiffening of the spring constant as illustrated in Figure

4.12(c) [132]. One expects the nonlinear mechanical frequency blue-shifts and eventually the bistable transition happens at a frequency higher than the initial resonant frequency. The same reasoning applies to the red-detuned optical excitation as well. However the trends we observe are opposite to the expected results. We are still investigating the origin of such phenomena. The additional physics pertinent to this system but yet to be considered include (i). the concurrent driving of the optical spring constant and the mechanical linewidth, (ii). relative strengths and effects of the quadratic and cubic nonlinearity due to the optical force, and (iii). the role of photothermal force in the nonlinear dynamics.

As a concluding remark for this section that delineates rich optomechanical nonlinear dynamics, we note that our initial vision of sampling the Casimir (mechanical softening) nonlinearity may be masked by the nonlinear response due to the optical force. However when the Casimir nonlinearity is sufficiently large, we expect the softening nonlinearity could offset or enhance the measured nonlinearity across the optical resonance depending on the optical detuning of the excitation.

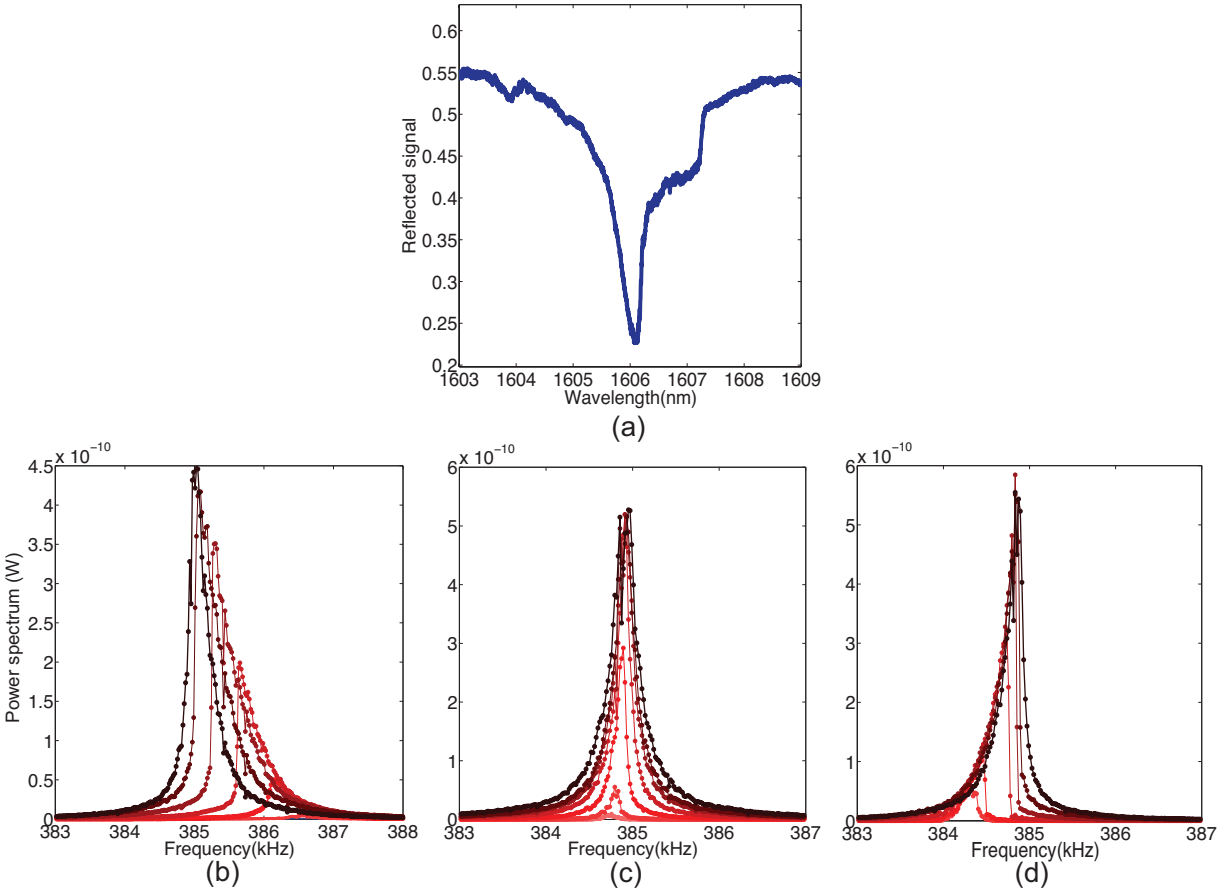

Figure 4.15: Mechanical nonlinear response of the PhC membrane upon resonant excitation: (a) Optical resonance excited at 31.3μW for exerting an optical force on the membrane. Note the occurrence of optical bistability. Mechanical response of the membrane upon the excitation of an optical force whose amplitude is modulated from 380kHz-390kHz at (b) 1605.9nm, (c) 1606.1nm and (d) 1606.15nm. The response with different modulation depths (0.05, 0.1, 0.2, 0.3, 0.4, 0.5 and 0.6V_{pp}) is shown (darker shades of red represent larger modulation depths). (b) shows mechanical softening nonlinearity upon blue-detuned excitation; (c) has minute mechanical nonlinear response; (d) shows mechanical hardening nonlinearity upon red-detuned excitation.

Chapter 5

Towards calibrating the electrostatic effects in Casimir force measurements

5.1 The role of electrostatic effects in Casimir experiments

Virtually, most Casimir experiments in the literature measure the Casimir-induced frequency gradients over a range of separations of the test bodies. Often, the Casimir effect is mingled with other competing effects caused by attractive potentials. A major competing artifact in Casimir measurement is the electrostatic interaction between the test bodies [133, 134, 135, 127]. Though the power laws for the Casimir force and the electrostatic force with respect to the test-body separations are dif-

ferent, the magnitude and gradient of the electrostatic force are comparable to that of the Casimir force in the range where the test-body separation is above 100nm. An important step of characterizing the Casimir potential, whether in a static or dynamic mode of measurement, involves minimizing and calibrating the electrostatic effects on the Casimir oscillator. Extracting the contributions due to the Casimir and electrostatic forces could incur much uncertainties without understanding the relevant physics of the system under test. For instance, one of the ongoing controversies of Casimir physics is the choice between the Drude model and the plasma model in calculating the Casimir force: the DC (zero-frequency) contribution of the dielectric function of the test bodies can cause a difference of 200% in the force magnitude calculation [136]. Hence the existence of the electrostatic artifacts can obscure the understanding of some unsettled issues in Casimir physics. The sources of such electrostatic effect are contact potential and patch charges. Below we describe the origin of these sources, how they are quantified and minimized experimentally in typical Casimir measurements.

5.1.1 Contact Potential

When two metals or dielectrics of different work functions are in contact, a potential is established between them. A simple experiment to illustrate this can be performed by clamping two different pieces of metals, say potassium and calcium, with crocodile clips which are connected to a voltmeter; one obtains a finite voltage measurement. Such potential difference could be minimized, or even balanced out, by applying a bias across the two bodies concerned. Denoting the contact potential

as V_m, and the applied bias as V, the energy stored between two parallel plates with area A separated by distance d is given by

$$U_{CP} = \frac{1}{2}C(V - V_m)^2, \tag{5.1}$$

where the capacitance of such capacitor is given by $C = \epsilon_0 A/d$. Thus, the attractive force on the parallel plates is given by

$$F_{CP} = -\frac{\partial U_{CP}}{\partial d} = -\frac{1}{2}\frac{\epsilon_0 A}{d^2}(V - V_m)^2. \tag{5.2}$$

In most Casimir force measurements, a proper calibration is performed by first moving the bodies (usually a sphere and a plane) sufficiently far away that the Casimir effect is negligible. A bias is applied to the two bodies which measures the displacement of the moveable body. By calibrating the absolute separation between the two bodies interferometrically or electrostatically, one could fit the contact potential by sweeping over a range of voltages. In particular, when the bias is set at the contact potential, it eliminates the force contribution due to the potential difference between the two paralle plates. Alternately, the electrostatic force serves to drive the oscillatory motion of an object and the freqeuncy shift from its natural mechanical frequency is measured as the bias varies. The contact potential V_m is extracted likewise.

It is observed in several experiments that V_m, also known as minimizing potential, could be distance-dependent due to varying contact potential across the membranes as a result of stresses and membrane curvatures, etc. This might not be problematic as our case if the membranes are reasonably flat and the effective area is exactly the area of the membranes. Accounting for the distance dependence in V_m, one rewrites

the electrostatic force as

$$F_{CP} = -\frac{1}{2}\frac{\epsilon_0 A}{d^2}(V - V_m(d))^2. \tag{5.3}$$

It is suggested that "although the parabola measurement minimizes the electrostatic force across the plates, it does not necessarily *nullify* all the electric forces that possibly exist.

5.1.2 Patch potential

Patch effects are due to work function variations across a surface due to grain boundaries in polycrystalline materials (different effective masses in different crystal directions, dipole moments due to polar molecules on the surface (e.g. native oxide film on non-passivated silicon surfaces), impurities, etc [137, 138, 139]. One could map out the surface patch potentials with a scanning Kelvin probe. The state of the art of the technique has a spatial resolution of several microns and has a sensitivity of about $30mV$. In Lamoreaux's experiment with Ge torsional balance, the root-mean-square voltage due to such patch effect is fitted to be around $6\pm2mV$ [95].

The theoretical treatment is by defining a two-point correlation function in the $k-$space. Three important scales are the typical dimension of a patch λ, membrane separation d and the membrane size A. In the limiting case of the patch size greater than the membrane separation, the force due to the patch field is given by

$$F_{patch}(\lambda > d) = -\frac{1}{2}\frac{\epsilon_0 A}{d^2}V_{rms}^2. \tag{5.4}$$

In the opposite limit where the membrane separation is greater than the patch size, the force is now exponentially suppressed, i.e. $F \propto e^{-d/\lambda}$. In the intermediate regime,

the functional form of the interaction energy of the plates due to the patches is given by

$$U_{pp} = \frac{\epsilon_0}{4}\int_0^\infty dk k^2 \left(\frac{2cosh(kd)}{sinh(kd)} - 2\right) S(k) = \frac{\epsilon_0}{2}\int_0^\infty dk \frac{k^2 e^{-kd}}{sinh(kd)} S(k), \tag{5.5}$$

where $S(k)$ is the Fourier transform of V_{rms}^2 defined via the correlation functions across isotropic patches in the $k-$space. However, it is best to avoid this regime because measuring the correlation function is beyond the technological limit. Yet, emerging atomic force microscopy technologies like Kelvin Peak Force Microscopy allows one to map the local potential distribution with a spatial resolution of tens of nanometers. Being able to map such spatial correlation allows us to even check if lateral force exists. The application of such nanoscale detection techniques to Casimir experiments is deemed to bring new understanding of the patch potentials as we verify various proposed models in explaining the extent of the electrostatic effect observed as the Casimir effect is carefully distilled.

5.1.3 Model for total electrostatic residual force

Kim et al. proposed a model to account for the electrostatic residual force with good experimental fits in several different Casimir force measurements [134]:

$$F_r^{el} = F_0 + F_{CP} + F_{patch} = F_0 + \frac{1}{2}\frac{\epsilon_0 A}{d^2}\left[(V_1 + V_m(d))^2 + V_{rms}^2\right], \tag{5.6}$$

where F_0 is an offset at large distances possibly due to instruments and other D.C. effects. $V_m(d)$ is measured and could even be non-distance-dependent for inert, smooth, flat, and highly conducting materials, e.g. gold. As a survey of the empirical data in various experiments, Table 5.1 summarizes some of the estimated minimizing poten-

Experiment (Year)	Minimizing contact potential, V_1	Patch potential
Ge plates, 500nm-5μm, Kim et al (2009)	22-28mV, -34± 3mV	6± 2mV
Au plates, 700nm-7μm, Sushkov et al (2011)	20± 0.2mV, NA	5.4±0.1mV
Cr-on-Si plates, 0.5-1.1μm, Bressi et al (2002)	-68.6mV, NA	NA

Table 5.1: A table of estimated contact potentials and patch potentials in several Casimir experiments

tial (range).

5.2 Electrical degree of freedom in Casimir optomechanical oscillators

The strategies of evaluating and minimizing the electrostatic effect in our integrated optomechanical system have to be modified compared to the procedures established in previous Casimir demonstrations for the following reasons: First, in a vertically integrated system, the ability to perform a pure electrostatic calibration by separating the test bodies to the micron scales is limited by the actuation mechanism (i.e. the ability to actuate without introducing a significant spring constant which masks the interested frequency shifts due to residual potentials) and range of the system. Second, our approach of averaging out the variability of individual devices by measuring multiple devices requires new designs that allow for individual electrical control. In the following sections, we discuss our effort in building an electrically addressable optomechanical system on the chip level and the hardware level.

5.2.1 Development of an electrically addressable optomechanical system

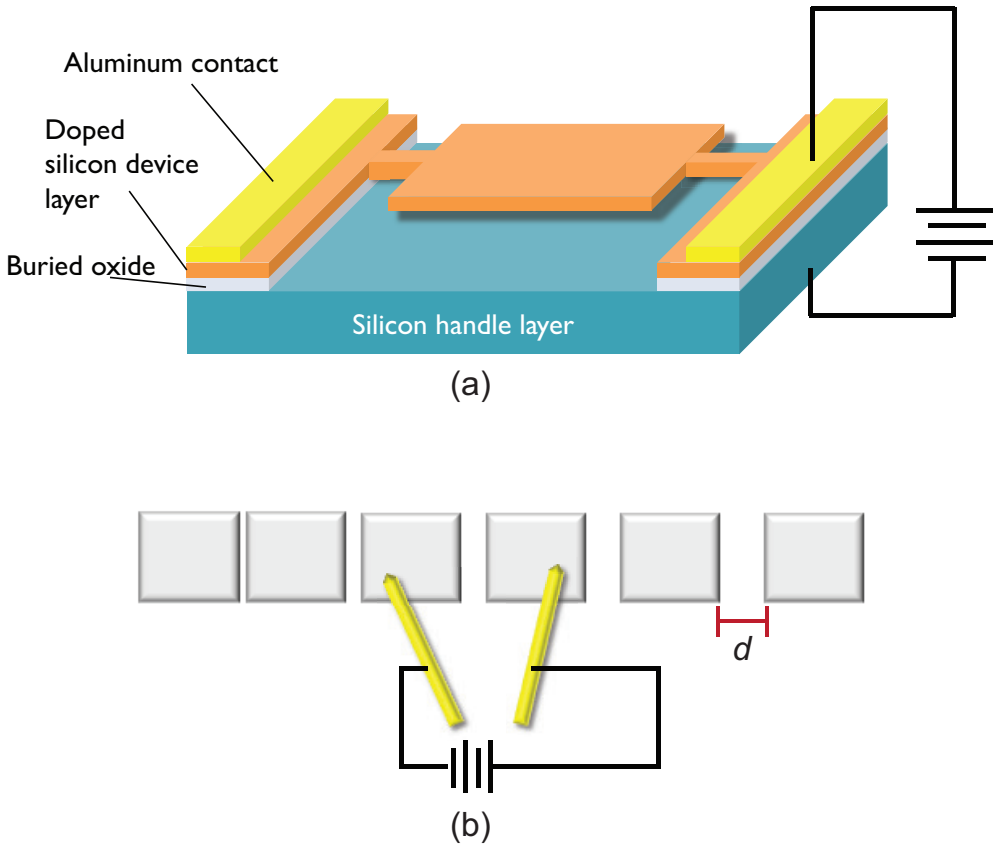

Figure 5.1: (a) Schematic for measuring the contact potential in the photonic crystal platform. Aluminum contacts are formed. The mechanical frequency of the membrane is monitored upon different biases. (b) Schematic for the transmission line method (TLM) for characterizing contacts and extracting the contact resistance. d is the separation between two neighbor contacts.

The double-SOI substrate we employ to develop the existing optomechanical system is intrinsically doped with a doping level of $\times 10^{15}/cm^3$. Metallic contacts formed with such low-doped silicon have large contact resistance and non-Ohmic response. Significant dissipation at the metal-silicon contact could forbid us from estimating the contact potential while minimizing the electrostatic effect is still possible. Hence,

the idea of biasing the top silicon device layer and measuring its interaction with the bottom substrate is implemented by first establishing the biasing technique and the detection method of electrostatic force gradients in a simpler, more controlled platform of single SOI substrate. The schematic is illustrated in Figure 5.1(a). Electrical contacts are formed by forming ohmic contacts with a metal and doped silicon. The substrate (silicon handle layer) is grounded. Bias is applied between the top silicon device layer and the handle layer, and the mechanical resonant frequency upon this biasing is measured accordingly.

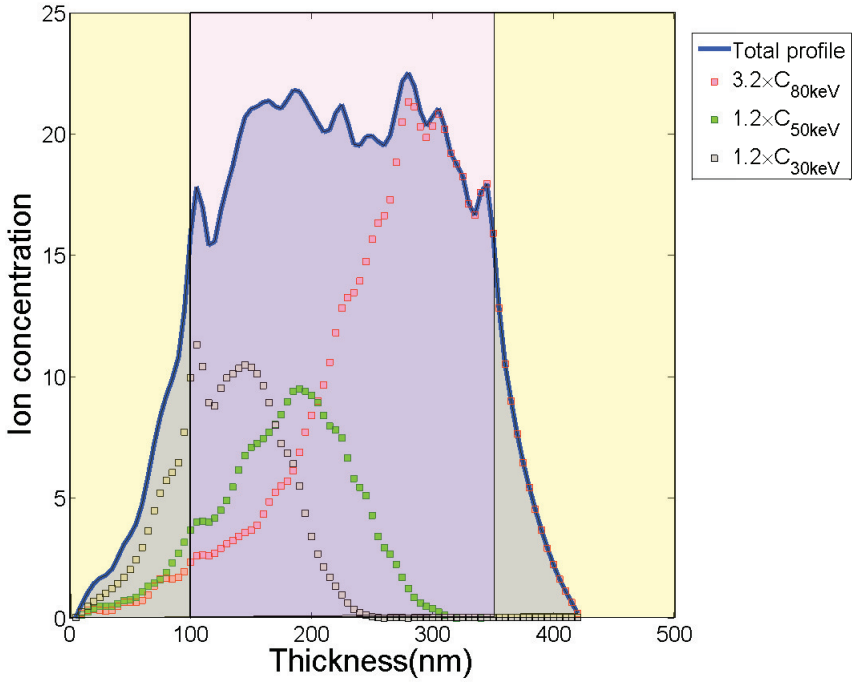

Figure 5.2: Multiple ion energies for a flat doping profile obtained by SRIM simulations: the relative doses of 35keV (grey squares), 50keV (green squares) and 80keV (pink square) ions are adjusted to obtain a flat doping profile (blue line). The x-axis represents the cross-sectional dimensions of the first few layers of SOI: 100nm of PECVD oxide; 220nm of silicon device layer; the remaining is part of the buried oxide layer.

To ensure the formation of good ohmic contacts, we dope the silicon device layer

Doping level	Dose of 35keV ion	Dose of 50keV ion	Dose of 80keV ion
$10^{17}/cm^3$	$5.8\times10^{11}/cm^2$	$5.8\times10^{11}/cm^2$	$15.4\times10^{11}/cm^2$
$10^{18}/cm^3$	$5.8\times10^{12}/cm^2$	$5.8\times10^{12}/cm^2$	$15.4\times10^{12}/cm^2$
$5\times10^{18}/cm^3$	$2.9\times10^{13}/cm^2$	$2.9\times10^{13}/cm^2$	$7.7\times10^{13}/cm^2$
$8\times10^{18}/cm^3$	$4.6\times10^{13}/cm^2$	$4.6\times10^{13}/cm^2$	$12.3\times10^{13}/cm^2$
$10^{19}/cm^3$	$5.8\times10^{13}/cm^2$	$5.8\times10^{13}/cm^2$	$15.4\times10^{13}/cm^2$

Table 5.2: Dose of 35keV, 50keV and 80keV ions required for doping levels of $10^{17}/cm^3$, $10^{18}/cm^3$, $5\times10^{18}/cm^3$, $8\times10^{18}/cm^3$, and $10^{19}/cm^3$.

with boron ion to at least $5\times10^{18}/cm^3$. Such doping level forms a good quasi-ohmic contact with the contact electrode of aluminum. It is known that uneven doping could generate stress gradient to the device layer which may cause unwanted mechanical response. Hence, care is taken in creating an even doping profile along the device layer cross section by multi-dose, multi-energy doping simulated by SRIM. Since the minimum ion energy allowed for ion implantation already reaches the middle of the device layer. 100nm of PECVD oxide is first deposited on the SOI substrate, such that ions with the minimum energy can reach the top side of the silicon layers. The resultant doping profile is illustrated in Figure 5.2. The energies and the corresponding doses selected to achieve the doping levels of $10^{17}/cm^3$, $10^{18}/cm^3$, $5\times10^{18}/cm^3$, $8\times10^{18}/cm^3$, and $10^{19}/cm^3$ are listed in Table 5.2:

As an initial step of evaluating the ability of detecting force gradients due to the electrostatic force between the silicon device layers, several single SOI substrates are sent for boron ion implantation at Materials Diagnostics to the doping levels listed above. The dopants are then activated by annealing the the doped samples with rapid thermal annealing at 1000°C with forming gases for a minute. To ensure compatibility with the silicon reactive ion etcher, aluminum is chosen as the metal for forming ohmic contacts with the doped silicon. The ohmicity of the aluminum-silicon contact

of each doping level was carefully characterized using the transmission line method/ transfer length method (TLM) which is widely used by the semiconductor industry. Briefly, a series of six 100μm×100μm aluminum squares (with neighboring separations of 5μm, 10μm, 15μm, 20μm, 25μm) are formed by standard photolithography and lift-off processes. The contacts formed are then annealed at 420°C for 1 minute in forming gases to establish stronger bonding at the interface of aluminum and silicon. As illustrated in Figure 5.1(b), each pair of neighboring square contacts are then tested with a semiconductor analyzer to obtain the *I-V* curves which illustrate the ohmicity of the aluminum-silicon contact and the differential resistance between two contacts. A series of *I-V* curves of the five contact pairs (with neighboring separations of 5μm, 10μm, 15μm, 20μm, 25μm) made with $10^{17}/cm^3$ doped silicon and made with $5\times10^{18}/cm^3$ doped silicon are shown in Figure 5.3 and 5.4 respectively. In the measurements, the voltage applied goes from -10V to 10V [1]. The differential resistance at each bias voltage is obtained by numerically differentiating the *I-V* curves as shown in the bottom panel of Figure 5.3 and 5.4. At the doping level of $10^{17}/cm^3$, the aluminum-silicon junction forms a Schottky barrier, which gives the nonlinear *I-V* curves shown in Figure 5.3. The differential resistance in the low-voltage range is as high as $10^5\Omega$. On the other hand, at the doping level of $5\times10^{18}/cm^3$, the *I-V* curves are more linear which means the Al-Si junction resembles an ohmic contact. From the differential resistance plots, we notice variations of the resistance over the bias range, but the values remain fairly consistent overall. For the Casimir measurements, since we are not interested in applying large voltages to actuate the membranes but in

[1]The voltage applied only goes from -8V to 8V or even with a smaller range for the contact pair with a gap of 5μm since the contacts melt upon large bias.

reducing the contact potential which is usually in the sub-Volt range, the differential resistance chosen for the TLM extraction of the contact resistance is chosen within the low-voltage range. Figure 5.5 plots the measured resistance at zero bias for each contact pair extracted from Figure 5.4 as a function of the contact separations. It is then fitted to a linear form where the y-intercept gives twice of the contact resistance at the Al-Si junction according to TLM. Here the extrapolated contact resistance is 50.2Ω. For higher doping levels, we achieved contact resistance ≈5Ω.

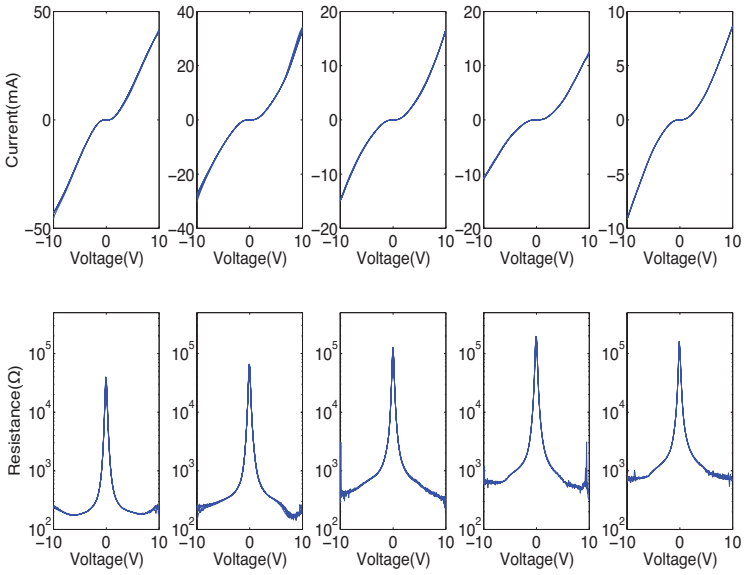

Figure 5.3: I-V curves for contact pairs where the contact metal is aluminum and the silicon layer is $10^{17}/cm^3$ boron-doped, with separations (from left to right) of 5μm, 10μm, 15μm, 20μm, 25μm. The bottom panel shows the differential resistance at each bias voltage. The resistance is plotted in the logscale due to the range the resistances vary over.

Although the contact resistance can be minimized by choosing the highest doping levels available, large optical absorption occurs which could diminish the optomechanical performance and induce large thermo-optic effect. Hence there is a trade-off in optimizing the electrical and optical properties. With reference to the results pre-

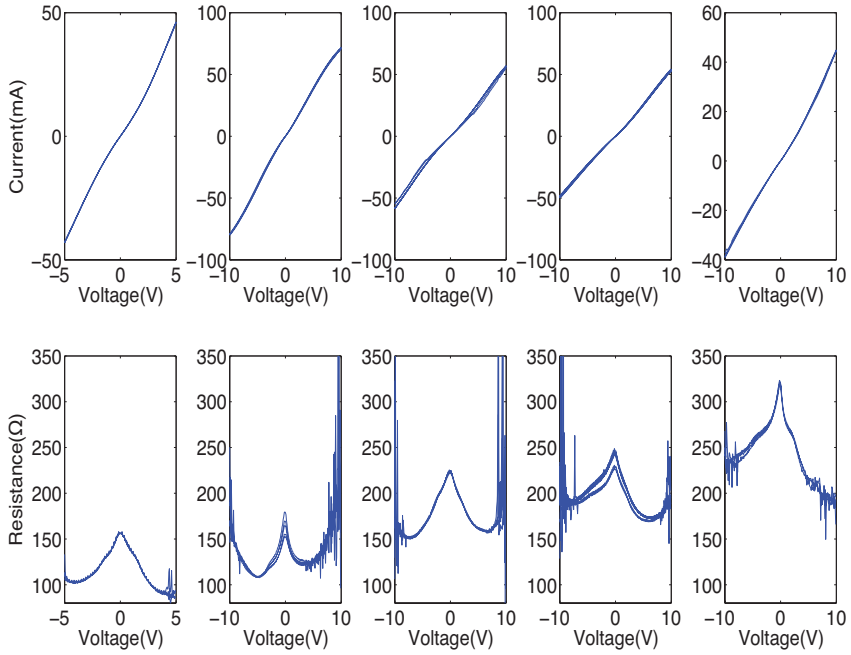

Figure 5.4: I-V curves for contact pairs where the contact metal is aluminum and the silicon layer is $5\times10^{18}/cm^3$ boron-doped, with separations (from left to right) of 5μm, 10μm, 15μm, 20μm, 25μm. The bottom panel shows the differential resistance at each bias voltage. The resistance is plotted in the linear scale as the resistance is consistent within a similar magnitude.

sented in [140], we choose the doping level of $8\times10^{18}/cm^3$ for fabricating Casimir photonic MEMS oscillators.

Our attempt of on-chip integration of arrays of Casimir oscillators and elucidating other attractive contributions requires us to individually biasing the devices. Addressing tens or even hundreds of devices in a vacuum environment could be challenging. However, as we learnt from the ion-trap communities where on-chip preparation of multiple RF trap sites in an ultra-high vacuum is not uncommon, we adopt their architecture for large-scale electrical characterization of the devices in a high vacuum environment using ceramic pin grid array (CPGA).

Due to the relatively large difference in length scales of the photonic crystal de-

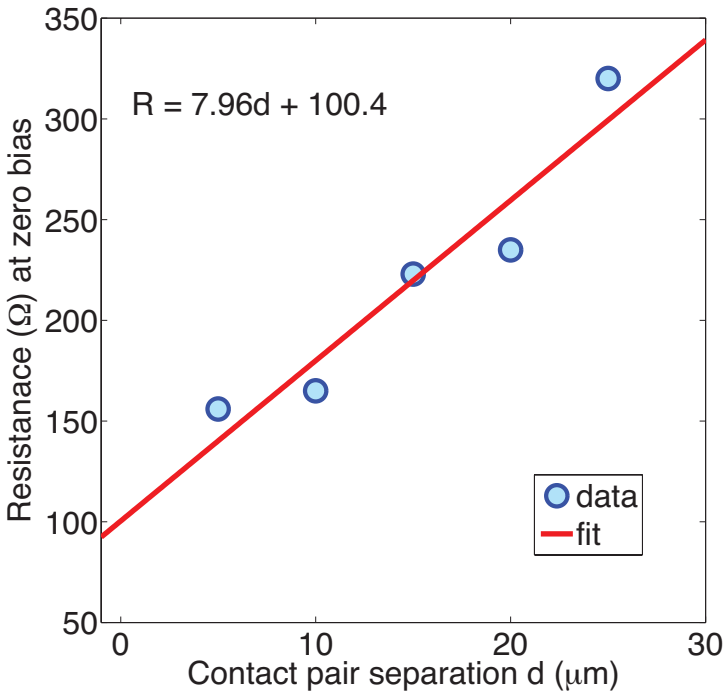

Figure 5.5: Extrapolation of the contact resistance for contacts made with doping level of $5\times10^{18}/cm^3$: Transmission line method is applied where the resistance values of the five contact pairs at zero bias are plotted against the contact pair separations d. The data are fitted to a linear form. From the y-intercept, the contact resistance of the Al-Si junction is $\approx 50.2\Omega$.

vices relative to the metallic contact pads, packaging of hundreds of devices could be challenging. Figure 5.6(a) shows the layout for fabricating 54 devices on a 1cm × 1cm sample. Aligned electron-beam lithography and photolithography are performed to define the photonic crystal patterns, the metallic contacts and the electrical isolation trenches. Figure 5.6(a) shows the optical micrograph of a partial view of the finished sample. The sample is then mounted on a 108-pin CPGA [2] with Electrodag-502 (for eliminating the strong coherent reflections from the bottom of the silicon handle layer). Wirebonding (with aluminum threads) is then performed to connect each

[2]Spectrum Semiconductor Materials, Inc. CPG1081

metallic contact pad to the designated pins of the CPGA. Finally, the underlying sacrificial oxide layer is to be removed by vapor hydrogen fluoride etch to release each individual photonic crystal membrane [3].

5.2.2 Plug-and-play strategy for large-scale electrical characterization in a vacuum environment

On the hardware level, we envision an electrical platform that admits a plug-and-play solution for quick turn-over of samples. However, the involvement of more than 50 electrical connections poses some challenges to finding the appropriate vacuum components. Having access to a flange with two 50-pin sub-D electrical feedthrough, we use a vacuum-compatible teflon ribbon cable [4], connected to two 25-pin sub-D connectors on one end to the feedthrough, to facilitate multi-site electrical contacts. The other end of the ribbon cable is soldered to the designated pins of a fiber-glass chip carrier [5] for the CPGA (shown in Figure 5.6(d)), which is to be permanently mounted to the experimental setup.

While the samples and components are ready, electrostatic calibration with these hardware changes will be underway as soon as the study of the nonlinear mechanics with optical force is finished.

[3] As noted in Appendix A, the sample needs to be raised to 35°C. Thermal conduction through the much reduced contact area should require the sample to be heated on the etchant platen for a longer time to ensure minimal water condensation which leads to stiction.

[4] Accuglass 6-101557: 2 X 25 Way FEP Ribbon Cable with Socket (Female) and DAP D-Connector on one end and female contacts on the other, 19" Long.

[5] Ironwood Electronics SK-PGA12/108A-01

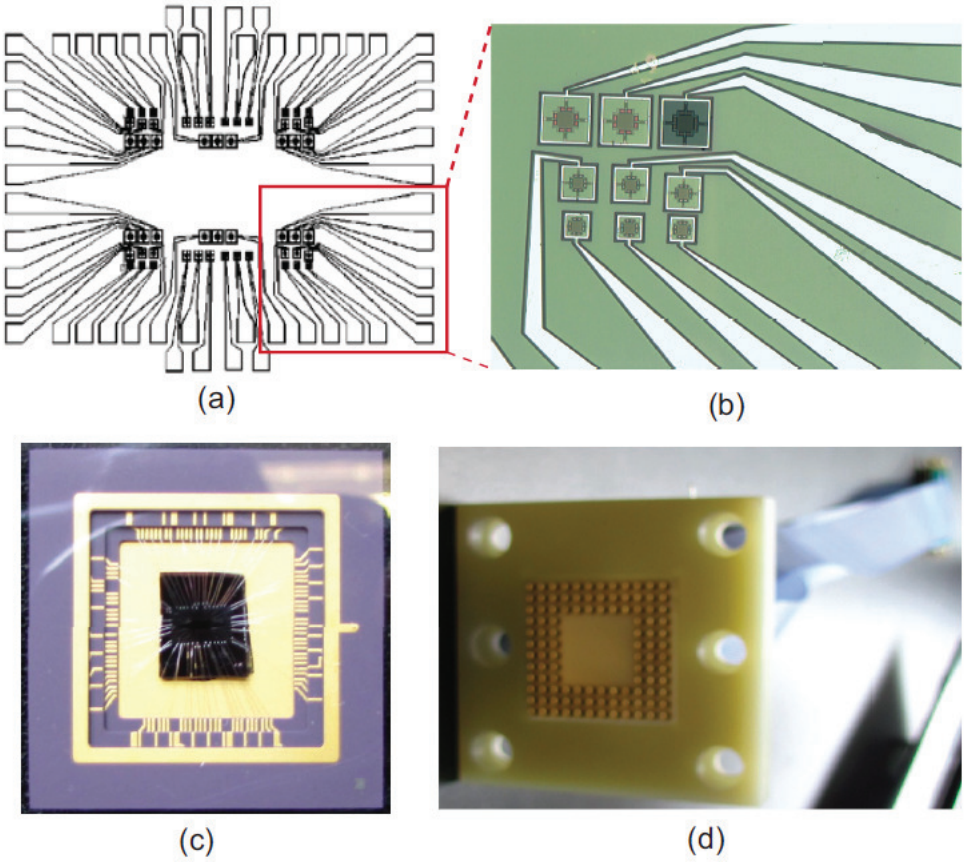

Figure 5.6: (a) Layout of 54 devices which can be electrically addressed individually; (b) Optical micrograph of the fabricated sample. Each aluminum electrode leading towards the PhC membrane is isolated. (c) Sample wirebonded to a 108-pin CPGA carrier. (d) A CPGA sample holder soldered to a 50-wire ribbon cable which is to be connected to an electrical feedthrough.

Chapter 6

Conclusion and future outlook

6.1 Conclusion

Starting with the ambition of developing an all-integrated optomechanical platform for probing the Casimir force, we developed an asymmetric system of a photonic crystal membrane coupled to an silicon-on-insulator substrate. With novel stress management techniques, lithographically defined tunability of optomechanical coupling is realized and probed with fiber interferometry in vacuum. The optomechanical properties, including static deformation by the repulsive optical gradient force, optical spring effect, and dynamic backaction, are fully characterized. Our study reveals the interplay of the optical gradient force and the photothermal force. Optomechanical cooling and amplification mediated by the photothermal force are also demonstrated. The implications of this investigation to the development of a Casimir oscillator are: 1. Displacing the photonic crystal membrane with a repulsive optical force by an amplitude of 1nm/mW is possible; 2. probing the Casimir-induced mechanical frequency

shifts while pumping the membrane to drive it closer to the substrate is susceptible to large optical spring effect; 3. large-amplitude motion due to self-oscillations may be exploited for sampling the Casimir nonlinearity.

We explored three different approaches of measuring the Casimir-induced force gradients, namely multiple-device characterization, piezo-drive and optomechanical drive. The first approach of measuring the mechanical frequencies for numerous devices with various membrane-substrate separations, though enjoying some initial success, is shown to be problematic due to the abnormally large mechanical frequencies of these suspended membranes.

The second approach involves resonantly driving a photonic crystal membrane with a piezo-actuator to sample the Casimir nonlinearity. Harmonics of the fundamental mechanical mode appear, possibly due to optomechanical readout nonlinearity and/or actual frequency generation mediated by quadratic and cubic nonlinearity. Upon increasing driving strength, the thermal peak moves further away from the drive signal and eventually a symmetric side peak on the other side of the drive signal emerges. Finally mechanical mixing mediated by quadratic and cubic nonlinearity leads to mechanical signatures in the frequency range well below the fundamental mechanical resonant frequency.

The third approach is to resonantly drive the photonic crystal membrane with an optical force. A pump-probe system is adopted to separate out nonlinear readout artifact in the measurements. Optical detuning-dependent mechanical nonlinearity (blue-detuned softening and red-detuned hardening) can be observed. Further work is required to understand the origin of optical force nonlinearity and elucidate the

interplay of such nonlinearity with the Casimir force.'

Finally we reported on the progress of establishing the capability of electrically addressing photonic crystal membranes in a vacuum environment. The doping level required for creating ohmic contacts using aluminum as the contact metal is evaluated using the transmission line method. Photonic crystal membranes with individual, isolated electrical contacts are fabricated with SOI substrates uniformly doped with $8\times10^{18}/cm^3$. The samples are wirebonded to a CPGA carrier and ready to be released with vapor hydrogen fluoride etch. A plug-and-play strategy compatible with the vacuum environment is also developed for interfacing with the wirebonded samples.

6.2 Future outlook

Numerous opportunities arise in the course of developing the Casimir optomechanical oscillator. In this section, we consider four areas which are worth exploring, namely alternate approaches of probing the Casimir force, nonlinear optomechanics, lateral optomechanical sensing and soft-lithography-enabled hybrid systems.

Alternate approaches of probing the Casimir force

In the piezo-drive experiment, we were not able to demonstrate mechanical bistability and hysteresis due to the multi-resonant features of the piezo-actuator employed. Recently a piezo-actuator with flat response output well into the MHz range is available. The ability of demonstrating mechanical nonlinearity (and even mixing) when the membrane is driven by a relatively small amplitude would be a decent demonstration of a highly nonlinear potential in the system.

Another approach is to design a system where the test body for the Casimir effect is connected to other free-standing structures, which are susceptible to direct electrostatic actuation. The central test body will then be displaced accordingly without experiencing the electrostatic spring effect. By probing the mechanical mode whose motion is largely localized to the test body, an on-chip method of directly actuating and probing the Casimir effect is proposed.

Nonlinear optomechanics

In Chapter 5, we demonstrate the rich nonlinear mechanical features present in our current coupled PhC membranes. The full model that explains (i) mechanical softening nonlinearity on the blue-detuned side of the optical resonance and vice versa, and (ii) Mollow-triplet-like features due to the non-trivial interactions of a strong coherent drive and the weak thermal force is yet to be developed.

Lateral optomechanical sensing

As mentioned in Chapter 1, in a system where two identical photonic crystal membranes are vertically coupled, breaking its lateral symmetry leads to strong optomechanical coupling with a dark mode in the lateral direction [50]. Together with its strong optomechanical coupling in the vertical direction, a 3D accelerometer may be enabled through multi-mode interrogation in this system. A simple proof-of-concept demonstration can be constructed by a doubly clamped photonic crystal membrane where a comb-drive-like electrostatic actuator can be incorporated to the other two sides of the membrane for systematic lateral displacement of the membrane. Preliminary RCWA simulations reveal modes with such lateral motion sensitivity.

Soft-lithography-enabled hybrid system

We demonstrated that free-standing photonic crystal membranes could be peeled off using PDMS films. The yield of membrane transfer to PDMS is close to 90%. We have also demonstrated transfer of these photonic crystal membranes to a thermally oxidized SOI substrate by creating surface bonds with oxygen plasma. This simple transfer technique of soft-lithography grants much flexibility in creating hybrid systems [53]. One of the ideas is to transfer a highly doped silicon device layer to an oxidized SOI platform to create an electro-optomechanical system, which combines the competitive edge of electrostatic actuation and optomechanical readout.

Other partially investigated topics include the prospective of developing an optomechanical cavity with dissipative coupling via optomechanical control in the optical quality factor of a bonding mode in our asymmetric coupled system [19]. It can be realized by forming a Fabry-Perot cavity where one reflector is our coupled asymmetric photonic crystal membrane. One may also explore sub-bandgap photodetection with silicon photonic crystal membranes with modes that have high concentration of optical energy at the holes' sidewalls [141].

Bibliography

[1] John David Jackson. Classical electromagnetism. *Wiley, NY*, 2:558, 1975.

[2] P. Lebedew. Testings on the compressive force of light. *Annalen Der Physik*, 6(11):433–458, 1901.

[3] E. F. Nichols and G. F. Hull. The pressure due to radiation - (second paper). *Physical Review*, 17(2):91–104, 1903.

[4] A. Ashkin, J. M. Dziedzic, J. E. Bjorkholm, and S. Chu. Observation of a single-beam gradient force optical trap for dielectric particles. *Optics Letters*, 11(5):288–290, 1986.

[5] S. Chu, J. E. Bjorkholm, A. Ashkin, and A. Cable. Experimental-observation of optically trapped atoms. *Physical Review Letters*, 57(3):314–317, 1986.

[6] S. Chu and C. Wieman. Laser cooling and trapping of atoms. *Journal of the Optical Society of America B-Optical Physics*, 6(11):2020–2020, 1989.

[7] P. D. Lett, W. D. Phillips, S. L. Rolston, C. E. Tanner, R. N. Watts, and C. I. Westbrook. Optical molasses. *Journal of the Optical Society of America B-Optical Physics*, 6(11):2084–2107, 1989.

[8] W. D. Phillips. Laser-cooled and trapped atoms - proceedings of a workshop on spectroscopic applications of slow atomic-beams - nbs, gaithersburg, usa 14-15 april 1983 - preface. *Progress in Quantum Electronics*, 8(3-4):117–117, 1984.

[9] M. H. Anderson, J. R. Ensher, M. R. Matthews, C. E. Wieman, and E. A. Cornell. Observation of bose-einstein condensation in a dilute atomic vapor. *Science*, 269(5221):198–201, 1995.

[10] J. Mlynek, V. Balykin, and P. Meystre. Optics and interferometry with atoms. *Applied Physics B-Photophysics and Laser Chemistry*, 54(5):319–320, 1992.

[11] M. Aspelmeyer, S. Groblacher, K. Hammerer, and N. Kiesel. Quantum optomechanics-throwing a glance [invited]. *Journal of the Optical Society of America B-Optical Physics*, 27(6):A189–A197, 2010.

[12] T. J. Kippenberg and K. J. Vahala. Cavity opto-mechanics. *Optics Express*, 15(25):17172–17205, 2007.

[13] T. J. Kippenberg and K. J. Vahala. Cavity optomechanics: Back-action at the mesoscale. *Science*, 321(5893):1172–1176, 2008.

[14] M. Li, W. H. P. Pernice, C. Xiong, T. Baehr-Jones, M. Hochberg, and H. X. Tang. Harnessing optical forces in integrated photonic circuits. *Nature*, 456(7221):480–U28, 2008.

[15] M. Li, W. H. P. Pernice, and H. X. Tang. Tunable bipolar optical interactions between guided lightwaves. *Nature Photonics*, 3(8):464–468, 2009.

[16] P. B. Deotare, I. Bulu, I. W. Frank, Q. M. Quan, Y. N. Zhang, R. Ilic, and M. Loncar. All optical reconfiguration of optomechanical filters. *Nature Communications*, 3, 2012.

[17] G. S. Wiederhecker, L. Chen, A. Gondarenko, and M. Lipson. Controlling photonic structures using optical forces. *Nature*, 462(7273):633–U103, 2009.

[18] J. Rosenberg, Q. Lin, and O. Painter. Static and dynamic wavelength routing via the gradient optical force. *Nature Photonics*, 3(8):478–483, 2009.

[19] M. Li, W. H. P. Pernice, and H. X. Tang. Reactive cavity optical force on microdisk-coupled nanomechanical beam waveguides. *Physical Review Letters*, 103(22), 2009.

[20] R. Thijssen, E. Verhagen, T. J. Kippenberg, and A. Polman. Plasmon nanomechanical coupling for nanoscale transduction. *Nano Letters*, 13(7):3293–3297, 2013.

[21] A. H. Safavi-Naeini, T. P. M. Alegre, M. Winger, and O. Painter. Optomechanics in an ultrahigh-q two-dimensional photonic crystal cavity. *Applied Physics Letters*, 97(18), 2010.

[22] Thomas Corbitt, David Ottaway, Edith Innerhofer, Jason Pelc, and Nergis Mavalvala. Measurement of radiation-pressure-induced optomechanical dynamics in a suspended fabry-perot cavity. *Physical Review A*, 74(2):021802, 2006.

[23] S. Zaitsev, A. K. Pandey, O. Shtempluck, and E. Buks. Forced and self-excited oscillations of an optomechanical cavity. *Physical Review E*, 84(4), 2011.

[24] E. Verhagen, S. Deleglise, S. Weis, A. Schliesser, and T. J. Kippenberg. Quantum-coherent coupling of a mechanical oscillator to an optical cavity mode. *Nature*, 482(7383):63–67, 2012.

[25] M. Tomes and T. Carmon. Photonic micro-electromechanical systems vibrating at x-band (11-ghz) rates. *Physical Review Letters*, 102(11), 2009.

[26] J. Chan, T. P. M. Alegre, A. H. Safavi-Naeini, J. T. Hill, A. Krause, S. Groblacher, M. Aspelmeyer, and O. Painter. Laser cooling of a nanomechanical oscillator into its quantum ground state. *Nature*, 478(7367):89–92, 2011.

[27] E. Gavartin, R. Braive, I. Sagnes, O. Arcizet, A. Beveratos, T. J. Kippenberg, and I. Robert-Philip. Optomechanical coupling in a two-dimensional photonic crystal defect cavity. *Physical Review Letters*, 106(20), 2011.

[28] B. Ilic, S. Krylov, K. Aubin, R. Reichenbach, and H. G. Craighead. Optical excitation of nanoelectromechanical oscillators. *Applied Physics Letters*, 86(19), 2005.

[29] C. H. Metzger and K. Karrai. Cavity cooling of a microlever. *Nature*, 432(7020):1002–1005, 2004.

[30] M. L. Povinelli, S. G. Johnson, M. Loncar, M. Ibanescu, E. J. Smythe, F. Capasso, and J. D. Joannopoulos. High-q enhancement of attractive and repulsive optical forces between coupled whispering-gallery-mode resonators. *Optics Express*, 13(20):8286–8295, 2005.

[31] M. L. Povinelli, M. Loncar, M. Ibanescu, E. J. Smythe, S. G. Johnson, F. Capasso, and J. D. Joannopoulos. Evanescent-wave bonding between optical waveguides. *Optics Letters*, 30(22):3042–3044, 2005.

[32] A. W. Rodriguez, A. P. McCauley, P. C. Hui, D. Woolf, E. Iwase, F. Capasso, M. Loncar, and S. G. Johnson. Bonding, antibonding and tunable optical forces in asymmetric membranes. *Optics Express*, 19(3):2225–2241, 2011.

[33] L. Troger and M. Reichling. Quantification of antagonistic optomechanical forces in an interferometric detection system for dynamic force microscopy. *Applied Physics Letters*, 97(21), 2010.

[34] D. Woolf, P. C. Hui, E. Iwase, M. Khan, A. W. Rodriguez, P. Deotare, I. Bulu, S. G. Johnson, F. Capasso, and M. Loncar. Optomechanical and photothermal interactions in suspended photonic crystal membranes. *Optics Express*, 21(6):7258–7275, 2013.

[35] A. Oskooi, P. A. Favuzzi, Y. Kawakami, and S. Noda. Tailoring repulsive optical forces in nanophotonic waveguides. *Optics Letters*, 36(23):4638–4640, 2011.

[36] S. G. Johnson, M. Ibanescu, M. A. Skorobogatiy, O. Weisberg, J. D. Joannopoulos, and Y. Fink. Perturbation theory for maxwell's equations with shifting material boundaries. *Physical Review E*, 65(6), 2002.

[37] Q. Lin, J. Rosenberg, X. S. Jiang, K. J. Vahala, and O. Painter. Mechanical oscillation and cooling actuated by the optical gradient force. *Physical Review Letters*, 103(10), 2009.

[38] L. Ding, C. Baker, P. Senellart, A. Lemaitre, S. Ducci, G. Leo, and I. Favero. High frequency gaas nano-optomechanical disk resonator. *Physical Review Letters*, 105(26), 2010.

[39] P. C. Hui, D. Woolf, E. Iwase, Y. I. Sohn, D. Ramos, M. Khan, A. W. Rodriguez, S. G. Johnson, F. Capasso, and M. Loncar. Optical bistability with a repulsive optical force in coupled silicon photonic crystal membranes. *Applied Physics Letters*, 103(2), 2013.

[40] Y. G. Roh, T. Tanabe, A. Shinya, H. Taniyama, E. Kuramochi, S. Matsuo, T. Sato, and M. Notomi. Strong optomechanical interaction in a bilayer photonic crystal. *Physical Review B*, 81(12), 2010.

[41] Young-Shin Park and Hailin Wang. Resolved-sideband and cryogenic cooling of an optomechanical resonator. *Nature physics*, 5(7):489–493, 2009.

[42] Peter T Rakich, Miloš A Popović, Marin Soljačić, and Erich P Ippen. Trapping, corralling and spectral bonding of optical resonances through optically induced potentials. *Nature Photonics*, 1(11):658–665, 2007.

[43] V. Ginis, P. Tassin, C. M. Soukoulis, and I. Veretennicoff. Enhancing optical gradient forces with metamaterials. *Physical Review Letters*, 110(5), 2013.

[44] Takashi Asano, Bong-Shik Song, and Susumu Noda. Analysis of the experimental q factors (˜ 1 million) of photonic crystal nanocavities. *Optics express*, 14(5):1996–2002, 2006.

[45] Anatoliy A Savchenkov, Andrey B Matsko, Vladimir S Ilchenko, and Lute Maleki. Optical resonators with ten million finesse. *Optics Express*, 15(11):6768–6773, 2007.

[46] M. Davanco, S. Ates, Y. Liu, and K. Srinivasan. Si3n4 optomechanical crystals in the resolved-sideband regime. *Applied Physics Letters*, 104(4), 2014.

[47] M. Eichenfield, J. Chan, R. M. Camacho, K. J. Vahala, and O. Painter. Optomechanical crystals. *Nature*, 462(7269):78–82, 2009.

[48] P. A. Favuzzi, R. Bardoux, T. Asano, Y. Kawakami, and S. Noda. Ab-initio design of nanophotonic waveguides for tunable, bidirectional optical forces. *Optics Express*, 20(22):24488–24495, 2012.

[49] J. Zhang, K. F. MacDonald, and N. I. Zheludev. Optical gecko toe: Optically controlled attractive near-field forces between plasmonic metamaterials and dielectric or metal surfaces. *Physical Review B*, 85(20), 2012.

[50] V. Liu, M. Povinelli, and S. H. Fan. Resonance-enhanced optical forces between coupled photonic crystal slabs. *Optics Express*, 17(24):21897–21909, 2009.

[51] Y. Sun, T. P. White, and A. A. Sukhorukov. Slow-light enhanced optical forces between longitudinally shifted photonic-crystal nanowire waveguides. *Optics Letters*, 37(5):785–787, 2012.

[52] Yongmin Liu and Xiang Zhang. Metamaterials: a new frontier of science and technology. *Chem. Soc. Rev.*, 40:2494–2507, 2011.

[53] John A. Rogers, Takao Someya, and Yonggang Huang. Materials and mechanics for stretchable electronics. *Science*, 327(5973):1603–1607, 2010.

[54] M. Eichenfield, C. P. Michael, R. Perahia, and O. Painter. Actuation of micro-optomechanical systems via cavity-enhanced optical dipole forces. *Nature Photonics*, 1(7):416–422, 2007.

[55] K. Y. Fong, W. H. P. Pernice, M. Li, and H. X. Tang. Tunable optical coupler controlled by optical gradient forces. *Optics Express*, 19(16):15098–15108, 2011.

[56] H. Cai, B. Dong, J. F. Tao, L. Ding, J. M. Tsai, G. Q. Lo, A. Q. Liu, and D. L. Kwong. A nanoelectromechanical systems optical switch driven by optical gradient force. *Applied Physics Letters*, 102(2), 2013.

[57] M. Bagheri, M. Poot, M. Li, W. P. H. Pernice, and H. X. Tang. Dynamic manipulation of nanomechanical resonators in the high-amplitude regime and non-volatile mechanical memory operation. *Nature Nanotechnology*, 6(11):726–732, 2011.

[58] F. F. Liu, S. Alaie, Z. C. Leseman, and M. Hossein-Zadeh. Sub-pg mass sensing and measurement with an optomechanical oscillator. *Optics Express*, 21(17):19555–19567, 2013.

[59] G. Bahl, K. H. Kim, W. Lee, J. Liu, X. D. Fan, and T. Carmon. Brillouin cavity optomechanics with microfluidic devices. *Nature Communications*, 4, 2013.

[60] K. H. Kim, G. Bahl, W. Lee, J. Liu, M. Tomes, X. D. Fan, and T. Carmon. Cavity optomechanics on a microfluidic resonator with water and viscous liquids. *Light-Science and Applications*, 2, 2013.

[61] B. Dong, J.G. Huang, h. cai, P. Kropelnicki, A.B. Randles, Y.D. Gu, and A.Q. Liu. An all optical shock sensor based on buckled doubly-clamped silicon beam. In *Micro Electro Mechanical Systems (MEMS), 2014 IEEE 27th International Conference on*, pages 692–695, Jan 2014.

[62] V. Intaraprasonk and S. H. Fan. Nonvolatile bistable all-optical switch from mechanical buckling. *Applied Physics Letters*, 98(24), 2011.

[63] A. G. Krause, M. Winger, T. D. Blasius, Q. Lin, and O. Painter. A high-resolution microchip optomechanical accelerometer. *Nature Photonics*, 6(11):768–772, 2012.

[64] Y. X. Liu, H. X. Miao, V. Aksyuk, and K. Srinivasan. Wide cantilever stiffness range cavity optomechanical sensors for atomic force microscopy. *Optics Express*, 20(16):18268–18280, 2012.

[65] H. X. Miao, K. Srinivasan, and V. Aksyuk. A microelectromechanically controlled cavity optomechanical sensing system. *New Journal of Physics*, 14, 2012.

[66] A. H. Safavi-Naeini and O. Painter. Proposal for an optomechanical traveling wave phonon-photon translator. *New Journal of Physics*, 13, 2011.

[67] L. Tian and H. L. Wang. Optical wavelength conversion of quantum states with optomechanics. *Physical Review A*, 82(5), 2010.

[68] M. Notomi, H. Taniyama, S. Mitsugi, and E. Kuramochi. Optomechanical wavelength and energy conversion in high-q double-layer cavities of photonic crystal slabs. *Physical Review Letters*, 97(2), 2006.

[69] J. T. Hill, A. H. Safavi-Naeini, J. Chan, and O. Painter. Coherent optical wavelength conversion via cavity optomechanics. *Nature Communications*, 3, 2012.

[70] M. Davanco, J. Chan, A. H. Safavi-Naeini, O. Painter, and K. Srinivasan. Slot-mode-coupled optomechanical crystals. *Optics Express*, 20(22):24394–24410, 2012.

[71] Y. X. Liu, M. Davanco, V. Aksyuk, and K. Srinivasan. Electromagnetically induced transparency and wideband wavelength conversion in silicon nitride microdisk optomechanical resonators. *Physical Review Letters*, 110(22), 2013.

[72] J. Bochmann, A. Vainsencher, D. D. Awschalom, and A. N. Cleland. Nanomechanical coupling between microwave and optical photons. *Nature Physics*, 9(11):712–716, 2013.

[73] J. J. Zheng, Y. Li, M. S. Aras, A. Stein, K. L. Shepard, and C. W. Wong. Parametric optomechanical oscillations in two-dimensional slot-type high-q photonic crystal cavities. *Applied Physics Letters*, 100(21), 2012.

[74] J. J. Zheng, Y. Li, N. Goldberg, M. McDonald, X. S. Luan, A. Hati, M. Lu, S. Strauf, T. Zelevinsky, D. A. Howe, and C. W. Wong. Feedback and harmonic locking of slot-type optomechanical oscillators to external low-noise reference clocks. *Applied Physics Letters*, 102(14), 2013.

[75] H. Rokhsari, M. Hossein-Zadeh, A. Hajimiri, and K. Vahala. Brownian noise in radiation-pressure-driven micromechanical oscillators. *Applied Physics Letters*, 89(26), 2006.

[76] M. Hossein-Zadeh, H. Rokhsari, A. Hajimiri, and K. J. Vahala. Characterization of a radiation-pressure-driven micromechanical oscillator. *Physical Review A*, 74(2), 2006.

[77] M. Hossein-Zadeh and K. J. Vahala. Observation of injection locking in an optomechanical rf oscillator. *Applied Physics Letters*, 93(19), 2008.

[78] M. Hossein-Zadeh and K. J. Vahala. Photonic rf down-converter based on optomechanical oscillation. *Ieee Photonics Technology Letters*, 20(1-4):234–236, 2008.

[79] M. Hossein-Zadeh and K. J. Vahala. An optomechanical oscillator on a silicon chip. *Ieee Journal of Selected Topics in Quantum Electronics*, 16(1):276–287, 2010.

[80] F. Liu and M. Hossein-Zadeh. On the spectrum of radiation pressure driven optomechanical oscillator and its application in sensing. *Optics Communications*, 294:338–343, 2013.

[81] F. F. Liu and M. Hossein-Zadeh. Characterization of optomechanical rf frequency mixing/down-conversion and its application in photonic rf receivers. *Journal of Lightwave Technology*, 32(2):309–317, 2014.

[82] K.A. Milton. *The Casimir Effect: Physical Manifestations of Zero-point Energy*. World Scientific, 2001.

[83] V.A. Parsegian. *Van der Waals Forces: A Handbook for Biologists, Chemists, Engineers, and Physicists*. Cambridge University Press, 2005.

[84] Alejandro W. Rodriguez, Federico Capasso, and Steven G. Johnson. The Casimir effect in microstructured geometries. *Nature Photonics*, 5:211–221, March 2011. Invited review.

[85] Hendrik BG Casimir. On the attraction between two perfectly conducting plates. In *Proc. K. Ned. Akad. Wet*, volume 51, page 150, 1948.

[86] Igor Ekhiel'evich Dzyaloshinskii, EM Lifshitz, and Lev Petrovich Pitaevskii. General theory of van der waals'forces. *Physics-Uspekhi*, 4(2):153–176, 1961.

[87] Steve K Lamoreaux. Demonstration of the casimir force in the 0.6 to 6 μ m range. *Physical Review Letters*, 78(1):5, 1997.

[88] Umar Mohideen and Anushree Roy. Precision measurement of the casimir force from 0.1 to 0.9 μ m. *Physical Review Letters*, 81(21):4549, 1998.

[89] HB Chan, VA Aksyuk, RN Kleiman, DJ Bishop, and Federico Capasso. Quantum mechanical actuation of microelectromechanical systems by the casimir force. *Science*, 291(5510):1941–1944, 2001.

[90] Giacomo Bressi, Giovanni Carugno, Roberto Onofrio, and Giuseppe Ruoso. Measurement of the casimir force between parallel metallic surfaces. *Physical review letters*, 88(4):041804, 2002.

[91] RS Decca, D López, E Fischbach, and DE Krause. Measurement of the casimir force between dissimilar metals. *Physical review letters*, 91(5):050402, 2003.

[92] S De Man, K Heeck, RJ Wijngaarden, and D Iannuzzi. Halving the casimir force with conductive oxides. *Physical review letters*, 103(4):040402, 2009.

[93] C-C Chang, AA Banishev, GL Klimchitskaya, VM Mostepanenko, and U Mohideen. Reduction of the casimir force from indium tin oxide film by uv treatment. *Physical review letters*, 107(9):090403, 2011.

[94] Justine Laurent, Hermann Sellier, Alexis Mosset, Serge Huant, and Joël Chevrier. Casimir force measurements in au-au and au-si cavities at low temperature. *Physical Review B*, 85(3):035426, 2012.

[95] WJ Kim, AO Sushkov, DAR Dalvit, and SK Lamoreaux. Measurement of the short-range attractive force between ge plates using a torsion balance. *Physical review letters*, 103(6):060401, 2009.

[96] AA Banishev, GL Klimchitskaya, VM Mostepanenko, and U Mohideen. Demonstration of the casimir force between ferromagnetic surfaces of a ni-coated sphere and a ni-coated plate. *Physical review letters*, 110(13):137401, 2013.

[97] HB Chan, Y Bao, J Zou, RA Cirelli, F Klemens, WM Mansfield, and CS Pai. Measurement of the casimir force between a gold sphere and a silicon surface with nanoscale trench arrays. *Physical review letters*, 101(3):030401, 2008.

[98] Y Bao, R Guérout, J Lussange, A Lambrecht, RA Cirelli, F Klemens, WM Mansfield, CS Pai, and HB Chan. Casimir force on a surface with shallow nanoscale corrugations: Geometry and finite conductivity effects. *Physical review letters*, 105(25):250402, 2010.

[99] Astrid Lambrecht and Valery N Marachevsky. Casimir interaction of dielectric gratings. *Physical review letters*, 101(16):160403, 2008.

[100] HB Chan, VA Aksyuk, RN Kleiman, DJ Bishop, and Federico Capasso. Nonlinear micromechanical casimir oscillator. *Physical Review Letters*, 87(21):211801, 2001.

[101] J Zou, Z Marcet, AW Rodriguez, MTH Reid, AP McCauley, II Kravchenko, T Lu, Y Bao, SG Johnson, and HB Chan. Casimir forces on a silicon micromechanical chip. *Nature communications*, 4:1845, 2013.

[102] E Buks and ML Roukes. Stiction, adhesion energy, and the casimir effect in micromechanical systems. *Physical Review B*, 63(3):033402, 2001.

[103] Eyal Buks and Michael L Roukes. Metastability and the casimir effect in micromechanical systems. *EPL (Europhysics Letters)*, 54(2):220, 2001.

[104] D Rugar, HJ Mamin, and Peter Guethner. Improved fiber-optic interferometer for atomic force microscopy. *Applied Physics Letters*, 55(25):2588–2590, 1989.

[105] Klaus Thurner, Pierre-François Braun, and Khaled Karrai. Absolute distance sensing by two laser optical interferometry. *Review of Scientific Instruments*, 84(11):115002, 2013.

[106] Alexander Högele, Stefan Seidl, Martin Kroner, Khaled Karrai, Christian Schulhauser, Omar Sqalli, Jan Scrimgeour, and Richard J Warburton. Fiber-based confocal microscope for cryogenic spectroscopy. *Review of scientific instruments*, 79(2):023709, 2008.

[107] DT Smith, JR Pratt, and LP Howard. A fiber-optic interferometer with subpicometer resolution for dc and low-frequency displacement measurement. *Review of Scientific Instruments*, 80(3):035105, 2009.

[108] MY Shagam. *Thesis: Nanomechanical displacement detection using fiber optic interferometery*. PhD thesis, 2006.

[109] Eric RI Abraham and Eric A Cornell. Teflon feedthrough for coupling optical fibers into ultrahigh vacuum systems. *Applied optics*, 37(10):1762–1763, 1998.

[110] Alejandro W Rodriguez, David Woolf, Pui-Chuen Hui, Eiji Iwase, Alexander P McCauley, Federico Capasso, Marko Loncar, and Steven G Johnson. Designing evanescent optical interactions to control the expression of casimir forces in optomechanical structures. *Applied Physics Letters*, 98(19):194105, 2011.

[111] Eiji Iwase, Pui-Chuen Hui, David Woolf, Alejandro W Rodriguez, Steven G Johnson, Federico Capasso, and Marko Lonar. Control of buckling in large micromembranes using engineered support structures. *Journal of Micromechanics and Microengineering*, 22(6):065028, 2012.

[112] J. Lee, B. Zhen, S. L. Chua, W. J. Qiu, J. D. Joannopoulos, M. Soljacic, and O. Shapira. Observation and differentiation of unique high-q optical resonances near zero wave vector in macroscopic photonic crystal slabs. *Physical Review Letters*, 109(6), 2012.

[113] O. Kilic, M. Digonnet, G. Kino, and O. Solgaard. Controlling uncoupled resonances in photonic crystals through breaking the mirror symmetry. *Optics Express*, 16(17):13090–13103, 2008.

[114] S. L. Chua, Y. D. Chong, A. D. Stone, M. Soljacic, and J. Bravo-Abad. Low-threshold lasing action in photonic crystal slabs enabled by fano resonances. *Optics Express*, 19(2):1539–1562, 2011.

[115] M. El Beheiry, V. Liu, S. H. Fan, and O. Levi. Sensitivity enhancement in photonic crystal slab biosensors. *Optics Express*, 18(22):22702–22714, 2010.

[116] Vladimir B Braginsky, Vladimir Borisovich Braginsky, and Farid Ya Khalili. *Quantum measurement*. Cambridge University Press, 1995.

[117] Constanze Metzger, Ivan Favero, Alexander Ortlieb, and Khaled Karrai. Optical self cooling of a deformable fabry-perot cavity in the classical limit. *Physical Review B*, 78(3):035309, 2008.

[118] A. Schliesser, P. Del'Haye, N. Nooshi, K. J. Vahala, and T. J. Kippenberg. Radiation pressure cooling of a micromechanical oscillator using dynamical backaction. *Physical Review Letters*, 97(24), 2006.

[119] A. Schliesser, R. Riviere, G. Anetsberger, O. Arcizet, and T. J. Kippenberg. Resolved-sideband cooling of a micromechanical oscillator. *Nature Physics*, 4(5):415–419, 2008.

[120] M. Eichenfield, R. Camacho, J. Chan, K. J. Vahala, and O. Painter. A picogram- and nanometre-scale photonic-crystal optomechanical cavity. *Nature*, 459(7246):550–U79, 2009.

[121] Albert Schließer. *Cavity optomechanics and optical frequency comb generation with silica whispering-gallery-mode microresonators*. PhD thesis, lmu, 2009.

[122] Y. T. Yang, C. Callegari, X. L. Feng, K. L. Ekinci, and M. L. Roukes. Zeptogram-scale nanomechanical mass sensing. *Nano Letters*, 6(4):583–586, 2006.

[123] B. S. Sheard, M. B. Gray, C. M. Mow-Lowry, D. E. McClelland, and S. E. Whitcomb. Observation and characterization of an optical spring. *Physical Review A*, 69(5), 2004.

[124] T. J. Johnson, M. Borselli, and O. Painter. Self-induced optical modulation of the transmission through a high-q silicon microdisk resonator. *Optics Express*, 14(2):817–831, 2006.

[125] D. Blocher, A. T. Zehnder, R. H. Rand, and S. Mukerji. Anchor deformations drive limit cycle oscillations in interferometrically transduced mems beams. *Finite Elements in Analysis and Design*, 49(1):52–57, 2012.

[126] K. Srinivasan and O. Painter. Momentum space design of high-q photonic crystal optical cavities. *Optics Express*, 10(15):670–684, 2002.

[127] Daniel Garcia-Sanchez, King Yan Fong, Harish Bhaskaran, Steve Lamoreaux, and Hong X Tang. Casimir force and in situ surface potential measurements on nanomembranes. *Physical review letters*, 109(2):027202, 2012.

[128] Travis C Briles, Dylan C Yost, Jun Ye, Thomas R Schibli, et al. Simple piezoelectric-actuated mirror with 180 khz servo bandwidth. *Optics express*, 18(10):9739–9746, 2010.

[129] Igor Bargatin. *High-frequency nanomechanical resonators for sensor applications*. PhD thesis, California Institute of Technology, 2008.

[130] S Knünz, M Herrmann, V Batteiger, G Saathoff, TW Hänsch, K Vahala, and Th Udem. Injection locking of a trapped-ion phonon laser. *Physical review letters*, 105(1):013004, 2010.

[131] Mahmood Bagheri, Menno Poot, Linran Fan, Florian Marquardt, and Hong X Tang. Photonic cavity synchronization of nanomechanical oscillators. *Physical review letters*, 111(21):213902, 2013.

[132] Huan Li, Yu Chen, Jong Noh, Semere Tadesse, and Mo Li. Multichannel cavity optomechanics for all-optical amplification of radio frequency signals. *Nature communications*, 3:1091, 2012.

[133] WJ Kim, M Brown-Hayes, DAR Dalvit, JH Brownell, and R Onofrio. Anomalies in electrostatic calibrations for the measurement of the casimir force in a sphere-plane geometry. *Physical Review A*, 78(2):020101, 2008.

[134] Woo-Joong Kim, AO Sushkov, Diego AR Dalvit, and Steve K Lamoreaux. Surface contact potential patches and casimir force measurements. *Physical Review A*, 81(2):022505, 2010.

[135] Guillaume Jourdan, Astrid Lambrecht, Fabio Comin, and Joël Chevrier. Quantitative non-contact dynamic casimir force measurements. *EPL (Europhysics Letters)*, 85(3):31001, 2009.

[136] AO Sushkov, WJ Kim, DAR Dalvit, and SK Lamoreaux. Observation of the thermal casimir force. *Nature Physics*, 7(3):230–233, 2011.

[137] CC Speake and C Trenkel. Forces between conducting surfaces due to spatial variations of surface potential. *Physical review letters*, 90(16):160403, 2003.

[138] RO Behunin, F Intravaia, DAR Dalvit, PA Maia Neto, and S Reynaud. Modeling electrostatic patch effects in casimir force measurements. *Physical Review A*, 85(1):012504, 2012.

[139] RO Behunin, Y Zeng, DAR Dalvit, and S Reynaud. Electrostatic patch effects in casimir-force experiments performed in the sphere-plane geometry. *Physical Review A*, 86(5):052509, 2012.

[140] Paolo Cardile, Giorgia Franzò, Roberto Lo Savio, Matteo Galli, Thomas F Krauss, Francesco Priolo, and Liam OFaolain. Electrical conduction and optical properties of doped silicon-on-insulator photonic crystals. *Applied Physics Letters*, 98(20):203506, 2011.

[141] Hui Chen, Xianshu Luo, and Andrew W Poon. Cavity-enhanced photocurrent generation by 1.55 μm wavelengths linear absorption in a pin diode embedded silicon microring resonator. *Applied Physics Letters*, 95(17):171111, 2009.

Appendix A

Vapor hydrogen fluoride etch

The release of movable parts in MEMS and NEMS structures cannot be performed in a fluid environment without properly introducing anti-stiction schemes to the devices. For instance, in the case of removing a sacrificial layer of silicon dioxide, hydrofluoric acid is often employed. However, once the wet etch is completed, the capillary force due to the etchant pulls the movable parts to their neighboring parts, causing stiction. Two typical approaches of successfully releasing MEMS and NEMS are critical point drying (CPD) and vapor-phase etch. Critical point drying is performed by first replacing the etchant fluid by isopropanol. Upon immersing the wet released device into a critical point dryer, carbon dioxide gas is pumped into the drying chamber. By applying high pressure to the chamber which turns the carbon dioxide gas into a liquid form at the critical point, the liquid carbon dioxide displaces the isopropanol layer in between the movable parts. Reducing the pressure then turns the carbon dioxide back into a gaseous form, which eliminates the threat of stiction due to the capillary force. For releasing the photonic crystal membranes fabricated

on a silicon-on-insulator platform, we employ vapor hydrogen fluoride etch (VHFE) which has the merit of minimizing handling of hazardous chemicals.

VHFE was considered difficult to control when first explored in our lab. Vaguely we understood the etching performance was related to the humidity of the environment and the platens temperature. However, the principles of etching timing and the evaluation of the complete removal of the sacrificial oxide layer were not well established until recently. Here we lay out a reliable set of procedures which have produced numerous properly released structures.

Basic understanding of the chemistry of anhydrous hydrogen fluoride and water with silicon dioxide helps to understand the rationales of the VHFE procedures we adopted. A two-reaction mechanism of the VHFE is presented as follows:

$$SiO_2 + 4HF(g) \rightarrow SiF_4 + 2H_20$$

$$4HF(g) + 2H_20 \rightarrow 2HF_2^- + 2H_30^+$$

$$SiO_2 + 2HF_2^- + 2H_30^+ \rightarrow 4H_20 + SiF_4(g)$$

As we see from above, water serves as a catalyst which first ionizes the anhydrous hydrogen fluoride to form hydrofluoric acid, and is released after silicon dioxide is etched. In another words, water initiates the VHFE process. However, condensation of the water by-product on the sample could be detrimental when it exerts a capillary force on the structure to be released. Hence prior to loading the sample for VHFE, baking the sample at $180°C$ to remove the excess, adsorbed water molecules for at least 10 minutes is in order. Also, the platen temperature of the VHFE chamber set at $35°C$ or above discourages water condensation/ re-deposition on the sample. While higher platen temperature is more effective in reducing water condensation,

it comes at a cost of lower etch rate. Currently $35°C$ is found to be a good trade-off temperature which gives a reasonable etch rate and keeps water condensation low. Finally, it may be beneficial to divide a long session of etch into several shorter sessions: since the reaction produces extra water molecules, re-setting the chambers humidity by venting the chamber once in a while helps to reduce water condensation.

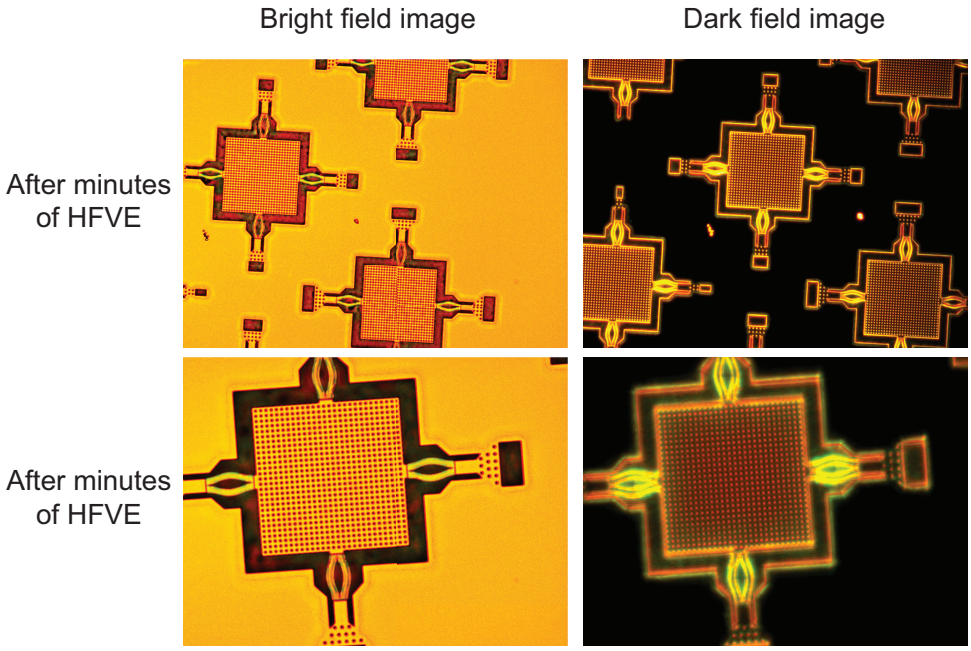

Figure A.1: Bright and dark field optical images of photonic crystal membranes subjected to vapor hydrogen fluoride etch for TODO minutes. In the bright field images, the edges of the membrane's frame look lighter in color than the rest of the sample surface due to the oxide removal by VHFE. One may see some darker spots on the membrane indicating the presence of residual oxide left unetched. In the dark field image, one can see the non-uniformity of the color throughout the membrane. It is due to the stronger contrast established by increased scattering of the oxide.

Since the SOI samples we work with have thin silicon device layers ($\approx$ 200nm), it is possible to monitor the etch progress by directly looking at the remaining oxide underneath the silicon layer in both the bright and dark field modes. In particular the dark field modes show a contrast in image brightness locally as light becomes

scattered. For thin silicon layers the visible light can illuminate through them to reveal the residual oxide left. See Figure A.1 for details. Another useful indicator of the oxide removal is by observing the release of cantilevers and doubly clamped beams. In our double-silicon SOI platform, structures are subjected to in-plane compressive stress and large turning moment due to a gradient layer of oxide left underneath the released structures.

Procedures of vapor hydrogen fluoride etch:

1. Bake the sample at $180°C$ for at least 10 minutes.

2. Condition the VHFE chamber for around 10 minutes until the desired temperature increase of the platen is reached.

3. Load in a dummy sample to etch for 3 minutes to monitor the etch rate which might vary due to environmental variations. Carefully observe the color change in areas where oxide is prone to HF attacks in an optical microscope both in the bright and dark field.

4. The release of the cantilever and double-clamped beams is also a good indicator of the etch progress.

5. Note the total time needed for (almost) fully releasing the photonic crystal membrane with all residual oxide etched.

6. Load in the actual sample to etch for 2 minutes. Monitor the etch rate by monitoring the progress with the bright and dark field of the optical microscope. It is important to remain patient lest the devices are stuck due to stiction caused by water condensation.